Filter Bank Multicarrier Waveforms for Future Wireless Networks: Interference Analysis and Cancellation

Sumaila Anning Mahama

Doctor of Philosophy

University of York
Electronic Engineering

July 2021

Abstract

Billions of devices are expected to connect to future wireless networks. Although conventional orthogonal division multiplexing (OFDM) has proven to be an effective physical layer waveform for enhanced mobile broadband (eMBB), it experiences various challenges. For example, OFDM experiences high out-of-band (OOB) emission caused by the use of rectangular filters. This causes interference to adjacent frequency bands and make OFDM highly sensitive to asynchronous transmissions. Filter bank multicarrier (FBMC) systems have emerged as a promising waveform candidate to satisfy the requirements of future wireless networks. They employ prototype filters with faster spectral decay, which results in better OOB emission and spectral efficiency compared to OFDM. Also, FBMC systems support asynchronous transmissions, which can reduce the signalling overhead in future applications. However, in FBMC systems there is no subcarriers orthogonality, resulting in intrinsic interference. The purpose of this thesis is to address the intrinsic interference problem to make FBMC a viable option for practical application in future wireless networks.

In this thesis, iterative interference cancellation (IIC) receivers are developed for FBMC systems to improve their performance and applicability in future applications. First, an IIC receiver is studied for uncoded FBMC with quadrature amplitude modulation (FBMC-QAM) systems. To improve the decoding performance, bit-interleaved coded modulation with iterative decoding (BICM-ID) is incorporated into the IIC receiver design and the technique of extrinsic information transfer (EXIT) chart analysis is used to track the convergence of the IIC-based BICM-ID receiver. Furthermore, the energy harvesting capabilities of FBMC is considered. Particularly, FBMC is integrated with a simultaneous wireless information and power transfer (SWIPT) technique. Finally, an interference cancellation receiver is investigated for asynchronous FBMC systems in both single and mixed numerology systems. Analytical expressions are derived for the various schemes and simulations results are shown to verify the performance of the different FBMC systems.

Table of Contents

List of Figures

List of Tables

Acknowledgements

First, my deepest gratitude goes to my supervisors, Prof. Alister Burr and Prof. David Grace, for their invaluable guidance during this period of my PhD studies. The accomplishment of this study would not have been feasible without their kind support and insightful supervision. I would also like to thank my thesis advisor, Dr. Kanapathippillai Cumanan for his helpful discussions over the course of this study.

Secondly, I thank the European Commission for providing the funding for my studies through its Horizon 2020 Marie Curie Actions. The program provided me with the opportunity to collaborate and interact with researchers across Europe. For this I am forever grateful.

Finally, I would like to express my heartfelt gratitude to my family and friends for their moral and emotional support throughout my life and from the first day of my PhD journey until the end.

Declaration

I declare that this thesis is a presentation of original work and I am the sole author. This work has not previously been presented for an award at this, or any other, University. All sources are acknowledged as References.

List of Symbols

$(\cdot)^*$	Complex Conjugate
$(\cdot)^T$	Transpose
$(\cdot)^H$	Hermitian Transpose
$(\cdot)^{-1}$	Inverse
$\mathbb{E}$	Expectation
$\mathbf{x}$	Vector
$\mathbf{X}$	Matrix
$\mathbf{I}$	Identity Matrix
$\mathbb{C}^{N\times M}$	$N \times M$ dimensional complex matrix
$\mathfrak{R}(\mathfrak{x})$	Real Part of complex number x
$\mathfrak{I}(\mathfrak{x})$	Imaginary Part of complex number x
$\log(x)$	Logarithm of x to base 10
$\log 2(x)$	Logarithm of x to base 2
$\min(\cdot)$	Minimum of a function
$\max(\cdot)$	Maximum of a function
$Q(\cdot)$	Q-function
$\cup$	Union Operation
$\cap$	Intersection Operation
δ	Kronecker delta function
∂f	First derivative of f
$\partial^2 f$	Second derivative of f

List of Abbreviations

4G	Forth Generation
5G	Fifth Generation
3GPP	3rd Generation Partnership Project
AFB	Analysis Filter Bank
AAP	A Priori Probability
AWGN	Additive White Gaussian Noise
BER	Bit-Error-Rate
BICM-ID	Bit-Interleaved Coded Modulation with Iterative Decoding
BS	Base Station
BWP	Bandwidth Parts
CP	Cyclic Prefix
CND	Check Node Decoder
CSI	Channel State Information
DL	Downlink
DFT	Discrete Fourier Transform
EH	Energy Harvesting
eMBB	enhanced Mobile Broadband
EPA	Extended Pedestrian A
EVA	Extended Vehicular A
ETU	Extended Typical Urban

EXIT	Extrinsic Information Transfer
FEC	Forward Error-correcting Code
FDM	Frequency-Division Multiplexing
FBMC	Filter Bank Multicarrier
FFT	Fast Fourier Transform
f-OFDM	filtered OFDM
GFDM	Generalized Frequency Division Multiplexing
GSM	Global System for Mobile Communication
ICI	Inter-Carrier Interference
IDFT	Inverse Discrete Fourier Transform
IFFT	Inverse Fast Fourier Transform
INI	Inter-Numerology Interference
IIC	Iterative Interference Cancellation
ISI	Inter-Symbol Interference
LDPC	Low-Density Parity-Check
LLR	Log-Likelihood Ratio
LTE	Long Term Evolution
LTE-A	Long-Term Evolution Advanced
mMTC	massive Machine-Type Communications
MI	Mutual Information
MIMO	Multiple-Input Multiple-Output
MLD	Maximum Likelihood detection
MUI	Multi-User Interference
NB-IoT	Narrowband-IoT
NR	New Radio

NPR	Nearly Perfect Reconstruction
OFDM	Orthogonal Frequency Division Multiplexing
OOB	Out-of-band
OQAM	Offset Quadrature Amplitude Modulation
PeIC	Perfect Interference Cancellation
PDF	Probability Distribution Function
PHY	Physical Layer
PIC	Parallel Interference Cancellation
PPN	Polyphase Network
PR	Perfect Reconstruction
PRB	Physical Resource Block
PS	Power Splitting
PSD	Power Spectral Density
QAM	Quadrature Amplitude Modulation
RF	Radio Frequency
RV	Random Variable
SFB	Synthesis Filter Bank
SISO	Soft-Input Soft-Output
SNR	Signal-to-Noise Ratio
STBC	Space-Time Block Coding
SWIPT	Simultaneous Wireless Information and Power Transfer
TDMA	Time Division Multiple Access
TO	Timing Offset
TS	Time Switching
UL	Uplink

UN	User Node
URLLC	Ultra-Reliable Low Latency Communications
VND	Variable Node Decoder
WMMSE	Weighted Minimum Mean Squared Error
WPT	Wireless Power Transfer
WPCN	Wireless Powered Communication Networks
WSR	Weighted Sum-Rate
ZF	Zero-Forcing

Chapter 1

Introduction

1.1 Overview and Motivation

Mobile communication networks have evolved over the past few decades to provide better connectivity and improved network efficiency. From a network that was originally designed for voice calls and low data rate text messaging in the early generations, the fourth generation (4G) and current fifth generation (5G) networks support large data broadband applications. 5G in particular is designed to satisfy the communication requirements of a wide range of applications that can be classified into three main use cases as follows: [1]

- enhanced Mobile Broadband (eMBB)
- massive Machine-Type Communications (mMTC)
- Ultra-Reliable Low Latency Communications (URLLC)

Although the above use cases correctly generalises 5G scenarios, they cannot satisfy all the technical requirements of future wireless networks. For instance, some future applications scenarios may require not only ultra-high data rates but also low latency. As such any use case classification for future networks must take into account the interworking among different scenarios and their relationship with the above mentioned 5G use cases. An example of such consideration is presented in [2] where three enhanced use cases are proposed to support disruptive applications in future networks. They are:

- ubiquitous Mobile Broadband (uMBB) - which can provide global ubiquitous broadband connectivity and significantly boost network capacity for hot spots.
- massive Ultra-Reliable Low Latency Communication (mULC) - which can support applications that require both URLLC and extremely high throughput.
- Ultra-Reliable Low Latency Broadband Communication (ULBC) - which can combine the capabilities of both mMTC and URLLC to facilitate the deployment of a massive number of sensor nodes.

These new use cases can fill the gaps in the 5G scenarios and the combined set of use cases can support all kinds of applications in future networks. However, the different use cases have contrasting requirements on network parameters such as throughput, latency, reliability, and number of connected devices. To effectively accommodate such diverse use cases, future networks should be designed with the core objective of flexibility and adaptability. One way to achieve this flexibility is for the network to allow the coexistence of different technologies. For instance, some Physical layer (PHY) techniques, e.g. waveform type and numerologies, are more suitable to some applications compared to others, necessitating the need for different PHY techniques to coexist in order to serve all use cases efficiently.

One PHY technology that has been widely adopted as the multicarrier waveform for existing wireless communications networks is OFDM. This is due to advantages over previous technologies, such as robustness to channel frequency selectivity, high spectral efficiency due to subcarrier ovelap to achieve orthogonality, and its robustness against intersymbol interference (ISI) and intercarrier interference (ICI) by using sufficient guard bands and cyclic prefix (CP) [3]. In addition, with a sufficient CP length, OFDM requires only a simple per subcarrier equalizer to combat the effect of frequency selective channels. Because of its advantages and to ensure backward compatibility with the existing 4G system, OFDM has been selected for 5G new radio (NR) [4, 5]. Also, to enable the coexistence of the three use cases, 5G NR adopts a range of numerologies to satisfy the different technical requirements and provide a unified underlying frame structure for the PHY. Here, the term numerology simply refers to a particular subcarrier spacing and the corresponding symbol duration. However, some of the drawbacks of OFDM mean that it is not the most efficient multicarrier waveform to satisfy all the requirements of future wireless networks.

For example, OFDM systems use a rectangular pulse shaping filter which results in high OOB emission between adjacent frequency bands. Therefore, to ensure that subbands do not interfere, longer CP duration and wider guard bands are needed, which reduces the spectral efficiency of OFDM. In addition, OFDM requires the grant-based synchronization procedure in which each UN sends a scheduling request to a base station (BS) and wait for the BS to grant it radio resources. For future applications, such as mMTC, the overhead and delay involved in the synchronization procedure can be significant due to the high connection density [6–9]. Therefore, for such applications, it is desirable to allow contention-based grant-free or asynchronous transmissions, in which each UN operates in a wake-up-and-transmit manner [10]. However, OFDM has been shown to perform poorly in asynchronous transmissions due to its poor OOB emission performance [7]. Motivated by these disadvantages of OFDM, alternative multicarrier waveforms have been investigated recently for future applications in which OFDM may be inefficient.

For applications like mMTC, FBMC has emerged as a promising alternative waveform to OFDM [11, 12]. FBMC employs well-localized prototype filters to improve the poor OOB leakage of OFDM, which reduces its sensitivity to asynchronous transmissions [13]. This implies that smaller guard bands are needed between adjacent sub-bands, which improves the spectral efficiency compared to

OFDM. Furthermore, FBMC systems can support a grant-free synchronization procedure because of the improved frequency localization, which makes the waveform robust against asynchronous transmissions and channel frequency selectivity without using any CP [14]. FBMC systems provides efficient and flexible time-frequency allocation to support the huge connection density required in future mMTC applications.

However, as stated in the Balian-Low Theorem, orthogonality, high time-frequency localization and maximum symbol density cannot be achieved simultaneously by a multicarrier system [15, 16]. Hence, the improvement in frequency localization achieved in FBMC is at the expense of the loss of complex orthogonality between subcarriers. The basic idea in FBMC is to relax the orthogonality condition to guarantee the other two factors mentioned above. However, the relaxed orthogonality in FBMC causes intrinsic interference between symbols and subcarriers. It was shown in [17] that by introducing a shift of half the symbol period between the real and imaginary components of a complex QAM symbol, it is possible to recover the information symbols free of ISI and ICI. This is known as offset QAM (OQAM) and has been implemented for FBMC systems. In FBMC-OQAM, the orthogonality is achieved in the real domain with the imaginary part of the signal serving as intrinsic interference [11, 18]. Moreover, OQAM processing limits the direct implementation of some conventional PHY techniques such as channel estimation, space-time block coding (STBC) and maximum likelihood detection (MLD) [13]. Furthermore, in the presence of multipath fading channels, the real-part orthogonality of FBMC-OQAM may be lost, resulting in ISI and ICI. To resolve the problems in FBMC-OQAM, the transmission of complex QAM symbols in FBMC systems is investigated in [14, 19]. By transmitting QAM signals, the FBMC-QAM systems cannot guarantee complex orthogonality between subcarriers which results in intrinsic interference. Therefore, FBMC-QAM is classified as a non-orthogonal waveform, in contrast to OFDM which is an orthogonal waveform.

Apart from the need for asynchronous access, it is essential for future mMTC networks to be self-sustaining, especially for energy-constrained sensor devices, such as those embedded in buildings [20]. Although the life span of such devices could be extended through battery charging or replacement, the process may be inconvenient. For such devices, energy harvesting (EH) is a promising approach to provide device self-sustainability and prolong the battery life. Conventional EH methods collects energy from environmental sources, such as wind, solar etc. However, these natural energy sources are unstable and changes with changing environmental conditions [21]. Because the radio frequency (RF) signal can transmit both information and energy, wireless power transfer (WPT) has emerged as an enabling technology to address the power problems in future wireless networks [22]. One practical implementation of WPT is the concept of SWIPT. In SWIPT, a receiver node can harvest energy and decode information from the received RF signal by employing either the separated receiver mode or co-located receiver mode [23]. In the separated receiver mode, separate receivers are used for information decoding (ID) and EH. Thus, each receiver can have a dedicated antenna without the need to split the received signal. In the co-located receiver mode, on the other hand, a single receiver

simultaneously performs ID and EH. The received signal is split into two portions for ID and EH by either time switching (TS) or power splitting (PS) [24, 25].

The key challenge in FBMC-QAM systems is how to mitigate the interference problem while maintaining the good features of compatibility with conventional PHY techniques, improved spectral efficiency and suitability for asynchronous or grant-free transmissions. Moreover, unlike traditional wireless communications, in which interference is treated as an undesired signal, it can be exploited as a useful signal for wireless EH in SWIPT systems. By harnessing the benefits of FBMC-QAM and SWIPT, billions of devices can be effectively connected and powered anywhere, at any time.

1.2 Research Objectives

Following the overview and motivation above, the main objective of this thesis is to address the following research questions:

How can the intrinsic interference in FBMC-QAM systems be effectively eliminated at the information receiver to enable its application in future wireless networks?

Focusing on harnessing the good spectral efficiency and suitability to asynchronous transmissions, this thesis examines the use of FBMC-QAM in future applications. First, this thesis investigates the performance of an IIC receiver in a single user FBMC-QAM system. To further improve the decoding performance of the single user FBMC-QAM model, an IIC-based BICM-ID receiver is considered. Specifically, the aim is to determine whether the IIC-based BICM-ID receiver can effectively eliminate the intrinsic interference in FBMC-QAM systems, and to investigate the convergence behaviour and computational complexity of this receiver.

Furthermore, a multiuser uplink FBMC-QAM system is investigated in this thesis, where multiple UNs transmit their signal to a BS in a grant-free manner. Moreover, as stated above, the different use cases of 5G and beyond systems will be better served by adopting different numerologies for different applications. Thus, a scenario where UNs with different numerologies transmit their signals asynchronous to a BS is considered. The performance of a novel iterative receiver based on parallel interference cancellation (PIC) and IIC is investigated for the multi-user, multi-numerology FBMC-QAM system.

Can the intrinsic interference in FBMC-QAM systems be opportunistically exploited as a useful signal at the energy receiver in SWIPT systems?

For most future wireless networks, high energy conversion rate and long battery life of UNs are key requirements. In conventional communication systems, interference is treated as an unwanted signal at the information receiver. However, in SWIPT systems interference signals can serve as a useful signal for RF EH. As a result, the intrinsic interference in FBMC systems is exploited for EH in

this thesis. Considering the case where network nodes are equipped with an energy receiver, it is determined whether the nodes can harvest a significant amount of energy from the received signal in the downlink (DL), to aid their information transmission in the uplink (UL). Specifically, the goal is to consider a SWIPT based FBMC-QAM system, in which UNs can decode information and harvest energy from the received signal in the DL and utilize the harvested energy to power their transmission in the UL.

1.3 Thesis Outline and Contributions

Motivated by the challenge of addressing the intrinsic interference problem in FBMC-QAM systems, the aim of this thesis is to develop different interference cancellation receivers to improve the performance and applicability of FBMC-QAM system in future wireless networks. In particular, IIC is studied to iteratively cancel the intrinsic interference in different FBMC-QAM system models. The scope of this thesis includes mathematical modelling of the received signal in terms of the desired and interference components, development of different interference cancellation algorithms, complexity analysis, as well as numerical simulation results. The thesis consist of seven chapters and the main contributions of the remaining chapters are summarised as follows:

Chapter 2 provides the fundamental concepts and literature review relevant to this thesis. First, a review of 5G NR is provided to outline the various numerologies standardized for 5G. Next, a description of the various candidate multicarrier waveforms for future wireless networks is presented. In addition, the basics of statistical channel models, including standard LTE channel models are introduced. Furthermore, an overview of iterative detection and decoding using low-density parity-check (LDPC) coding, including the fundamental concepts of EXIT chart analysis is provided. Finally, the underlying concepts of RF EH systems have been presented.

In Chapter 3, the interference analysis and cancellation of a single user uncoded FBMC-QAM systems is studied, where the received FBMC-QAM signal is separated into even- and odd-numbered subcarrier components and the analytical expression of each component is derived in terms of the desired signal, ICI, ISI and noise. Since the FBMC-QAM prototype filters are well-localized in the frequency domain, it is assumed that data on even-numbered (odd-numbered) subcarriers causes negligible interference to other even-numbered (odd-numbered) subcarriers. Therefore, by demodulating the even- and odd-numbered subcarrier components separately, the level of intrinsic interference can be reduced. Based on the derived expressions, an IIC receiver is implemented in which the intrinsic interference terms of even- and odd-numbered subcarrier components can be estimated and subtracted from the received signal in each iteration of the receiver. Simulation results have been provided to demonstrate the effectiveness of the proposed IIC receiver.

An error floor problem is encountered in Chapter 3 which limits the BER performance of the IIC receiver. Therefore, to improve performance, an IIC-based BICM-ID receiver is proposed for a single user FBMC-QAM system in Chapter 4. The proposed receiver consists of an inner decoder,

which combines iterative demodulation and interference cancellation, and an outer decoder which is an LDPC channel decoder. An analytical model is presented to derive the intrinsic interference terms at the FBMC-QAM receiver. To evaluate the convergence behaviour and complexity analysis of the proposed receiver, EXIT chart analysis is employed, where the EXIT functions of the components of the iterative receiver are derived. Based on the derived EXIT functions, the number of iterations and the convergence threshold of the proposed receiver under different fading channels is evaluated.

In Chapter 5, the single user FBMC-QAM models in Chapters 3 and 4 are extended to a multiuser FBMC-QAM system. To cultivate the desirable benefits offered by both FBMC-QAM and SWIPT, a multiuser FBMC-based SWIPT system is considered in which UNs can simultaneously process ID and EH. Each UN, equipped with separate antennas for ID and EH, communicates with a single antenna BS via time division multiple access (TDMA). At the EH receiver, a non-linear EH model is adopted to capture the non-linear behaviour of practical EH circuits. Furthermore, an IIC receiver is implemented to cancel the intrinsic interference at the information receiver of both the UN and the BS. The aim of this chapter is to maximize the weighted sum-rate by optimizing the weight allocation, time allocation, and power allocation of each UN while satisfying the total DL transmit power and EH constraints. The problem is reformulated as a weighted minimum mean squared error (WMMSE) problem, which is then converted to two subproblems: (i) time and weight allocation problem and (ii) power allocation problem. Finally, a joint resource allocation algorithm is proposed to combine the solutions of the time and weight allocation problem and the power allocation problem.

Due to the highly diverse nature of future wireless applications, UNs with different performance requirements may have different numerologies, i.e. subcarrier spacing or symbol duration. In additions, some future applications, like mULC, may be better served with asynchronous transmissions. Therefore, in Chapter 6 an asynchronous uplink multi-user FBMC-QAM system is investigated in which the signal from multiple UNs arrives at the BS with different timing offsets (TO). First, the case in which UNs transmit with the same numerology is considered. This is extended to the case where UNs transmit their signals to the BS using different numerologies. In the mixed numerology case, the frequency multiplexing of multiple UNs with different numerologies causes inter-numerology interference (INI) between UNs in addition to the intrinsic interference in FBMC-QAM. To eliminate the interference terms, a novel iterative receiver is proposed based on PIC and IIC that can be applied to any coded modulation scheme with a soft-input soft-output (SISO) decoder. Specifically, the proposed receiver performs BICM-ID by combining FBMC-QAM demodulation and SISO decoding for signal detection, and PIC and IIC for interference removal.

Finally, the conclusions of the work conducted in this thesis and the potential research areas for future work are provided in Chapter 7.

1.4 Publication List

Journal Papers

1. Sumaila Mahama, Yahya Harbi, Alister Burr and David Grace, "Design and Convergence Analysis of an IIC-Based BICM-ID Receiver for FBMC-QAM Systems" *IEEE Open Journal of the Communications Society*, vol. 1, pp. 563 – 577, May 2020.

2. Sumaila Mahama, Derek Kweku Pobi Asiedu, Yahya Harbi, Kyoung Jae Lee, David Grace and Alister Burr, "Multi-User Wireless Information and Power Transfer in FBMC-Based IoT Networks," *IEEE Open Journal of the Communications Society*, vol. 2, pp. 545-563, Mar. 2021.

3. Sumaila Mahama, Yahya Harbi, David Grace and Alister Burr, "Multi-User Interference Cancellation for Uplink FBMC-based Multiple Access Channel," *IEEE Communications Letters*, vol. 25, no. 8, pp. 2733-2737, Aug. 2021.

Conference Papers

1. Sumaila Mahama, Yahya Harbi, Alister Burr and David Grace, "Iterative Interference Cancellation in FBMC-QAM Systems," in Proc. 2019 IEEE *Wireless Communications and Networking Conference (WCNC)*, Marrakesh, Morocco, pp. 1-5. Apr. 2019.

2. Sumaila Mahama, Yahya Harbi, Alister Burr and David Grace, "A Non-orthogonal Waveform Design with Iterative Detection and Decoding for Narrowband IoT Applications," in Proc. 2019 *European Conference on Networks and Communications (EuCNC)*, Valencia, Spain, pp. 315-319, June 2019.

Chapter 2

Literature Review

Initial deployment of 5G mobile communication networks is well under way in many places around the world. The full network architecture and implementation of 5G and beyond networks are a significant shift from the previous long-term evolution advanced (LTE-A) or 4G network. The key drivers and requirements of 5G and beyond networks are [26]:

- **Gigabit Wireless Connectivity**: As we head towards beyond 5G networks, peak data rates of up to 10 Gbps and cell-edge data rates close to 100 Mbps are required to satisfy eMBB applications and to improve services in areas with high user density or high mobility [1].
- **Massive Device Connectivity**: 5G and beyond networks are expected to support additional network functionalities such as mMTC. For this type of application, billions of devices will connect and interact with each other and with humans through the internet [27, 28]. mMTC will find applications in areas such as telemedicine, smart homes, smart factory, etc. Unlike eMBB applications, mMTC networks will mainly consist of low data rate sensor nodes. Moreover, the critical design requirement of mMTC networks will be to support a connection density of up to 10^6 devices per km^2 [1].
- **Energy Efficiency**: With the large number of interconnected applications and network devices, the energy consumption of future wireless networks will also grow exponentially. This will result in an increase in the cost of network operation and in some cases increase the amount of CO_2 emissions. Therefore, with the high networks density in use cases like mMTC, a high level of energy efficiency is required to keep energy consumption down and prolong the battery life of energy constrained devices [29, 30].

From the scenarios outlined above, it is clear that future network design will involve very different and sometimes contradicting system requirements. As mentioned in Chapter 1, the focus of this thesis is to investigate a new PHY waveform for future wireless networks. Therefore, in this chapter, the fundamental concepts of the techniques discussed in this thesis are introduced. First, the fundamentals of 5G numerologies are presented in Section 2.1 to serve as the general underlying framework for

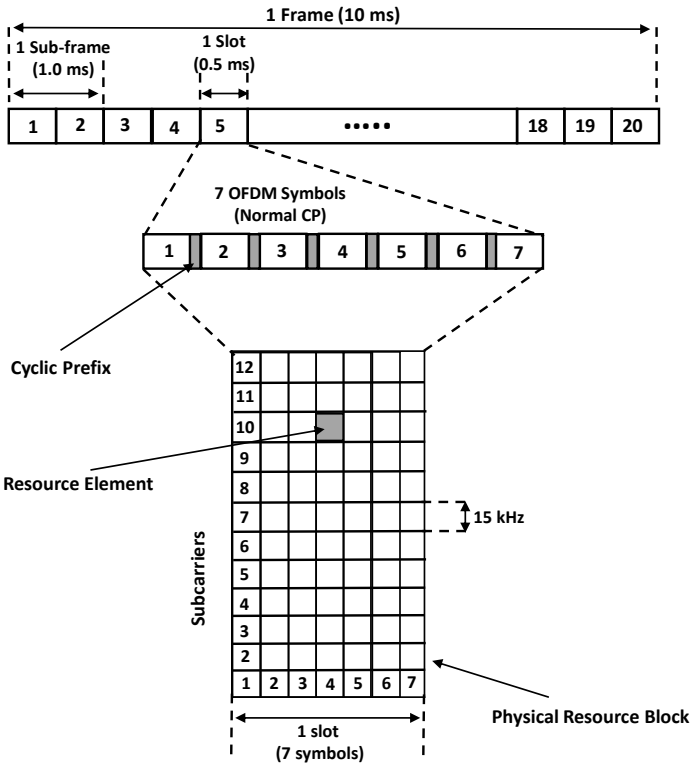

Fig. 2.1 The LTE (OFDM) DL signal frame structure.

this thesis. Next, an overview of some potential waveform candidates for beyond 5G applications are presented in Section 2.2. In Section 2.3, the basics of the wireless propagation channel employed in this thesis is presented. In addition, the basic concepts of iterative detection and decoding receivers are given in Section 2.4. Finally, the concept of EH with different receiver models is presented in Section 2.5.

2.1 5G NR

In LTE, a frame with a single OFDM numerology is designed mainly to satisfy the high data rate requirement. However, this one-size-fits-all radio frame structure cannot support the diverse requirements of the three main use cases of 5G NR. As a result, 5G NR adopts a number of scalable numerologies, defined mainly by the subcarrier spacing [31]. For example, in highly time-variant channels, larger subcarrier spacing may be needed to combat the effect of Doppler spread, while frames with smaller subcarrier spacing will be required to support the high number of devices in mMTC applications.

5G NR numerologies are designed considering the 15 kHz OFDM numerology, shown in Fig. 2.1, as the baseline. The structure shown in Fig. 2.1 represents one OFDM frame [26], which has

Table 2.1 5G NR Numerologies

μ	$\Delta f = 2^{\mu} \times 15$ kHz	Cyclic Prefix	No. of slots per subframe
0	15	Normal	1
1	30	Normal	2
2	60	Normal/Extended	4
3	120	Normal	8
4	240	Normal	16

a duration of 10 ms. Each frame consist of 10 sub-frames, each of which has two time slots. One OFDM time slot has a duration of 0.5 ms. Moreover, there are two different implementations of CP in the LTE frame structure design. The first case is the normal CP implementation in which each time slot contains seven OFDM symbols. The other case is the extended CP implementation, which consist of six OFDM symbols within each time slot. In the frequency domain, the LTE specifications define channel bandwidths ranging from 1.4 MHz to 20 MHz. The channel bandwidth is divided into chunks of subchannels known as Physical Resource Blocks (PRBs). Each PRB is made up of 12 subcarriers, each having a subcarrier spacing of 15 kHz. The total number of available PRBs depends on the selected LTE channel bandwidth. For example, the 1.4 MHz channel bandwidth has 6 PRBs, i.e. 72 active subcarriers.

The other numerologies used in 5G NR are obtained by scaling the baseline numerology using a scaling factor. In general, scaling the baseline numerology by a power of two is adopted in order to maintain the symbol boundaries across numerologies, which simplifies the multiplexing of multiple numerologies on the same frequency band. Specifically, the subcarrier spacing of different numerologies in 5G NR scales as $2^{\mu} \times 15$ kHz. In the time domain, the number of symbols in each time slot is 14. However, since the subcarrier spacing has an inverse relation to the symbol duration the number of time slots within a single subframe varies with the scaling factor, μ. That is, as the subcarrier spacing increases, the symbol duration decreases and therefore each subframe can accommodate more symbols. The OFDM numerologies standardized for 5G NR are represented in Table 2.1.

As mentioned above, a number of numerologies can be transmitted on the same carrier frequency, by dividing the available bandwidth into different bandwidth parts (BWPs). The BWPs maybe be assigned to UNs with different applications and different numerologies. In an OFDM-based mixed numerology system, subcarrier orthogonality exists only between subcarriers within a BWP (with the same subcarrier spacing). Subcarriers from one numerology may leak energy into subcarriers of other numerologies, which causes INI to adjacent subcarriers. In addition, OOB emissions from nearby BWPs with different numerologies can destroy the subcarrier orthogonality within a particular BWP, which also causes INI. An illustration of the a mixed numerology system is shown in Fig. 2.2. Considering the numerology μ^i in Fig. 2.2 as an example, it can be seen that the numerology with

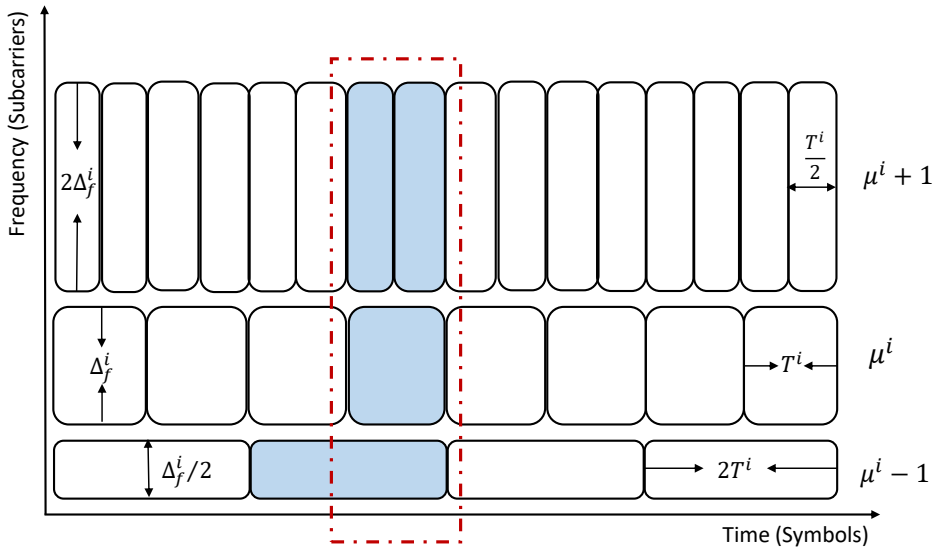

Fig. 2.2 Symbol overlap in a multi-numerology system

smaller subcarrier spacing ($\mu^i - 1$) has a longer symbol duration and a part of it overlaps with the one symbol of numerology μ^i. In addition, the numerology with larger subcarrier space ($\mu^i + 1$) has a shorter symbol duration such that two symbols of numerology $\mu^i + 1$ overlap with one symbol of numerology μ^i. This complicates the symbol overlap and causes INI. To get rid of INI, guard bands can be inserted between neighbouring BWPs. However, this comes at the cost of reduced spectral efficiency. Alternatively, new waveforms that are more suitable for asynchronous transmissions and support much lower OOB emissions, such as FBMC, may fit multi-numerology systems better.

2.2 Waveform Candidates for Future Applications

Multicarrier modulation has been widely adopted for current wireless communication systems due to its robustness against the time and frequency selectivity of the wireless propagation channel. In multicarrier transmissions, the information signal is distributed over multiple narrowband sub-channels (subcarriers) to create the transmitted broadband signal. As a result, the broadband propagation channel can be modelled as a group of narrowband propagation channels. Moreover, each element of the narrowband channel can be considered to be a flat fading channel, enabling the implementation of a simple one-tap equalizer at the receiver. In this section, an overview of some candidate multicarrier waveforms for future applications are presented.

2.2.1 OFDM

OFDM modulation was first introduced in [32] as an evolution to Frequency-Division Multiplexing (FDM), by using orthogonal pulse shapes to multiplex data in the frequency domain. It has seen

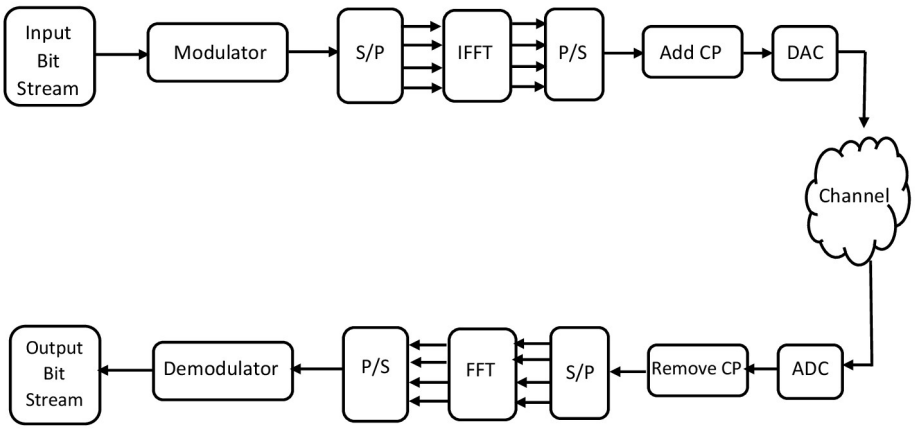

Fig. 2.3 Block diagram of OFDM transceiver

widespread application in existing communication systems such as Digital Video Broadcasting (DVB), WiFi and LTE-A [33–35]. OFDM and its multiple access technique, orthogonal frequency division multiple access (OFDMA), were standardized for 4G due to the many advantages they offered compared to code division multiple access (CDMA), which was used in 3G, including robustness to multipath fading, efficient implementation and higher spectral efficiency.

The structure of a conventional OFDM transceiver is shown in Fig. 2.3. At the OFDM transmitter, a stream of modulated data is multiplexed over M consecutive subcarriers to form one OFDM symbol. The subcarriers are separated from each other by a frequency spacing, F_0. Each symbol, with duration $T_0 = 1/F_0$, is separated from other symbols by a guard interval to avoid ISI. The guard interval can be implemented by either zero-padding (ZP) or CP. In the case of CP, a specific period from the tail of each symbol is copied and appended to the beginning of that symbol [36]. Note that to avoid ISI the CP duration, T_{CP}, must be longer than the channel impulse response. Denoting $x_{n,m}$ as the data carried by subcarrier m of symbol n, the time-domain OFDM modulated signal at the transmitter can be represented by

$$x(l) = \sum_{n=0}^{N-1} \sum_{m=0}^{M-1} x_{n,m} g_{n,m}(l) \qquad l = 0, 1 \ldots M \tag{2.1}$$

where N is the number of OFDM symbols, M is the number of subcarriers and

$$g_{n,m}(l) = g^T(l - nM_s) e^{\frac{j2\pi ml}{M}} \tag{2.2}$$

with $M_s = M + M_{CP}$ being the symbol duration in samples and $g^T(l)$ as the prototype filter impulse response. In OFDM, a rectangular pulse-shaped filter is employed as the prototype filter, which is given as [37]

$$g^T(l) = \begin{cases} \frac{1}{\sqrt{M}}, & \text{if } -\left(\frac{M}{2} + M_{CP}\right) \leq l < \frac{M}{2}. \\ 0, & \text{otherwise.} \end{cases} \tag{2.3}$$

Assuming a noiseless back-to-back connection, the received signal at time-frequency point (n', m') after receiver processing is given as

$$y_{n',m'} = \sum_{l=0}^{M_s-1} x(l)\tilde{g}_{n',m'}(l) \tag{2.4}$$

where

$$\tilde{g}_{n',m'}(l) = g^R(l - n'M_s)e^{-\frac{j2\pi m' l}{M}} \tag{2.5}$$

with $g^R(l)$ as the receiver prototype filter response which is expressed as

$$g^R(l) = \begin{cases} g^T(l), & M_{CP} \leq l \leq M + M_{CP} - 1 \\ 0, & 0 \leq l \leq M_{CP} - 1. \end{cases} \tag{2.6}$$

Substituting (2.1) into (2.4), we obtain

$$\begin{aligned} y_{n',m'} &= \sum_{l=0}^{M_s-1} \sum_{n=0}^{N-1} \sum_{m=0}^{M-1} x_{n,m} g_{n,m}(l) g^*_{n',m'}(l) \\ &= \sum_{n=0}^{N-1} \sum_{m=0}^{M-1} x_{n,m} I_{n,m}^{n',m'} \end{aligned} \tag{2.7}$$

with

$$\begin{aligned} I_{n,m}^{n',m'} &= \sum_{l=0}^{M_s-1} g_{n,m}(l) g^*_{n',m'}(l) \\ &= \sum_{l=0}^{M_s-1} g^T(l - nM_s) g^R(l - n'M_s) e^{\frac{j2\pi(m-m')l}{M}} \\ &= e^{\frac{j2\pi(m-m')n'M_s}{M}} \sum_{l=l_0}^{l_1} g^T(l - (n-n')M_s) g^R(l) e^{\frac{j2\pi(m-m')l}{M}} \end{aligned} \tag{2.8}$$

where $l_0 \triangleq \max(0, (n-n')M_s)$, $l_1 \triangleq \min(M-1, M-1+(n-n')M_s)$. As can be seen from the last expression in (2.8), $I_{n,m}^{n',m'}$ depends on the differences in time and frequency positions $v = n - n'$ and $u = m - m'$, respectively. Therefore, (2.8) can be rewritten as

$$I_{v,u} = \phi^{un'} \sum_{l=l_0}^{l_1} g^T(l - vM_s) g^R(l) e^{\frac{j2\pi ul}{M}} \tag{2.9}$$

where $\phi = e^{\frac{j2\pi M_s}{M}}$. For the rectangular pulse filter employed in OFDM, $I_{v,u} = 0$ for any time-frequency position with $(v,u) \neq 0$. This implies that, with long enough CP under ideal channel conditions OFDM has no ISI and ICI [38].

Note that the exponential expression in (2.2) and its complex conjugate in (2.5) represent the Inverse Discrete Fourier Transform (IDFT) and Discrete Fourier Transform (DFT) at the transmitter and receiver, respectively [39]. In practical systems, the Inverse Fast Fourier Transform (IFFT) and Fast Fourier Transform (FFT) has been used to implement the IDFT and DFT, respectively, due to the low implementation complexity of FFT/IFFT [40].

Due to the many advantages of OFDM, such as ease of implementation and backward compatibility with the existing 4G network, it has been maintained as the standard waveform for 5G NR. OFDM is well suited for eMBB applications that require synchronous, high data rate transmission on the downlink. However, for some future applications, especially mMTC applications, some shortcomings of OFDM render it ineffective. These include:

1. High OOB emissions due to the use of rectangular filters in OFDM, which causes interference to adjacent frequency bands which may be allocated to other mMTC nodes. In addition, this can negatively affect the exploitation of non-contiguous spectrum for carrier aggregation in future networks.

2. High sensitivity of OFDM to synchronisation errors. For most mMTC applications, the traffic will be dominated by uplink transmissions from a large number of distributed nodes. In such a scenario, it is difficult to maintain synchronous communications and therefore errors occur in terms of timing and frequency offsets [18]. The high sensitivity of OFDM to synchronisation errors will cause interference in asynchronous transmissions. Therefore, in asynchronous applications, one of OFDM's main advantages in the form interference avoidance is lost.

3. Although OFDM has a high spectral efficiency compared to waveforms used in previous generations of mobile networks, the need for CP and the high OOB leakage at the spectrum edges limit its spectral efficiency. New waveform technique that can further improve the spectral efficiency and make better use of the available spectrum for connecting the billions of expected devices in mMTC applications are therefore needed.

4. The strict synchronization procedure designed to meet the orthogonality constraints of OFDM introduces a considerable level of control overhead in the network. In particular, to enable the real-time tactile interaction in future wireless networks, a massive number of distributed nodes (access points and UNs) must be deployed. With such a massive number of node deployments in the network, the grant-based synchronization procedure required in OFDM systems would generate huge signalling overhead. In this regard, waveform techniques that facilitate asynchronous and grant-free transmissions are promising for future applications [6, 7].

As a result of the above shortcomings, OFDM is not the most efficient waveform for all possible use cases of future networks. Considering mMTC scenarios in which multiple UNs may transmit asynchronously, OFDM may not be an effective waveform. Thus, a number of new candidate waveforms, some of which are described below, have been investigated for such use cases.

2.2.2 Filtered OFDM

The rectangular pulse-shaped filter used in OFDM systems results in high OOB emission. To address this problem, filtered OFDM (f-OFDM) has been proposed [41, 42]. At the transmitter of a f-OFDM system, a filtering operation is implemented after OFDM processing in order to suppress the high OOB emission caused by the rectangular filter. The filtering process is implemented over an entire frequency band which reduces the spectrum leakage to adjacent frequency bands and improve the spectral efficiency of OFDM. At the receiver side, a similar filtering operation is employed before OFDM demodulation to deal with inter-user interference. In order to achieve the promised OOB emission performance, properly designed filters are required. In general, the filter design involves a trade-off between time localization, frequency localization and implementation complexity. Controlling the time-domain energy spread can reduce ISI, whereas the improved localization in the frequency domain can increase the spectral efficiency and reduce leakage interference. To satisfy all three design constraints, a sinc pulse is usually employed as the filter in f-OFDM. However, the impulse response of a sinc function is infinitely long. Therefore, for practical implementation, the sinc function is multiplied by a window function to provide a soft truncation of the filter. As a result, the impulse of the filter fades out quickly, and therefore limits the the ISI introduced between consecutive f-OFDM symbols. The most popular window function used in f-OFDM is the Hann window. However, other window functions such as the Root-raised-cosine (RRC) window can also be used [41].

Although in f-OFDM systems additional filtering is applied to address the high OOB emission problem in OFDM, the orthogonality and synchronisation requirements, characteristic of OFDM, are maintained. This implies that some of the problems with OFDM, such as the huge signalling overhead in synchronous transmissions will still exist in f-OFDM.

2.2.3 Generalized Frequency-Division Multiplexing (GFDM)

GFDM is a block-filtered multicarrier modulation scheme, which transmits data across multiple subsymbols per subcarrier in a time-frequency block structure [43, 44]. In GFDM systems, circular pulse shaping is applied to individual subcarriers consisting of a block of data symbols. By choosing a single subsymbol per subcarrier and applying a rectangular pulse shape filter, GFDM resembles OFDM [26]. The circularity property of the prototype filter enables GFDM to introduce a CP and use frequency-domain equalization (FDE) to combat the effect of multipath propagation and limit the interference between different blocks. In addition, GFDM can be designed to reduce the OOB emissions, in order to limit interference to users in adjoining subbands. One way to achieve this is to

use time windowing at the GFDM transmitter [45–47]. However, the use of circular filtering results in non-orthogonality between subcarriers, which introduces both ISI and ICI. Two main receiver designs have been studied in the literature for GFDM: the matched filter (MF) and zero forcing (ZF) [47]. The MF receiver maximises the per subcarrier signal-to-noise ratio (SNR) but with the negative effect of introducing intrinsic interference when the filter cannot achieve orthogonality. The ZF receiver, on the other hand, can completely eliminate the intrinsic interference but at the cost of noise enhancement. As a compromise between self-interference and noise enhancement, the minimum mean-squared error (MMSE) receiver has also been applied to GFDM systems. However, the MMSE receiver increases the computational complexity of the GFDM systems compared to MF or ZF receivers.

Considering a modulated data block $\mathbf{d}$ of N elements, the GFDM modulator decomposes it into M subcarriers, each having Q subsymbols, i.e. $\mathbf{d} = \left(\mathbf{d}_0^T, \ldots, \mathbf{d}_{Q-1}^T\right)^T$ with $\mathbf{d}_q = (d_{0,q}, \ldots, d_{M-1,q})^T$. Here, the individual element $d_{m,q}$ represents the data transmitted on the m-th subcarrier in the q-th GFDM subsymbols. In matrix notation, one GFDM transmitted data block can be written as

$$\mathbf{d} = \begin{pmatrix} d_{0,0} & \ldots & d_{0,N-1} \\ \vdots & \ddots & \vdots \\ d_{M-1,0} & \ldots & d_{M-1,N-1} \end{pmatrix} \tag{2.10}$$

2.2.4 FBMC-OQAM

To address the large OOB emission typically associated with OFDM transmission, FBMC systems have been proposed, which apply per-subcarrier filtering using enhanced linear filters at both the transmitter and receiver [48, 49]. The use of an advanced prototype filter makes FBMC systems highly localized in the frequency domain, and therefore less sensitive to asynchronous transmissions. Also, FBMC improves spectral efficiency, compared to OFDM, by removing the CP. However, the per-subcarrier filtering in the frequency domain of FBMC results in long filter tails in the time domain. In order to achieve maximum data rate, adjacent symbols overlap in the time domain, which causes a loss of subcarrier orthogonality. To maintain the orthogonality between subcarriers, the in-phase component of a complex QAM symbol is mapped to the first time slot and the quadrature component to the second time-slot. This is known to as offset QAM (OQAM), the term offset referring to the time shift of half the symbol period between the real and imaginary parts of a complex QAM symbol [11, 18]. As shown in Fig. 2.4, the OQAM processing at the transmitter side first separates the complex valued signal $c_{n,m}$ into two real valued symbols $d_{n,m}$ and $d_{n+1,m}$ as:

$$d_{n,m} = \begin{cases} \Re\{c_{n,m}\}, & \text{if } m \text{ is even.} \\ \Im\{c_{n,m}\}, & \text{if } m \text{ is odd.} \end{cases} \tag{2.11}$$

$$d_{n+1,m} = \begin{cases} \Im\{c_{n,m}\}, & \text{if } m \text{ is even.} \\ \Re\{c_{n,m}\}, & \text{if } m \text{ is odd.} \end{cases} \tag{2.12}$$

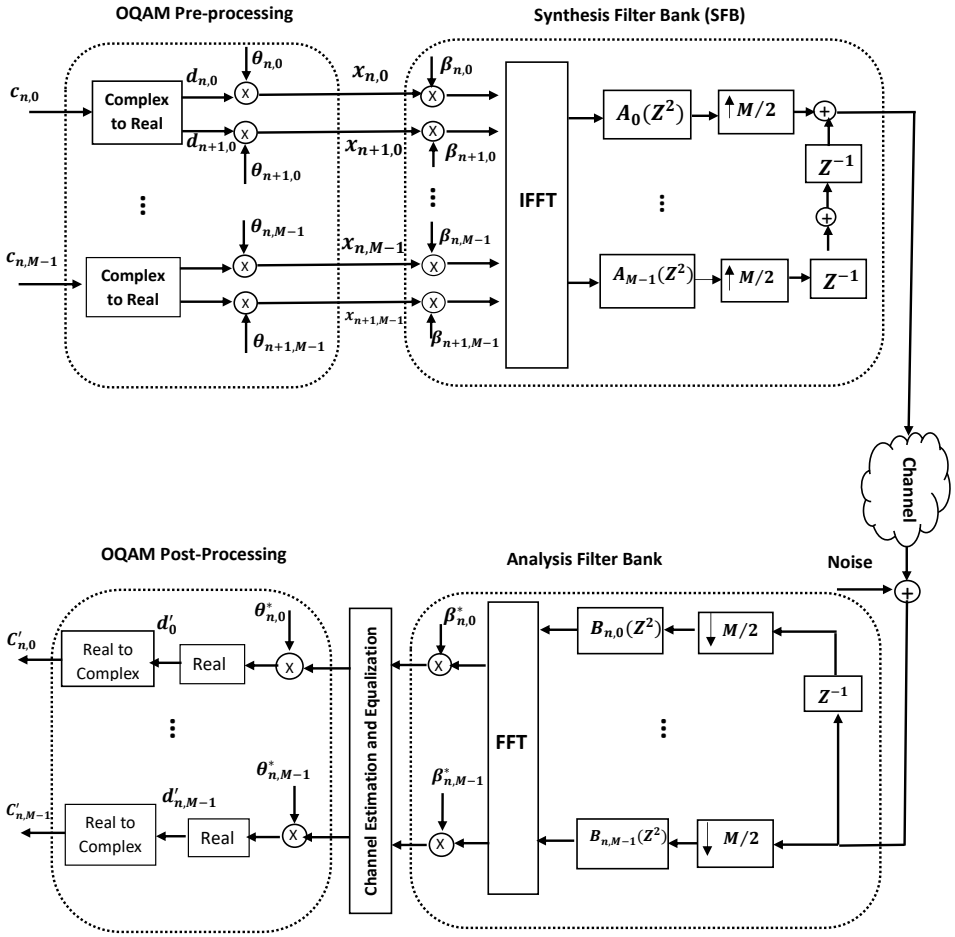

Fig. 2.4 Block diagram of FBMC-OQAM transceiver

The real-valued signals are then multiplied by a phase mapping coefficient $\theta_{n,m}$ to obtain the modulated signal as

$$x_{n,m} = d_{n,m}\theta_{n,m} \tag{2.13}$$

Generally, $\theta_{n,m}$ is of the form [50]

$$\theta_{n,m} = j^{(n+m)} = \begin{cases} \pm 1, & \text{if } m+n \text{ is even.} \\ \pm j, & \text{if } m+n \text{ is odd.} \end{cases} \tag{2.14}$$

Thus, the time-domain FBMC-OQAM modulated signal after transmit filtering can be represented by

$$x(l) = \sum_{n=0}^{N-1} \sum_{m=0}^{M-1} x_{n,m} g_{n,m}(l) \qquad l = 0, 1 \ldots L_p \tag{2.15}$$

where $g_{n,m}(l)$ is the transmit filter or synthesis filter bank (SFB), N is the total number of symbols, M is the total number of subcarriers and $L_p = DM - 1$. D is an integer usually referred to as the overlapping factor. The implementation of the SFB is mainly dependent upon the prototype filter employed at the transmitter. The synthesis filter can be expressed as

$$g_{n,m}(l) = p(l)e^{j\frac{2\pi m}{M}\left(l-\frac{L_p-1}{2}\right)} \tag{2.16}$$

where $p(l)$ is the prototype filter impulse response, $l = 0,1,\ldots,L_p-1$. An efficient implementation of the FBMC-OQAM transceiver structure can be achieved by the combination of IFFT/FFT and polyphase network (PPN), which is shown in Fig. 2.4. In the PPN case, the filter design depends on the periodicity of the modulation function [50]. In (2.16), the modulation function is given as

$$\begin{aligned} e_{m,l} &= e^{j\frac{2\pi m}{M}\left(l-\frac{L_p-1}{2}\right)} \\ &= e^{-j\frac{2\pi m}{M}\left(\frac{L_p-1}{2}\right)} e^{j\frac{2\pi kl}{M}} \\ &= \beta_l \Theta_{m,l} \end{aligned} \tag{2.17}$$

The periodicity of this function is M since $\Theta_{m,q+tM} = \Theta_{m,q}$, where $q = 0,1,\ldots,M-1$ and $t = 0,1,\ldots,D-1$. The polyphase representation of the synthesis filter is thus expressed as

$$\begin{aligned} G_m(z) &= \sum_{l=0}^{L_p-1} p(l)e_{m,l}z^{-l} \\ &= \sum_{q=0}^{M-1}\sum_{t=0}^{D-1} p(q+tL_p)\beta_l\Theta_{m,q+tL_p}z^{-(m,q+tL_p)} \\ &= \sum_{q=0}^{M-1} \beta_l\Theta_{m,q}z^{-q}\sum_{t=0}^{D-1} p(q+tL_p)z^{-tL_p} \\ &= \sum_{q=0}^{M-1} \beta_l\Theta_{m,q}z^{-q}A_q(z^{L_p}) \end{aligned} \tag{2.18}$$

Putting all synthesis filters together we have

$$\mathbf{G}(z) = \mathbf{B}\cdot\mathbf{W}\cdot\mathbf{A}(z^M)\cdot\mathbf{c}(z) \tag{2.19}$$

where

$$\begin{aligned}
\mathbf{G}(z) &= [G_0(z)\, G_1(z) \cdots G_{M-1}(z)]^T, \\
\mathbf{B} &= diag[\beta_0\, \beta_1 \cdots \beta_{L_p-1}], \\
\mathbf{W} &= diag[\Theta_{0,q}\, \Theta_{1,q} \cdots \Theta_{L_p,q}] \\
\mathbf{A}(z^{L_p}) &= diag[A_0(z^{L_p})\, A_1(z^{L_p}) \cdots A_{L_p-1}(z^{L_p})], \\
\mathbf{c}(z) &= [1\, z^{-1} \cdots z^{-(L_p-1)}]
\end{aligned}$$

At the receiver, the real-valued output signal can be obtained by applying receive filtering or analysis filter bank (AFB), multiplication by the complex conjugate of $\theta_{n,m}$ followed by taking the real part. Assuming a noiseless back-to-back connection, the received signal at time-frequency point (n',m') after receive filtering is given as

$$y_{n',m'} = \sum_{l=0}^{M_s-1} x(l)\tilde{g}_{n',m'}(l) \tag{2.20}$$

Ideally, prototype filters are designed to satisfy the perfect reconstruction (PR) condition. However, in practical systems it is impossible to achieve the PR condition due to the effect of multipath fading channels. For such systems, it is sufficient for prototype filters to satisfy the near perfect reconstruction (NPR) characteristics. To achieve this, the AFB is chosen to be the complex conjugate and time reversed version of the SFB [51]. The analysis filter is thus expressed as

$$\begin{aligned}
\tilde{g}_{n,m}(l) &= g^*_{n,m}(L_p-1-l) \\
&= p(L_p-1-l)e^{j\frac{2\pi m}{M}\left(l-\frac{L_p-1}{2}\right)}
\end{aligned} \tag{2.21}$$

Following the definition in (2.18), the polyphase representation of the analysis filter can be expressed as

$$\begin{aligned}
\tilde{G}_m(z) &= \sum_{m=0}^{L_p-1} p(L_p-1-l)e_{m,l}z^{-l} \\
&= \sum_{q=0}^{M-1} \beta_l \Theta_{m,q} z^{L_p-1-q} A_{L_p-1-q}(z^{L_p})
\end{aligned} \tag{2.22}$$

The corresponding matrix notation is given by

$$\tilde{\mathbf{G}}(z) = \mathbf{B}\cdot\mathbf{W}\cdot\mathbf{A}(z^M)\cdot\mathbf{c}(z) \tag{2.23}$$

where $\tilde{\mathbf{G}}(z) = [\tilde{G}_0(z)\, \tilde{G}_1(z) \cdots \tilde{G}_{M-1}(z)]^T$. The real-valued output is therefore given by

$$\hat{d}_{n,m} = \Re\{y_{n',m'}\theta^*_{n,m}\} \tag{2.24}$$

Finally, the estimated complex-valued symbol can then be obtained as

$$\hat{c}_{n,m} = \begin{cases} \hat{d}_{n,m} + j\hat{d}_{n+1,m}, & \text{if } m \text{ is even.} \\ \hat{d}_{n+1,m} + j\hat{d}_{n,m}, & \text{if } m \text{ is odd.} \end{cases} \tag{2.25}$$

The enhanced filtering on each subcarriers makes FBMC-OQAM systems very localised in the frequency domain, which reduces the sensitivity to asynchronous transmissions. However, as mentioned above, FBMC-OQAM systems achieve orthogonality only in the real domain and suffers from intrinsic interference caused by the imaginary part of the complex signal. Moreover, in a highly frequency selective channel, the real orthogonality maybe be lost, resulting in ISI and ICI. Furthermore, the OQAM processing limits the implementation of conventional LTE-based schemes such as channel estimation, STBC and MLD [13]. To resolve the problems in FBMC-OQAM, the transmission of complex QAM symbols in FBMC systems was proposed in [14, 19]. By transmitting QAM signals, the FBMC systems cannot guarantee complex domain orthogonality, resulting in intrinsic interference. The details of FBMC-QAM are presented in the next subsection.

2.2.5 FBMC-QAM

FBMC-QAM systems transmit complex QAM symbols, instead of OQAM, in order to resolve some of the difficulties associated with FBMC-OQAM [14, 19, 52]. However, the FBMC-QAM system cannot guarantee complex domain orthogonality, resulting in intrinsic interference. In order to restore orthogonality in FBMC-QAM, the authors in [19] and [52] proposed a twin-filter model that together satisfy complex orthogonality in ideal channels. This is achieved by separating the QAM symbols at the transmitter into even and odd-numbered subcarrier parts and applying different prototype filters to the two parts, as shown in Fig. 2.5. Thus, the signal to be transmitted can be expressed as

$$x(l) = \sum_{n=0}^{N-1} \sum_{m=0}^{M-1} (x^e_{n,2m} \mathrm{g}^e_{n,2m}(l) + x^o_{n,2m+1} \mathrm{g}^o_{n,2m+1}(l)) \tag{2.26}$$

where $x^e_{n,2m}$ and $x^o_{n,2m+1}$ refer to the even and odd-numbered subcarrier components of the transmit signal respectively, with $\mathrm{g}^e_{n,2m}$ and $\mathrm{g}^o_{n,2m+1}$ as the even and odd prototype filters respectively, given as

$$\mathrm{g}^e_{n,2m}(l) = p^e(l) e^{j\frac{2\pi}{M}(2l)(l-\frac{L_p-1}{2})},\ l \in \{0,1,\ldots,L_p/2-1\} \tag{2.27}$$

$$\mathrm{g}^o_{n,2m+1}(l) = p^o(l) e^{j\frac{2\pi}{M}(2m+1)(l-\frac{L_p-1}{2})},\ l \in \{0,1,\ldots,L_p/2-1\}. \tag{2.28}$$

Different types of prototype filters can be adopted in FBMC-QAM. In [52], the PHYDYAS prototype filter in [11] was used for even subcarriers. In [53], the power spectral densities (PSDs) of different prototype filters are compared and the results show that the PHYDYAS prototype filter has the fastest sidelobe attenuation speed (i.e. low OOB emission). This justify the popularity of the PHYDYAS filter in FBMC systems. The prototype filter coefficients of the PHYDYAS prototype filter can be

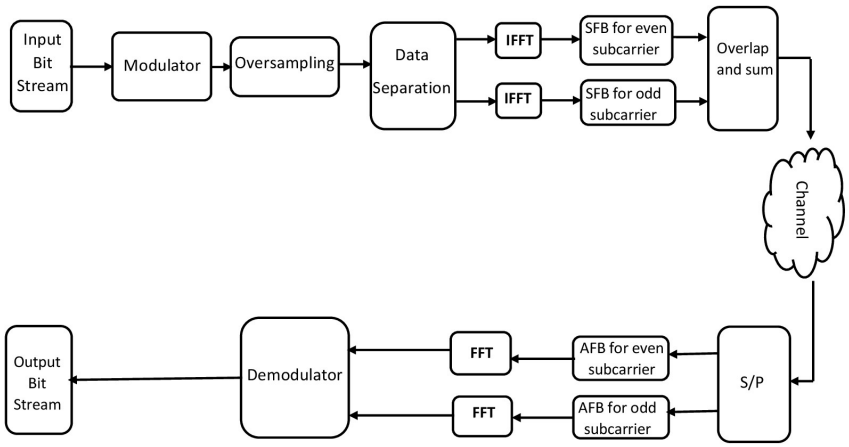

Fig. 2.5 Block diagram of FBMC-QAM transceiver

expressed as [54]

$$p^e(l) = G_0 + 2\sum_{i=1}^{3} G_i \cdot cos\left(\frac{2\pi}{L_p} il\right), \tag{2.29}$$

where the coefficients of the filter are given as $G_0 = 1, G_1 = 0.97196, G_2 = \sqrt{2}/2$ and $G_3 = 0.235147$. In vector form, the prototype filter can be represented as

$$\begin{aligned} \mathbf{p}^e &= [p^e(0)\ p^e(1)\ \cdots\ p^e(L_p-1)] \\ &= \left[\mathbf{p}^e_{(0)}\ \mathbf{p}^e_{(1)}\ \cdots\ \mathbf{p}^e_{(2K-1)}\right] \end{aligned} \tag{2.30}$$

where $\mathbf{p}^e_{(i)}$ is a sub-block of $\mathbf{p}^e$ with length $L_p/2$. The prototype filter of the odd subcarriers is obtained from that of the even subcarriers by block interleaving [19] and is expressed as

$$\begin{aligned} \mathbf{p}^o &= \left[\mathbf{p}^e_{(2K-1)}\ \mathbf{p}^e_{(2K-2)}\ \cdots\ \mathbf{p}^e_{(0)}\right] \\ &= [p^o(0)\ p^o(1)\ \cdots\ p^o(L_p-1)] \end{aligned} \tag{2.31}$$

At the receiver side, the processing at the transmitter is reversed to obtain the demodulated FBMC-QAM symbols.

Note that, even though the FBMC-QAM with dual prototype filters achieve complex orthogonality in ideal channel conditions, intrinsic interference arises under fading channel conditions. Also, the filter design in [19] and [52] cause filter coefficient discontinuities which result in higher OOB emissions compared to OFDM. As a result, FBMC-QAM with a single prototype filter on all subcarriers is investigated in this thesis. This approach can improve spectral confinement of FBMC-QAM at the cost of the loss of complex orthogonality between subcarriers. This is because multicarrier systems cannot achieve orthogonality, frequency localization and maximum symbol density simultaneously

Table 2.2 Waveform Comparison

Characteristics	OFDM	f-OFDM	GFDM	FBMC-OQAM	FBMC-QAM
OOB emission	Poor	Good	Good	Very Good	Very Good
Spectral efficiency	High	High	High	Very High	Very High
MIMO compatibility	High	High	High	Low	High
Robustness to asynchronous interference	Poor	Poor	Good	Very Good	Very Good
Cyclic prefix	Present	Present	Present	Absent	Absent

[15]. The aim of this these is to propose various interference cancellation receivers to address the intrinsic interference problem that results from the loss of orthogonality.

2.2.6 Waveform Comparison for Future Applications

As mentioned above, OFDM has many advantages that makes it suitable for eMBB applications. However, the diverse nature of future applications such as those discussed in Chapter 1, will require a waveform that can support the huge connection density with lower signalling overhead. The well-localized prototype filters employed in FBMC systems imply that, for applications like mMTC, the billions of expected devices can transmit in a grant-free or asynchronous manner. This means that resources that might otherwise be used to maintain synchronous access can be used for data transmissions. A comparison of candidate waveforms for future wireless networks is presented in Table 2.2 in terms of OOB emission, spectral efficiency, MIMO compatibility, robustness to asynchronous interference and the use of CP. Note that, here spectral efficiency is defined in terms of how effectively a particular waveform utilizes the available spectrum. Based on the high spectral efficiency, suitability to asynchronous access and compatibility with conventional MIMO techniques, FBMC-QAM is investigated in this thesis as an alternative to OFDM in future wireless networks.

2.3 Wireless Propagation Channel Modelling

One major advantage of multicarrier waveforms like OFDM and FBMC is their robustness against multipath channel selectivity, which is one reason why multicarrier modulation has been adopted for various wireless communication system [55–58]. In mobile communications research, statistical models are used to simulate the wireless propagation channel, which mainly represents the characteristics of the physical transmission medium between a transmitter and a receiver in wireless networks. An understanding of the channel model is very essential in evaluating the performance of any broadband wireless communication system. Practically, the transmitted electromagnetic signal is reflected and scattered by physical objects before it arrives at the intended receiver. This causes a phenomenon known as multipath propagation, in which multiple copies of the transmitted signal arrive at the

receiver from different directions. Each component of the multipath channel represents an attenuated and delayed version of the transmitted signal. Moreover, the level of attenuation and delay in each multipath component is dependent on the nature of the physical obstacles it encounters and also on the propagation distance between the transmitter and receiver. Assume that the received signal is the sum of L_{ch} paths, with the l-th path, $l \in [0, L_{ch}-1]$ described by the delay τ_l and by a time-domain channel impulse response $h_l(t)$.

The frequency variations in the propagation channel can be quantified by the coherence bandwidth, B_c [59]. The term coherence bandwidth refers to the frequency range over which the propagation channel can be considered "flat" or invariant in the frequency domain. That is, two frequencies of a received signal are likely to experience two different propagation channels when they are separated by a bandwidth much greater than the coherence bandwidth, i.e. $B >> B_c$. This phenomenon is known as frequency selectivity [60].

In the time domain, the variation in $h_l(t)$ is caused by the mobility of the transmitter or receiver as a result of the Doppler effect. This implies that the channel varies with time and the variance is higher if the transmitter or receiver is moving at a faster speed. The level of variations in $h_l(t)$ can be estimated by the coherence time, T_c, such that $h_l(t)$ can be considered to be invariant over a duration T if it is much less than the coherence time. Therefore, two received signals are likely to have different propagation channels if they are separated by a duration much greater than the coherence time, i.e. $T >> T_c$. This phenomenon is known as time selectivity [60]. A wireless channel that is both time and frequency selective is commonly referred to as a doubly-selective channel [61–63]. Two statistical channel models employed in wireless communication are presented in the next subsections.

The 3rd Generation Partnership Project (3GPP) consortium has played a key role in the success of geometric channel models in mobile communication networks by providing standardized channel models to evaluate network performance. The models cover propagation scenarios such as suburban macro–cellular, urban macro–cellular and urban micro–cellular. For LTE, there are three main types of standardized multipath channel models. They are classified based on low, moderate, and high multipath delay spread and Doppler spread [64, 65]. The low delay spread channel model is known as the Extended Pedestrian A (EPA) model, and is used to simulate urban environments with low delay spread. The Extended Vehicular A (EVA) model represents the medium delay spread channel. Finally, the Extended Typical Urban (ETU) model is the high delay and Doppler spread channel and is used to simulate the extreme urban, suburban and rural environments. The channel models are employed for the system simulation in this thesis due to the similarity of considered propagation environment to that of LTE. The delay and power profiles of the three channels are shown in Table 2.3. Note that the three channel models mentioned above are developed using statistical channel modelling, two of which are presented in the next subsections.

Table 2.3 LTE Channel Delay and Power Profile

Delay (*ns*)			Power (*dB*)		
EPA	EVA	ETU	EPA	EVA	ETU
0	0	0	0	0	-1.0
30	30	50	-1.0	-1.5	-1.0
70	150	120	-2.0	-1.4	-1.0
90	310	200	-3.0	-3.6	0
110	370	230	-8.0	-0.6	0
190	710	500	-17.2	-9.1	0
410	1090	1600	-20.8	-7.0	-3.0
	1730	2300		-12.0	-5.0
	2510	5000		-16.9	-7.0

2.3.1 Clarke's Channel Model

The Wide-Sense Stationary-Uncorrelated Scattering (WSSUS) channel model has been widely adopted for modelling wireless communication channels [66–71]. The classical WSSUS channel model was presented in [72], where a theoretical reference model of isotropic scattering for narrowband cellular channels is derived based on the following assumptions:

- The transmitted signal has a vertical polarization.
- The received signal is a superposition of signals coming from L_{ch} propagation paths.
- The angles of arrival of the L_{ch} propagation paths are independent of each other and having some arbitrary probability density function (PDF).
- In the absence of a dominant line of sight (LOS) propagation, the L_{ch} arriving signals have constant and equal amplitudes.

Based on these assumptions, the normalised complex two-dimensional (2-D) frequency-flat fading channel of the L_{ch} paths arriving at a receiver node can be expressed as [72, 73]

$$\begin{aligned} h(t) &= \frac{1}{\sqrt{L_{ch}}} \sum_{l=1}^{L_{ch}} \exp\left[j(\omega_d t \cos(\alpha_l) + \phi_l)\right] \\ &= h_R(t) + j h_I(t) \end{aligned} \tag{2.32}$$

where

$$h_R(t) = \frac{1}{\sqrt{L_{ch}}} \sum_{l=1}^{L_{ch}} \cos(\omega_d t \cos(\alpha_l) + \phi_l) \tag{2.33}$$

$$h_I(t) = \frac{1}{\sqrt{L_{ch}}} \sum_{l=1}^{L_{ch}} \sin(\omega_d t \cos(\alpha_l) + \phi_l) \tag{2.34}$$

with $\omega_d = 2\pi f_d$, f_d is the Doppler frequency, α_l and ϕ_l represents the angle of arrival and initial phase, respectively, of the l-th propagation path. Note that α_l is uniformly distributed over $[-\pi, \pi]$.

2.3.2 Jakes' Channel Model

The Clarke's channel model was simplified to the Jakes' channel model by using a sum of sinusoids modelling approach [74]. However, Jakes' model does not satisfy all the statistical properties of Clarke's model. As a result, Jakes' model does not represent a wide-sense stationary (WSS) channel model [75, 76]. Many modifications have been proposed to improve the statistical properties of the Jakes' model [73, 75–79]. Moreover, Jakes' model and its modifications have a lower computational complexity compared to Clarke's model, with a smaller number of low-frequency oscillators. Hence, Jakes' model is often employed for modelling the wireless propagation channel [74, 80]. To simplify Clarke's model and provide a deterministic model, Jakes' model employs some simplified assumptions on the channel model parameters used in Clarke's model [81]. These assumptions can be expressed as:

$$\alpha_l = \frac{2\pi l}{L_{ch}}, \qquad l = 1, 2, \ldots, L_{ch} \tag{2.35}$$

$$\phi_l = 0, \qquad l = 1, 2, \ldots, L_{ch} \tag{2.36}$$

$$L_{ch} = 4L_o + 2 \tag{2.37}$$

where L_o represents the number of low-frequency oscillators. Based on these assumptions, the normalized in-phase and quadrature parts of Jakes' channel model can be expressed as

$$h_R(t) = \frac{2}{\sqrt{L_{ch}}} \sum_{l=1}^{L_{ch}+1} a_l \cos(\omega_l t) \tag{2.38}$$

$$h_I(t) = \frac{2}{\sqrt{L_{ch}}} \sum_{l=1}^{L_{ch}+1} b_l \sin(\omega_l t) \tag{2.39}$$

where

$$a_l = \begin{cases} 2\cos(\beta_l), & l = 1, 2, \ldots, L_{ch}. \\ \sqrt{2}\cos(\beta_l), & l = L_{ch} + 1. \end{cases} \tag{2.40}$$

$$b_l = \begin{cases} 2\sin(\beta_l), & l = 1, 2, \ldots, L_{ch}. \\ \sqrt{2}\sin(\beta_l), & l = L_{ch} + 1. \end{cases} \tag{2.41}$$

$$\beta_l = \begin{cases} \frac{\pi l}{L_o+1}, & l = 1, 2, \ldots, L_{ch}. \\ \frac{\pi}{4}, & l = L_{ch} + 1. \end{cases} \tag{2.42}$$

$$\omega_l = \begin{cases} \omega_d \cos(\alpha_l), & l = 1, 2, \ldots, L_{ch}. \\ \omega_d, & l = L_{ch} + 1. \end{cases} \tag{2.43}$$

Jakes' channel model is employed for modelling the three LTE channel types this thesis.

2.4 Iterative Detection and Decoding Receivers

To meet the high data rate requirements of future applications, a combination of higher order modulation and efficient channel coding are essential in the design of wireless communication networks. As a result, bit interleaved coded modulation (BICM), first introduced in [82], has been standardized for current and future communication [83] systems. In BICM, a stream of bits are encoded by a channel encoder, interleaved and then modulated to obtain the transmit signal. In frequency selective channels, BICM systems achieve good bit-error-rate (BER) performance. However, the use of an interleaver can limits the performance of BICM, especially over additive white Gaussian noise (AWGN) channels. An effective solution to this problem is the application of iterative decoding (ID) at the receiver side. The resulting system is known as the BICM-ID [84–86]. By employing iterative decoding, the BICM receiver can achieve near optimum BER performance for both frequency selective and AWGN channels [87]. The description of BICM and BICM-ID systems are presented in the following subsections.

2.4.1 BICM

Transmitter

The BICM transmitter consist of an encoder, a bit interleaver, a serial-to-parallel (S/P) converter and a mapper as shown in Fig. 2.6. First, a stream of information bits, $\mathbf{b}$, is encoded by the channel encoder. Then, the sequence of encoded bits, $\mathbf{c}$, is passed through an interleaver. The bits at the interleaver output, $\mathbf{u}$, are grouped into blocks of length νN bits each, where ν and N are positive integers. Denote the t^{th} block of interleaved coded bits at the input of the mapper as $\mathbf{u}_t = [u_t^{(1)}, u_t^{(2)}, \ldots, u_t^{(\nu N)}]$. Finally, the mapper maps $\mathbf{u}_t$ to a vector of N consecutive 2^ν-ary transmit signals, $\mathbf{x}_t = [x_t^{(1)}, x_t^{(2)}, \ldots, x_t^{(N)}]$, using a mapping function $\lambda : \{0,1\}^{\nu N} \rightarrow \chi = \chi^N$, where χ denotes the 2^ν-ary signal constellation.

Receiver

At the receiver, the transmitter processing is reversed to recover the transmitted signal. The received signal corresponding to $\mathbf{x}_t$ can be represented as

$$\mathbf{y}_t = \mathbf{h}_t^T \mathbf{x}_t + \mathbf{z}_t \tag{2.44}$$

where $\mathbf{h}_t$ is the corresponding fading channel vector, $\mathbf{z}_t$ is the vector of AWGN with zero mean and variance N_0 and A^T represents the transpose of A. The demapper estimates the log-likelihood ratios

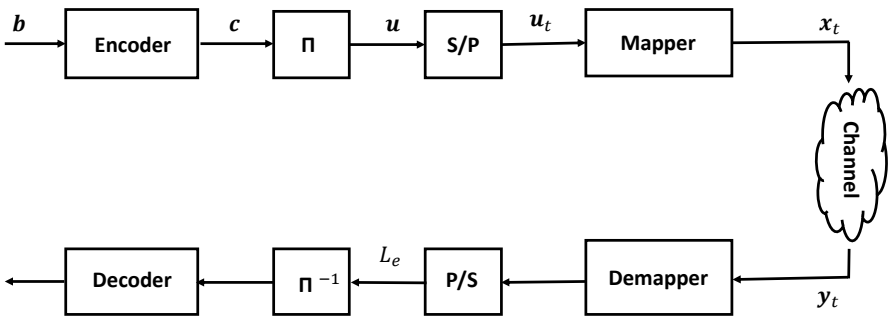

Fig. 2.6 Block diagram of BICM system

(LLRs) of the received signal as [85]

$$L_e(u_t^i) = \log \frac{\sum_{\mathbf{x}_t \in \chi_0^i} p(\mathbf{y}_t \mid \mathbf{x}_t)}{\sum_{\mathbf{x}_t \in \chi_1^i} p(\mathbf{y}_t \mid \mathbf{x}_t)} \tag{2.45}$$

where χ_0^i and χ_1^i represent the signals $\mathbf{x}_t \in \chi$ with 0 and 1, respectively, in the i^{th} bit position. $p(\mathbf{y}_t \mid \mathbf{x}_t)$ is the conditional PDF of the received signal, $\mathbf{y}_t$, given the transmit signal, $\mathbf{x}_t$. The LLR estimates of the demmaper is then deinterleaved and passed to the channel decoder. After decoding, a hard decision is made to obtain the transmitted signals.

2.4.2 BICM-ID

As mentioned above, the performance of BICM systems can be improved by employing iterative decoding at the receiver [84–86]. In BICM-ID systems the iterative decoding process is similar to the one used in turbo decoding [88]. However, BICM-ID systems employ a single decoder at the receiver side in order to reduce the decoding complexity in comparison with turbo decoding [85]. As shown in Fig. 2.7, the BICM-ID transmitter is the same as that of BICM. The difference between the two systems, however, is at the receiver side, in which the BICM-ID system has a feedback loop to return the decoder output as *a priori* LLR to the demapper. In multiple decoding iterations, the demapper uses the received signal vector $\mathbf{y}_t$ and the *a priori* LLR of the encoded bits to estimate the extrinsic LLRs of the bits in the received signal. The extrinsic LLR of the demapper during each iteration of the receiver can be expressed as

$$L_e(u_t^i) = \log \frac{\sum_{\mathbf{x}_t \in \chi_0^i} p(\mathbf{y}_t \mid \mathbf{x}_t) \prod_{j=1, j\neq i}^{\mu N} e^{-L_a(u_t^i)\cdot u_t^i}}{\sum_{\mathbf{x}_t \in \chi_1^i} p(\mathbf{y}_t \mid \mathbf{x}_t) \prod_{j=1, j\neq i}^{\mu N} e^{-L_a(u_t^i)\cdot u_t^i}} \tag{2.46}$$

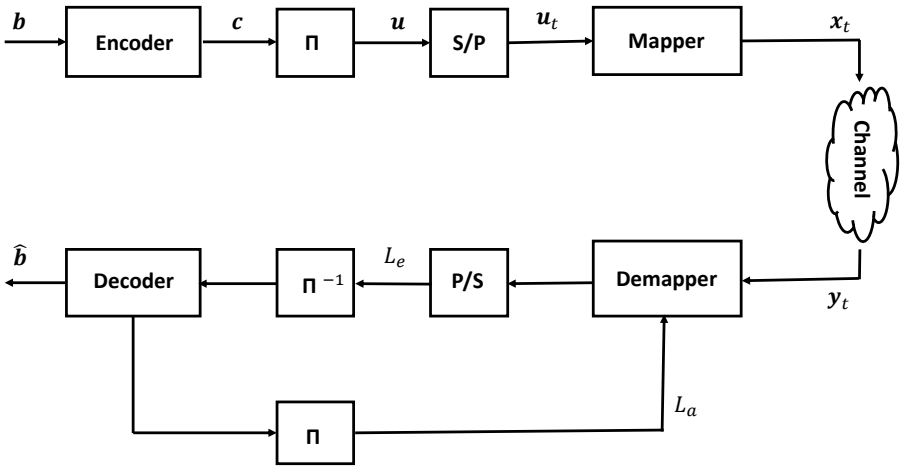

Fig. 2.7 Block diagram of BICM-ID system

where $L_a(u_t^i) = \log(p(u_t^i = 0)/p(u_t^i = 1))$ represents the *a priori* LLR of the encoded bits. After random deinterleaving, the extrinsic LLRs are passed to the channel decoder. The output of the channel decoder are then interleaved and fed back to the demapper as *a priori* LLR for the next decoding iteration. Through the iterative decoding process, the BICM-ID receiver can significantly improve the BER performance.

Note that the encoder and decoder blocks in Fig. 2.6 and Fig. 2.7 represent the forward error-correcting (FEC) code considered in the particular system under investigation. In LTE systems, turbo codes were adopted for data channels. However, to satisfy the new communication requirements of 5G NR, LDPC coding has replaced turbo coding for data channels. The advantages of LDPC codes compared to turbo codes include [89]:

- higher achievable peak throughput
- lower decoding complexity and improved decoding latency as a result of a higher degree of parallelism
- improved BER performance

Therefore, LDPC codes are adopted for the channel coding and decoding in this thesis. The detailed structure of LDPC codes is presented in the next subsection.

2.4.3 Channel Coding

LDPC Encoding

LDPC codes, first introduced in [90], are a class of linear block codes that uses a generator matrix for encoding and a parity-check matrix for decoding [91]. At the LDPC transmitter, a vector of information

bits $\mathbf{b} = [b_1, b_2, \ldots, b_{N_b}]$ are encoded by the generator matrix G to obtain the corresponding codeword $\mathbf{c}$ as

$$\mathbf{c} = \mathbf{b}G \tag{2.47}$$

Note that for a binary code with N_b information bits and a codeword of length N_c, G is a $N_b \times N_c$ binary matrix. The code rate is given as $r_c = N_b/N_c$. At the receiver side, a parity-check matrix, H_P of dimension $(N_c - N_b) \times N_c$, is used to perform the decoding process. The matrix H_P contains a very small number of non-zero elements. The sparsity of H_P ensures a decoding complexity which increases linearly with the code length. The original sparse parity-check matrices introduced in [90] were regular matrices, i.e. each column of H_P consist of a fixed number of non-zero elements, d_c, and each row of H_P consist of a fixed number of non-zero elements, d_r. To improve the decoding performance irregular parity-check matrices have been proposed for LDPC codes [92].

For irregular LDPC codes, the number of non-zero elements on each column or row varies, resulting in different column or row densities across the parity-check matrix. The fraction of columns of weight i (fraction of columns with i non-zero elements) is denoted as w_c^i and the fraction of rows of weight i denoted as w_r^i. Together the set of vectors $\mathbf{w}_c$ and $\mathbf{w}_r$ is referred to as the *degree distribution* of the LDPC code. An example of an irregular parity check matrix for a codeword of length $N_c = 6$ for an information bit stream of length $N_b = 3$ can be expressed as

$$H_P = \begin{bmatrix} 1 & 1 & 0 & 1 & 0 & 0 \\ 0 & 1 & 1 & 0 & 1 & 0 \\ 1 & 1 & 1 & 0 & 0 & 1 \end{bmatrix} \tag{2.48}$$

Each column of (2.48) corresponds to a bit in the codeword, whereas each row represents a parity-check equation or constraint. A codeword, $\mathbf{c}$, is a valid codeword if and only if it satisfy the constraint

$$H_P \mathbf{c}^T = 0 \tag{2.49}$$

For a code with parity-check matrix, H_P, the generator matrix can be obtained by applying a Gauss-Jordan elimination on H_P to decompose it to the form

$$H_P = [A, I_{N_c - N_b}] \tag{2.50}$$

where A is an $(N_c - N_b) \times N_b$ binary matrix and $I_{N_c - N_b}$ is the identity matrix of size $(N_c - N_b)$. The generator matrix can then be given as

$$G = [I_{N_b}, A^T] \tag{2.51}$$

Note that G and H_P are orthogonal to each other. Thus, if G is the generator matrix for an LDPC code with parity-check matrix H_P, then

$$G H_P^T = 0 \tag{2.52}$$

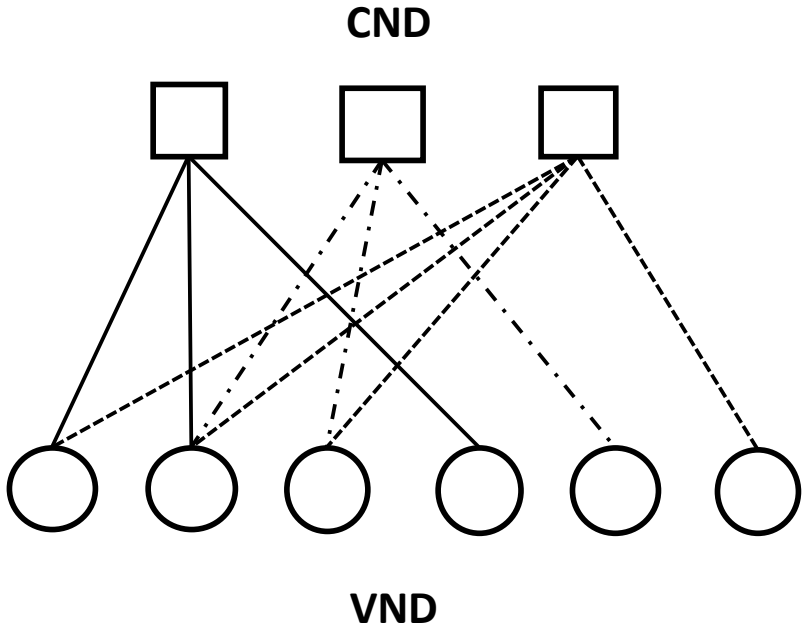

Fig. 2.8 Tanner graph representation of parity-check matrix in (2.50)

Apart from the matrix form, LDPC codes can be represented graphically in the form of a *Tanner graph* [93]. A Tanner graph consists of two sets of nodes: the check node decoder (CND) and the variable node decoder (VND). The number of CND nodes in the Tanner graph corresponds to the number of rows in the parity-check matrix. Also, the number VND nodes in the Tanner graph is the same as the number of columns in the corresponding parity-check matrix. An edge connects a VND node i to a CND node j on the Tanner graph, when the element in the i, j-th entry of the parity-check matrix is non-zero. Therefore, the number of edges in the Tanner graph is equal to the number of non-zero elements in the parity-check matrix. The Tanner graph representation for the parity-check matrix in (2.48) is illustrated in Fig. 2.8.

LDPC Decoding

The decoding performance of the LDPC code is determined by the type of decoding algorithm employed at the receiver side [94]. Collectively, the class of decoding algorithms used for decoding LDPC codes are referred to as *message-passing* algorithms. In some algorithms, such as *bit-flipping*, the messages exchanged between the two nodes are binary in nature. Other algorithms, such as *belief propagation*, are based on probabilities. The values of the probabilities represent the level of belief or confidence in the values of the decoded bits. For convenience and ease of implementation, the probability values in belief propagation can be represented as LLRs. This is referred to as *sum-*

product decoding [91]. In this work, the sum-product decoding algorithm is employed as the decoding algorithm at the LDPC decoder.

The sum-product decoding algorithm is a soft decision message passing algorithm which accepts the LLRs of each received bit as input. Because the LDPC decoder has prior knowledge of the input LLRs, the input LLRs are known as *a priori* LLRs. The LLRs output by the LDPC decoder is called the *a posteriori* LLRs. Overall, the aim of the sum-product decoding algorithm is to return the bit with the largest *a priori probability* (APP), i.e. $p_i = p(c_i = 1|N_p)$, which is the probability that the i-th codeword bit is 1 conditional on the event N_p that all parity-check constraints are satisfied. Thus, the sum-product decoder computes an approximation of the APP of the codeword bits in multiple iterations. The decoding steps for the sum-product algorithm is as follows:

- **Initialization**: Considering the BICM-ID system shown in Fig. 2.7, the initial input to the i-th VND, L^i, is the deinterleaved LLRs at the output of the demapper. The initial extrinsic LLR from the i-th VND to the j-th CND is $E_V^{i,j} = L_{in}^i$.

- **Check Node Update**: Each CND utilises the received extrinsic LLRs from the corresponding VNDs to compute its extrinsic LLRs. The extrinsic LLRs from the j-th CND to the i-th VND can be calculated as

$$E_C^{j,i} = 2\tanh^{-1}\left(\prod_{i' \in V_j, i' \neq i} \tanh\left(\frac{E_V^{i,j}}{2}\right)\right) \tag{2.53}$$

- **Variable Node Update**: Each VND uses the extrinsic LLRs from every connected CND to update its LLR, which in turn becomes the extrinsic LLR sent to the CNDs for the next decoder iteration. The updated extrinsic LLR from the i-th VND to the j-th CND is given as

$$E_V^{i,j} = L_{in}^i + \sum_{j' \in C_i, j' \neq j} E_C^{j',i} \tag{2.54}$$

- **Codeword Decision**: The decoding process terminates when the maximum number of iterations is reached or when doing more iterations will not improve the decoding performance. After the final iteration, the output LLRs of the sum-product algorithm can be calculated as the *a posteriori* LLRs:

$$L_{out}^i = L_{in}^i + \sum_{j' \in C_i} E_C^{j',i} \tag{2.55}$$

where V_j is the set of VNDs that exchanges bits with the j-th CND and C_i is the set of CNDs that exchange bits with the i-th VND.

2.4.4 EXIT Chart Analysis

The convergence behaviour of iterative decoders can be predicted by examining the exchange of mutual information (MI) between the component decoders in multiple iterations. This can be achieved

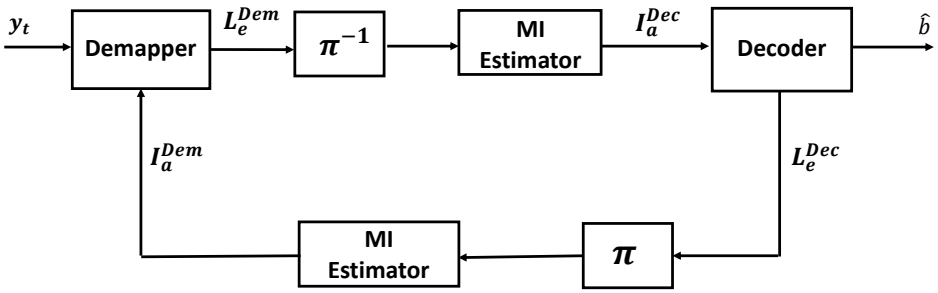

Fig. 2.9 Exchange of MI between demapper and decoder of BICM-ID

by employing EXIT charts, which was first introduced in [95]. An EXIT chart is a graphical semi-analytic technique that can be used to gain insight into the convergence properties of an iterative receiver without simulating the transmitter and receiver. In general, the EXIT chart technique is dependent on a Gaussian approximation of the received signal. As shown in Fig. 2.9, the Demapper takes the received signal from the channel and the *a priori* input from the Decoder, L_a^{Dem}, and generates soft output, L_e^{Dem}. The extrinsic soft information of the Demapper is passed through the bit de-interleaver to obtain the *a priori* information of the Decoder. After the Decoder processing, its extrinsic soft information, L_e^{Dec}, is interleaved and passed back to the Demapper as *a priori* input, L_a^{Dem}. In each iteration, the MI is used as a measure of the information between the transmitted bits and the soft information at the output of each component decoder. The MI estimator in Fig. 2.9 is evaluated assuming the Gaussian approximation and is given as follows:

Mutual Information

The MI between the transmitted bits and the LLR values at the output of a component decoder can be estimated by assuming a known probability distribution for the LLR values. The MI between equally likely information bits, x, and their corresponding LLR values, L, can be expressed as [96]

$$I(x,L) = \frac{1}{2}\sum_{x=\pm 1}\int_{-\infty}^{+\infty} p_L(\lambda|X=x)\times \log_2 \frac{p_L(\lambda|X=x)}{p_L(\lambda)} d\lambda \tag{2.56}$$

with

$$p_L(\lambda) = \frac{1}{2}\left[\, p_L(\lambda|X=-1) + p_L(\lambda|X=+1)\,\right] \tag{2.57}$$

where $p_L(\lambda|X=x)$ is the conditional PDF associated with L and X is a random variable (RV) representing the information bits. The LLR values, L, can be modelled by an independent Gaussian RV n_L with zero mean and variance σ_L^2 given by

$$L = \mu_L x + n_L \tag{2.58}$$

where $\mu_L = \sigma_L^2/2$ and σ_L^2 can be computed as [97]

$$\sigma_L^2 \approx \left(-\frac{1}{H_1} \log_2 \left(1 - I(x,L)^{1/H_3} \right) \right)^{1/2H_2} \tag{2.59}$$

with $H_1 = 0.3073$, $H_2 = 0.8935$ and $H_3 = 1.1064$. Following the Gaussian PDF, the MI expression in (2.56) can be rewritten as

$$I_L(\sigma_L) = 1 - \frac{1}{\sqrt{2\pi}\sigma_L} \int_{-\infty}^{+\infty} \exp\left(-\frac{\left(\lambda - \frac{\sigma_L^2}{2}\right)^2}{2\sigma_L^2} \right) \times \log_2 [\, 1 + \exp(-\lambda) \,] \, d\lambda . \tag{2.60}$$

Assuming a symmetric pdf for the LLR values, i.e. $p_L(-\lambda | X = +1) = p_L(\lambda | X = -1)$, a simple approximation of the MI expression in (2.60) is given by

$$I(x,L) = 1 - \mathbb{E}\{\log_2 [\, 1 + \exp(-\lambda) \,]\} \tag{2.61}$$

where $\mathbb{E}$ represents the expectation operation. According to [96], by replacing the ensemble average in (2.61) by the time average, the MI can be measured for a sufficiently large number of samples, T_s, even for non-Gaussian or undefined distributions. The approximated MI expression using time averaging is given as

$$I(x,L) = 1 - \frac{1}{T_s} \sum_{t=1}^{T_s} \log_2 [\, 1 + \exp(-x_t \cdot L_t) \,] \tag{2.62}$$

where L_t is the LLR value associated with the bits $x_t \in \{-1, +1\}$.

As can been seen from Fig. 2.9, the extrinsic MI of the Demapper is a function of the *a priori* MI received from the Decoder and the received signal coming from the channel. Therefore, the extrinsic MI of the Demapper, I_e^{Dem}, is defined by the transfer function

$$I_e^{Dem} = \mathbb{T}[\, I_a^{Dem}, \sigma_n^2 \,] \tag{2.63}$$

where σ_n^2 is the channel noise variance or channel SNR value and both I_a^{Dem} and I_e^{Dem} can be obtained using (2.62). However, the Decoder has only the *a priori* information, I_a^{Dec}, as input and its extrinsic MI, I_e^{Dec}, is defined by the transfer

$$I_e^{Dec} = \mathbb{T}[\, I_a^{Dec} \,] \tag{2.64}$$

Similarly, both I_a^{Dec} and I_a^{Dec} can be obtained using (2.62).

The EXIT chart is made up of two curves for the two components of the iterative receiver, i.e. the Demapper and Decoder in the example shown in Fig. 2.9. Each curve on the EXIT chart is a plot of the MI of the extrinsic LLRs against the MI of the *a priori* LLRs of the respective component. This is a measure of the quality of information at the output of the component receiver compared to its input. Using the *a priori* and extrinsic MI of the Demapper and Decoder, the EXIT chart can be plotted

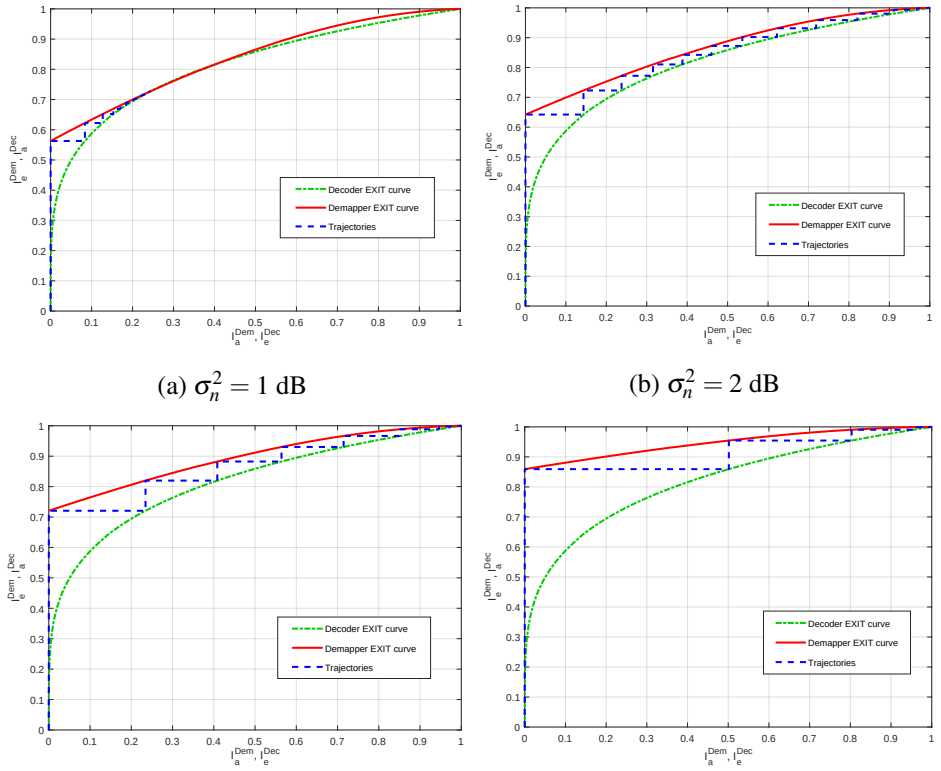

(a) $\sigma_n^2 = 1$ dB (b) $\sigma_n^2 = 2$ dB

(c) $\sigma_n^2 = 3$ dB (d) $\sigma_n^2 = 5$ dB

Fig. 2.10 EXIT curves of BICM-ID for different values of SNR

as shown in Fig. 2.10 and the trajectories between the two component decoders can be tracked. In Fig. 2.10 the EXIT chart is plotted for a BICM-ID receiver over the AWGN channel. The red (solid) line represents the extrinsic MI coming out of the Demapper versus the *a priori* MI going into the Demapper. Also, the green (dashed-dot) line depicts the *a priori* MI going into the Decoder against the extrinsic MI coming out of the Decoder. The blue (dashed) lines represents the trajectories or number of iterations required for the BICM-ID receiver to achieve convergence. For the receiver to converge, there should be an open area or "tunnel" between the red and green lines. As shown in Fig. 2.10 (a), at a low SNR value of 1 dB the two lines coincide around $I_e^{Dem} = 0.2$. In this case the tunnel between the two lines is blocked and the two lines cannot meet at the $(I_e^{Dec}, I_e^{Dem}) = (1,1)$ point on the graph. The receiver therefore achieves a poor error rate performance. However, since the Demapper EXIT curve depends on the SNR of the received signal, increasing the SNR to 2 dB moves the red curve upwards and a tunnel opens between the two EXIT curves, as shown in Fig. 2.10 (b). Moreover, with the open tunnel the two curves converge at the $(I_e^{Dec}, I_e^{Dem}) = (1,1)$ point after about 14 iterations. Furthermore, as can be seen in Fig. 2.10 (c) and Fig. 2.10 (d), the wider the tunnel between the two curves, the lower the number of iterations needed to reach the $(I_e^{Dec}, I_e^{Dem}) = (1,1)$ point on the EXIT curve. At SNR of 3 dB and 5 dB, around 9 and 5 iterations, respectively, are required for optimum performance. Thus, the EXIT chart gives an indication of the trade-off between SNR and number of

iterations needed for effective decoding. In Chapter 4, EXIT chart analysis will be used to evaluate the convergence and complexity of the IIC-based BICM-ID receiver for FBMC-QAM.

2.5 Energy Harvesting Systems

In future wireless communication applications, such as mMTC, achieving reliable communication while maintaining prolonged device lifespan is a key requirement. For energy constrained network devices, harvesting energy from the environment is a viable option to extend their operational lifespan. Traditionally, energy can be harvested from sources such as solar power, wind power, thermal power and vibrations [98, 99]. However, these sources are usually unstable and are affected by environmental factors like the changing weather pattern [21]. Another source of EH that is more stable and reliable is the RF signal. RF EH is considered in this work, details of which are presented in the next subsection.

2.5.1 RF Energy Harvesting

The process of transmitting RF signals for the purposes of EH is referred to as WPT. Practically, WPT can be implemented using two main techniques; wireless powered communication networks (WPCN) and SWIPT as shown in Fig. 2.11. In WPCN, energy transmitters send energy signals to UNs in the DL only for EH [100, 101]. The harvested energy is used to power the transmission of the UN in the UL. As the name suggests, SWIPT systems on the other hand, involves the concurrent transmission of information and energy to a UN. Moreover, the UN has the capability of performing both ID and EH using the same received signal.

Two main receiver configurations have been studied in the literature for SWIPT systems as shown in Fig. 2.12 [102]. First is the *separate receiver architecture*, in which the information and energy receivers have separate antennas. This implies that both ID and EH can take place at the same time using the entire received signal on each antenna. A typical application of the separate receiver architecture is a scenario where different devices serve as energy and information receivers. In this case, the energy receiver can be a low-power device that harvest energy from the received signal, whereas the information receiver can be a low data rate device receiving data. The second configuration is the *co-located receiver architecture*. In this case there are separate information and energy receivers that share the same antenna. Under this architecture, the received signal is processed by one of two schemes: TS, or PS [24, 25, 103]. In the case of TS, the time slot for decoding the received signal is divided into two subslots. EH is performed in the first subslot, while ID is performed in the second subslot [104, 105]. The PS case, on the other hand, divides the received signal power into two portions using a PS ratio, with one portion of the signal used for EH and the other portion for ID. For the co-located receiver architecture, a practical application will be the scenario where each receiver is a single low power device that simultaneously harvesting energy and receiving information.

Recently, SWIPT has been investigated for different wireless applications and deployment scenarios. The work in [106] proposed a multihop decode-and-forward (DF) SWIPT system where a

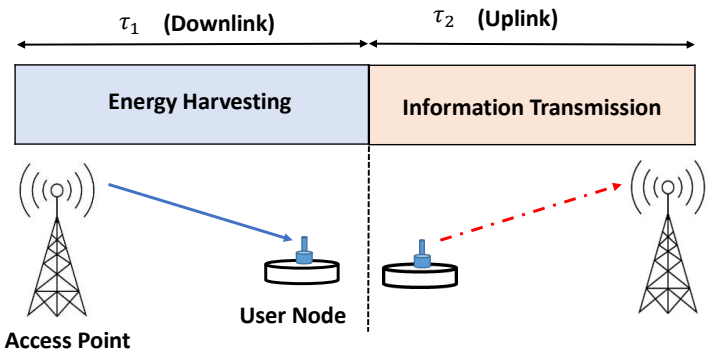

(a) WPCN

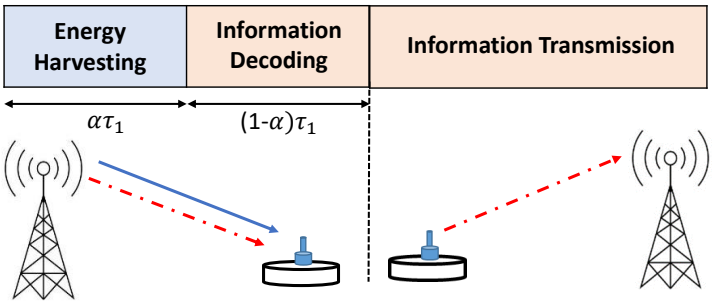

(b) TS-based SWIPT

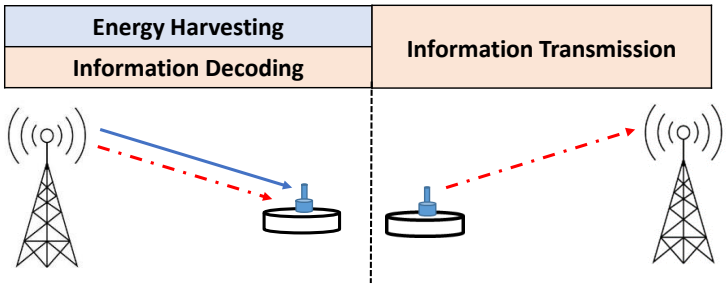

(c) PS-based SWIPT

Fig. 2.11 WPT models

source transmits information to a destination via a set of multihop PS-based SWIPT relays. The relays harvest energy from the received signal to aid the forwarding of the transmitted data to the destination node. A SWIPT system for IoT sensor networks is studied in [107] in which a number of transmitter-receiver pairs exchange information and energy by employing PS at the receiver node. In [108], a TS-based SWIPT system is considered for a multiple-input-multiple-output broadcast channel (MIMO-BC). A stochastic optimal control algorithm for the wireless powered communication networks with energy beamforming is proposed in [109]. The energy beamforming is used to enhance the RF energy transfer efficiency by focusing the radiated power on target nodes. As validation of the

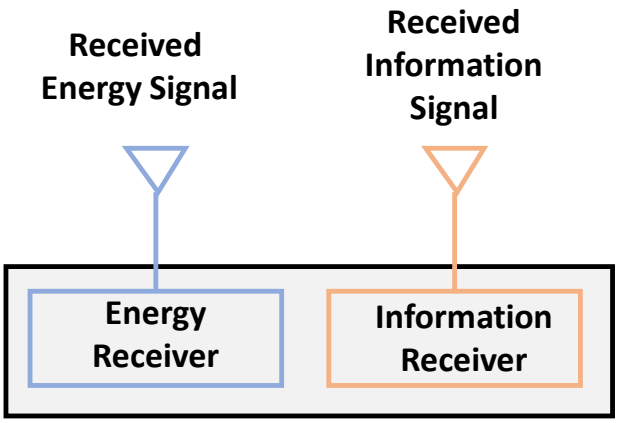

(a) Separate Receiver Configuration

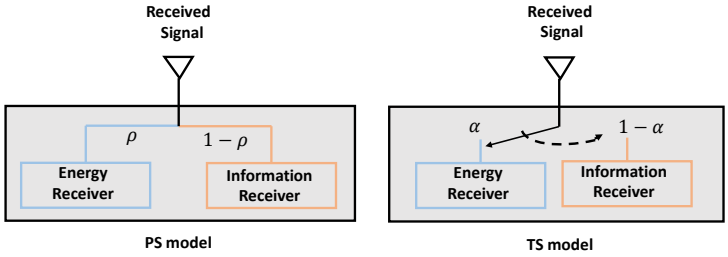

(b) Co-located Receiver Configuration

Fig. 2.12 SWIPT antenna configurations

theoretical model in [109], the same authors implemented a real-life EH testbed in [110] and [111]. Further research has been done for the implementation of SWIPT in different systems, e.g. MIMO [112–114], relay networks [21, 106, 115] and interference channels [116–118].

In addition to the applications mentioned above, SWIPT has been investigated for multicarrier waveforms [119–121]. In [120], a multi-user OFDM-based SWIPT system is investigated, in which a number of distributed nodes receive signals from an access point (AP) for their ID and EH. For practical implementation, two multiple access and EH schemes are considered in [120]: (i) TDMA transmission with TS at the receiver and (ii) OFDMA transmission with PS at the receiver. The work in [121] proposed a SWIPT-based OFDM system in which the received OFDM signal is divided into two groups of subcarriers: one group for ID and the other group for EH. The authors focus on solving a joint subcarrier and power allocation problem to maximize the harvested energy at the receiver node, while guaranteeing a target transmission rate.

Recall from Subsection 2.2.6 above that the drawbacks of OFDM make it inefficient in satisfying the diverse requirements of future wireless networks, especially mMTC applications. Thus, the application of SWIPT to non-orthogonal waveforms has been investigated recently [122–124]. In

[122], a GFDM-based cooperative relay system is proposed to improve the quality of experience and extend battery life of users at the edge of a cell. The same authors proposed a joint resource allocation for a multi-user SWIPT GFDM system in [123]. Specifically, a sum rate maximization problem is investigated in order to optimize sub-block allocation, power allocation and PS ratio under a total transmit power and EH constraints. The DF SWIPT model in [122] is extended to a GFDM-based amplify-and-forward (AF) system in [124]. In [124], an analytical expression for the BER is derived for a general QAM constellation set.

In the above referenced works, the EH model is based on the linear model of a rectifier circuit, i.e. the harvested energy is linearly dependent on the received RF signal. Following the linear EH model, the harvested energy from the received signal can be written as

$$Q = \beta \mathbb{E}[|y(t)|^2] \tag{2.65}$$

where Q represents the amount of energy harvested, β is the energy conversion efficiency and $y(t)$ is the received RF signal. However, the linear EH model is not practical as it does not capture the non-linear behaviour of the diodes, inductors and capacitors that make up the rectifier circuit. Therefore, non-linear EH models that take into account the rectifier non-linearity are introduced in [125]. The analytical models of non-linear EH discussed in [125] take into account the higher order terms in the Taylor series expansion of the diode characteristics. By considering higher order Taylor series expansions, the non-linear EH models in [125] results in more complex EH receivers. To reduce processing complexity, a simplified piece-wise linear EH model that captures the saturation characteristics of a practical rectifier circuit is proposed in [126], as an improvement of conventional linear EH model. The simplified non-linear EH model in [126] behaves as the linear EH model until the harvested power reaches a power threshold Q_{th}. Afterwards, the energy harvester will output a constant power denoted as βQ_{th}, i.e.

$$Q = \begin{cases} \beta \mathbb{E}[|y(t)|^2], & \text{for } \mathbb{E}[|y(t)|^2] \leq Q_{th} \\ \beta Q_{th}, & \mathbb{E}[|y(t)|^2] > Q_{th} \end{cases} \tag{2.66}$$

where Q_{th} is the saturation threshold power of the EH receiver.

In order to harness the benefits of both SWIPT and non-orthogonal waveforms for future applications, this thesis investigates the application of a non-linear SWIPT model in FBMC-QAM systems. The simplified non-linear EH model given in (2.66) is adopted in this thesis for the sake of analytical tractability.

2.6 Summary

In this chapter, an overview of the fundamental concepts relevant to this thesis has been presented. First, a review of 5G NR outlining the various numerologies is provided. Then, the basic concepts

of some waveform candidates for future wireless networks are presented. In addition, the basics of statistical channel models, including standard LTE channel models are introduced. Furthermore, an overview of iterative detection and decoding using LDPC coding is provided. Finally, the underlying concepts of RF EH systems have been presented. In the following chapter, the first major contribution of this thesis is presented.

Chapter 3

Iterative Interference Cancellation in Uncoded FBMC-QAM Systems

3.1 Introduction

In FBMC-QAM systems there is a complete loss of orthogonality between symbols and subcarriers resulting in intrinsic interference which degrades its performance compared to conventional OFDM. However, FBMC-QAM systems have advantages for future applications, e.g. mMTC, due to its high spectral efficiency and suitability for asynchronous transmissions. Therefore, efficient receiver design to address the intrinsic interference problem in FBMC-QAM systems is needed before FBMC-QAM can be employed in future wireless networks. Recently, a number of receiver architectures have been considered to address this problem. In [19], the authors proposed a twin-filter model for even and odd-numbered subcarriers that together satisfy complex orthogonality in ideal channels. However, in fading channels, residual interference remains. Also, the filter design causes filter coefficient discontinuities which result in higher OOB emissions compared to OFDM. FMBC-QAM systems with optimized filter sets have been proposed to find a trade-off between satisfying orthogonality and maintaining good frequency localization [127, 128]. In [128], improvements in BER and OOB emission performance is achieved at the expense of highly complex channel equalizer compared to OFDM. A linearly processed FBMC-QAM system was proposed in [129] which achieves similar OOB emission as FBMC-OQAM by transmitting data only on even-numbered subcarriers, therefore making use of only half of the assigned frequency band.

The purpose of this chapter is to show that the intrinsic interference in FBMC-QAM can be effectively removed by employing an IIC receiver. Thus, FBMC-QAM becomes a promising alternative to OFDM systems in applications that require asynchronous access between network nodes. This chapter investigates the performance of an uncoded FBMC-QAM system with a single prototype filter under different fading channels. The proposed IIC receiver separates the received FBMC-QAM signal into even- and odd-numbered subcarrier components and use the demodulated even- and odd-numbered

subcarrier symbols to iteratively remove the intrinsic interference. As shown in [129], due to the high frequency localization in FBMC systems, data symbols on even-numbered (odd-numbered) subcarriers cause negligible interference to other even-numbered (odd-numbered) subcarrier symbols. Therefore, by applying separate processing to the even and odd subcarriers the ICI between adjacent subcarriers can be reduced.

The rest of this chapter is organized as follows: Section 3.2 describes the FBMC-QAM system model. Section 3.3 outlines the IIC algorithm for FBMC-QAM. Simulation results are presented in Section 3.4. Finally, a summary of this chapter is presented in Section 3.5.

3.2 System Model

In this chapter, an IIC receiver is proposed to iteratively cancel the ISI and ICI inherent in FBMC-QAM systems. The approach is to separate the received signal into even- and odd-numbered subcarrier components and use the demodulated even- and odd-numbered subcarrier symbols to iteratively remove the effect of interference. As mentioned above, this approach is adopted to take advantage of the high frequency localization of FBMC-based prototype filters. At the FBMC-QAM transmitter, the QAM modulated symbols are separated into even- and odd-numbered subcarrier components. Each set of symbols then goes through the FBMC modulation process, which consist of IFFT and SFB operations, as shown in Fig. 3.1. Similar to the derivation in subsection 2.2.5, the output of the $M/2$-IFFT of the data at the m-th even-numbered subcarrier of the n-th symbol is given as

$$b_{m,n}^{even} = \sum_{m=0}^{M/2-1} a_{m,n}^{even} e^{j\frac{2\pi}{M/2}mn} \tag{3.1}$$

where $a_{m,n}^{even} = a_{2m,n}^{even}$ $m \in \{0,1,\ldots M/2\}$ represents the n-th even-numbered subcarrier symbol, and M is the total number of subcarriers. The vector form of the n-th even-numbered subcarrier symbol for $m \in \{0,1,\ldots M/2\}$ is expressed as

$$\mathbf{b}_n^{even} = \Phi \mathbf{a}_n^{even} \tag{3.2}$$

where $\mathbf{b}_n^{even} \triangleq [b_{0,n}^{even}, \ldots, b_{M/2-1,n}^{even}]$, $\mathbf{a}_n^{even} \triangleq [a_{0,n}^{even}, \ldots, a_{M/2-1,n}^{even}]$ and Φ is the $M/2$ IDFT matrix whose entry on the i-th row and j-th column is $e^{j\frac{2\pi ij}{M/2}}$. Similarly, the vector form of $M/2$-IFFT of the n-th odd-numbered subcarrier symbol is given as

$$\mathbf{b}_n^{odd} = \Phi \mathbf{a}_n^{odd} \tag{3.3}$$

where $\mathbf{b}_n^{odd} \triangleq [b_{0,n}^{odd}, \ldots, b_{M/2-1,n}^{odd}]$ and $\mathbf{a}_n^{odd} \triangleq [a_{0,n}^{odd}, \ldots, a_{M/2-1,n}^{odd}]$.

The IFFT output is oversampled by an overlapping factor D and filtered by the SFB. An efficient and low complexity implementation of the per-subcarrier filtering in FBMC is the PPN [129], which is employed in this thesis. The signal on the m-th even-numbered subcarrier of the n-th symbol after

SFB processing is given as

$$x_{m,n}^{even} = \sum_{k=0}^{2D-1} g[kM/2] b_{m,n-k}^{even} \tag{3.4}$$

where $g[i]$ is the prototype filter impulse response. The most popular prototype filter adopted in FBMC systems is the PHYDYAS prototype filter. This is due to its low OOB emission performance compared to other prototype filters. Also, it was shown in [14] that the PHYDYAS prototype filter is effective for interference cancellation receivers. Therefore, the PHYDYAS prototype filter is employed in this thesis. In vector form, the transmit signal of the n-th even-numbered subcarrier symbol can be expressed as

$$\begin{aligned} \mathbf{x}_n^{even} &= \mathbf{G}_n \mathbf{b}_n^{even} \\ &= \mathbf{G}_n \Phi \mathbf{a}_n^{even} \end{aligned} \tag{3.5}$$

where $\mathbf{x}_n^{even} \triangleq [x_{0,n}^{even}, \ldots, x_{M/2-1,n}^{even}]$ and $\mathbf{G}_n$ is the PPN matrix whose i-th row and j-th column is given as [129]

$$[\mathbf{G}_n]_{ij} = \begin{cases} g[(i-j)M/2], & \text{for } 0 \leq i-j < 2D \\ 0, & \text{otherwise} \end{cases} \tag{3.6}$$

Unlike [19], which uses two different prototype filters for even and odd-numbered subcarriers, the same prototype filter is employed for both even and odd-numbered subcarriers in this thesis. This is because the dual filters employed in [19] results in high leakage interference between adjacent frequency bands. As discussed in Chapter 2, for future applications that may require asynchronous transmissions between network nodes, a system with high OOB emission may not be suitable. Moreover, it will be shown in Chapter 4 that FBMC-QAM with a single prototype filter on all subcarriers achieve a better OOB emission performance compared to FBMC-QAM with optimized dual filters. Similar to (3.5), the vector form of the n-th odd-numbered subcarrier symbol after transmit filter processing can be expressed as

$$\begin{aligned} \mathbf{x}_n^{odd} &= \mathbf{G}_n \mathbf{b}_n^{odd} \\ &= \mathbf{G}_n \Phi \mathbf{a}_n^{odd} \end{aligned} \tag{3.7}$$

Combining the even and odd-numbered subcarriers, the overall discrete-time transmit signal during the n-th time slot is given by

$$\begin{aligned} \mathbf{x}_n &= \mathbf{x}_n^{even} + \mathbf{x}_n^{odd} \\ &= \mathbf{G}_n \Phi \mathbf{a}_n^{even} + \mathbf{G}_n \Phi \mathbf{a}_n^{odd} \end{aligned} \tag{3.8}$$

After passing through the multipath frequency selective channel, the received FBMC-QAM signal vector corresponding to the n-th symbol is given as

$$\mathbf{y}_n = \mathbf{H}\mathbf{x}_n + \mathbf{z}_n \tag{3.9}$$

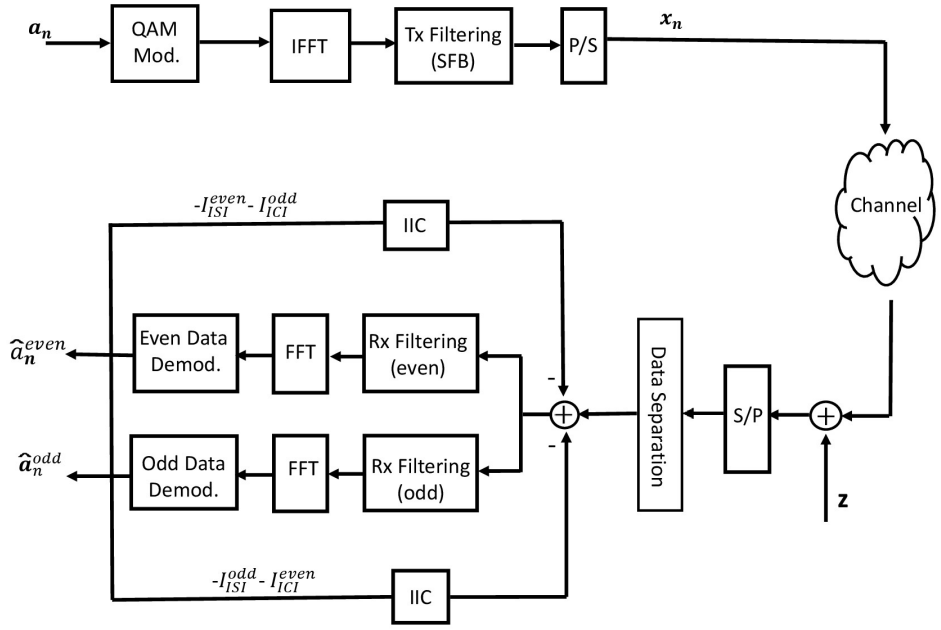

Fig. 3.1 Proposed FBMC-QAM IIC Transceiver

where $\mathbf{H}$ denotes the multipath channel matrix with entries given as

$$[\mathbf{H}]_{\tau_1,\tau_2} = \begin{cases} h(\tau_1 - \tau_2), & \text{for } 0 \leq \tau_1 - \tau_2 < L_{ch}, \\ 0, & \text{otherwise} \end{cases} \tag{3.10}$$

$h(\tau)$ is the time-domain multipath channel impulse response, τ is the multipath delay, L_{ch} is the length of the channel and $\mathbf{z}_n$ is the AWGN vector.

The received signal is then processed by the proposed receiver, which consist of FBMC-QAM demodulation and IIC processing. First, the received signal is passed to the FBMC-QAM demodulator, which is made up of an AFB and an FFT operation. For ideal performance, the AFB is chosen to satisfy the PR condition, as discussed in Chapter 2. However, in frequency-selective channels, it is impossible to achieve PR condition. Thus, prototype filters are designed to satisfy the NPR characteristics. To achieve at least NPR, the receiver filter is designed to be the complex conjugate and time reversed version of the transmit filter [51]. NPR processing is employed in this thesis. Therefore, the n-th symbol vector after AFB processing is given by

$$\begin{aligned} \hat{\mathbf{y}}_n &= \mathbf{G}_n^H \mathbf{y}_n \\ &= \hat{\mathbf{y}}_n^{even} + \hat{\mathbf{y}}_n^{odd} \end{aligned} \tag{3.11}$$

where $\hat{\mathbf{y}}_n^{even} \triangleq [\hat{y}_{0,n}^{even}, \ldots, \hat{y}_{M/2-1,n}^{even}]$ and $\hat{\mathbf{y}}_n^{odd} \triangleq [\hat{y}_{0,n}^{odd}, \ldots, \hat{y}_{M/2-1,n}^{odd}]$ are the sampled even and odd-numbered subcarriers of the filtered signal. Then, down-sampling followed by FFT is performed on

the filtered signal to obtain the frequency domain signal vector. The output of the $M/2$-FFT can be expressed as

$$\begin{aligned}\hat{\mathbf{b}}_n &= \hat{\mathbf{y}}_n \Phi^H \\ &= \hat{\mathbf{y}}_n^{even} \Phi^H + \hat{\mathbf{y}}_n^{odd} \Phi^H \\ &= \mathbf{H}\mathbf{G}_n^H \mathbf{G}_n \Phi^H \Phi \mathbf{a}_n^{even} + \mathbf{H}\mathbf{G}_n^H \mathbf{G}_n \Phi^H \Phi \mathbf{a}_n^{odd} + \mathbf{G}_n^H \Phi^H \mathbf{z}_n \\ &= \mathbf{H}\mathbf{Q}\mathbf{a}_n^{even} + \mathbf{H}\mathbf{Q}\mathbf{a}_n^{odd} + \tilde{\mathbf{z}} \\ &= \hat{\mathbf{b}}_n^{even} + \hat{\mathbf{b}}_n^{odd} + \tilde{\mathbf{z}}\end{aligned} \tag{3.12}$$

where $\hat{\mathbf{b}}_n^{even} \triangleq [\hat{b}_{0,n}^{even}, \ldots, \hat{b}_{M/2-1,n}^{even}]$, $\hat{\mathbf{b}}_n^{odd} \triangleq [\hat{b}_{0,n}^{odd}, \ldots, \hat{b}_{M/2-1,n}^{odd}]$, $\mathbf{Q} = \mathbf{G}_n^H \mathbf{G}_n \Phi^H \Phi$ and $\tilde{\mathbf{z}} = \mathbf{G}_n^H \Phi^H \mathbf{z}_n$. After the FBMC-QAM demodulation, the demodulated signal of the n-th even-numbered subcarrier symbol is given as

$$\hat{\mathbf{a}}_n^{even} = \mathbf{H}_D \mathbf{a}_n^{even} + \underbrace{\mathbf{H}_{ISI}(\mathbf{Q}-\mathbf{I})\mathbf{a}_{n-1}^{even}}_{I_{ISI}^{even}} + \underbrace{\mathbf{H}_{ICI}\mathbf{Q}\mathbf{a}_n^{odd}}_{I_{ICI}^{odd}} + \tilde{\mathbf{z}} \tag{3.13}$$

where I_{ISI}^{even} and I_{ICI}^{odd} represent the ISI and ICI experienced by even-numbered subcarrier symbols. Similarly, the demodulated signal of the n-th odd-numbered subcarrier symbol can be expressed as

$$\hat{\mathbf{a}}_n^{odd} = \mathbf{H}_D \mathbf{a}_n^{odd} + \underbrace{\mathbf{H}_{ISI}(\mathbf{Q}-\mathbf{I})\mathbf{a}_{n-1}^{odd}}_{I_{ISI}^{odd}} + \underbrace{\mathbf{H}_{ICI}\mathbf{Q}\mathbf{a}_n^{even}}_{I_{ICI}^{even}} + \tilde{\mathbf{z}} \tag{3.14}$$

where I_{ISI}^{odd} and I_{ICI}^{even} are the ISI and ICI experienced by odd-numbered sub-carrier symbols. Also, $\mathbf{H}_D$, $\mathbf{H}_{ICI}$, and $\mathbf{H}_{ISI}$ correspond respectively to the desired channel, the undesired channel that result in ICI and the channel that lead to ISI, and $\mathbf{I}$ is the identity matrix. Since FBMC systems use no CP, the interference channel matrix $\mathbf{H}_{ICI} = \mathbf{H}_{ISI} = \mathbf{H}_j \in \mathbb{C}^{N \times N}$ and can be expressed as

$$\mathbf{H}_j = \begin{bmatrix} 0_{E\times(N-E)} & \mathbf{H}_1 \\ 0_{(N-E)\times(N-E)} & 0_{(N-E)\times E} \end{bmatrix} \tag{3.15}$$

where $\mathbf{H}_1 \in \mathbb{C}^{E\times E}$, with $E = L-1$, is given by

$$\mathbf{H}_1 = \begin{bmatrix} h_{L-1} & \ldots & \ldots & h_0 \\ 0 & \ddots & & \vdots \\ \vdots & \ddots & \ddots & \vdots \\ 0 & \ldots & 0 & h_{L-1} \end{bmatrix} \tag{3.16}$$

As an illustration of the interference terms, consider the i-th transmitted multicarrier symbol of a system with $M = 4$ subcarriers, i.e. $\mathbf{x}^i = [x_0^i \; x_1^i \; x_2^i \; x_3^i]$ and a channel impulse response with length $L_{ch} = 4$, i.e. $\mathbf{h}^i = [h_0 \; h_1 \; h_2 \; h_3]$. The linear convolution between $\mathbf{x}^i$ and $\mathbf{h}^i$ for a muticarrier system with sufficient CP (e.g. OFDM) is shown in Fig. 3.2. The CP is obtained by copying a number of

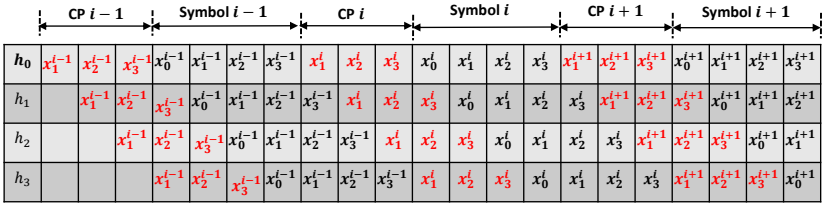

(a) Received signal with CP

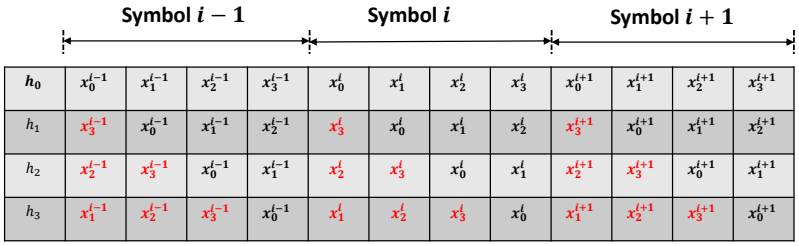

(b) Signal after removing CP

Fig. 3.2 Effect of frequency-selective channel on received multicarrier symbols with sufficient CP

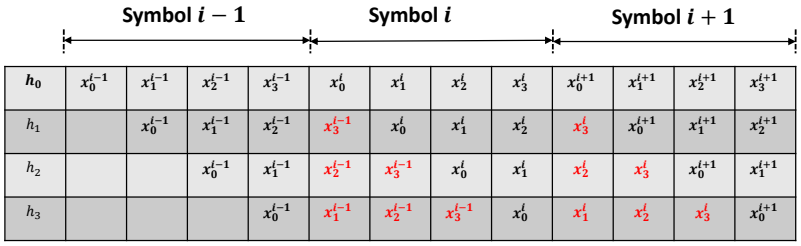

Fig. 3.3 Effect of frequency-selective channel on received multicarrier symbols with no CP

samples at the tail of each symbol and appending it at the beginning of the symbol. As shown in Fig. 3.2 (a), the multipath channel causes an overlap of the different multicarrier symbols at the receiver side. However, with sufficient CP the symbol overlap occurs within the allocated CP. Therefore, after removing CP, the orthogonality between symbols is maintained as shown in Fig. 3.2 (b). Thus, with a sufficient CP length intrinsic interference can be avoided.

In the case of a muticarrier system with no CP (e.g. FBMC), the symbol overlap occur within the symbols themselves as shown in Fig. 3.3. Taking the symbol i as an example, it can be seen that samples from symbol $i-1$ overlap with symbol i. Due to the lack of CP, this overlap cannot be compensated for and the orthogonality between symbols is lost. This means that intrinsic interference will occur at the receiver node. For desirable performance, the intrinsic interference terms must be estimated and cancelled from the received signal. This chapter shows that by applying IIC at the

receiver node, the interference terms in (3.13) and (3.14) can be cancelled, making FBMC-QAM a suitable waveform for future applications due to its high spectral efficiency and suitability to asynchronous transmissions. To effectively cancel the interference terms, the interference channels I_{ISI}^{even} and I_{ICI}^{odd} must be estimated at the receiver. Note that, without loss of generality, it is assumed in this thesis that the receiver node has perfect channel state information (CSI).

3.3 Iterative Interference Cancellation in FBMC-QAM

Due to the loss of complex orthogonality in FBMC-QAM, there is high intrinsic interference as shown in (3.13) and (3.14). To reduce the level of intrinsic interference and improve the BER performance, the undesirable terms must be removed from (3.13) and (3.14). In this chapter, an IIC receiver is investigated to remove the interference terms [130]. First, the receiver estimates the multipath channel responses $\mathbf{H}_{ICI}$, and $\mathbf{H}_{ISI}$. Then the matrix $\mathbf{Q}$ is computed using the filter response matrix $\mathbf{G}_n$ and IDFT matrix Φ. Next, using the current and previous values of the demodulated even- and odd-numbered subcarrier symbols, the receiver can evaluate I_{ISI}^{even}, I_{ICI}^{odd}, I_{ISI}^{odd} and I_{ICI}^{even} as shown in (3.13) and (3.14). Then, the calculated interference terms from the even- and odd-numbered data symbols are subtracted from the received signal vector in order to achieve a better version of the transmitted signal in the next iteration, i.e.

$$\hat{\mathbf{a}}_n^{even}(i+1) = \hat{\mathbf{a}}_n^{even}(i) - I_{ISI}^{even}(i) - I_{ICI}^{odd}(i) \tag{3.17}$$

and

$$\hat{\mathbf{a}}_n^{odd}(i+1) = \hat{\mathbf{a}}_n^{odd}(i) - I_{ISI}^{even}(i) - I_{ICI}^{even}(i) \tag{3.18}$$

where $i \leq I_{max}$ and I_{max} is the maximum number of iterations. After a number of iterations the ICI and ISI are removed and the resulting even- and odd-numbered demodulated signal can be expressed as

$$\hat{\mathbf{a}}_n^{even} = \mathbf{H}_D \mathbf{a}_n^{even} + \tilde{\mathbf{z}} \tag{3.19}$$

and

$$\hat{\mathbf{a}}_n^{odd} = \mathbf{H}_D \mathbf{a}_n^{odd} + \tilde{\mathbf{z}}, \tag{3.20}$$

respectively. Finally, a hard decision is made on the demodulated signal and this provides the final estimate of the transmitted information bits. The pseudo code for the proposed IIC receiver is presented in Algorithm 1. In Chapter 5, the intrinsic interference in FBMC-QAM systems will be exploited as a useful signal for RF EH to provide power for energy constrained communication devices. This chapter mainly focuses on the information decoding performance by eliminating the unwanted intrinsic interference terms.

Algorithm 1 IIC Algorithm

Specify the maximum number of iterations I_{max}
Initialize number of iterations $i = 0$
while $i \leq I_{max}$ **do**
  Compute $\mathbf{H}_{ICI}$ and $\mathbf{H}_{ISI}$ from (3.15).
  Compute $\mathbf{Q}$ using $\mathbf{G}_n$ and Φ.
  Estimate I_{ISI}^{even}, I_{ICI}^{odd}, I_{ISI}^{odd} and I_{ICI}^{even} in (3.13) and (3.14)
  Perform Interference cancellation, i.e
  $\hat{\mathbf{a}}_n^{even}(i+1) = \hat{\mathbf{a}}_n^{even}(i) - \hat{I}_{ISI}^{even}(i) - \hat{I}_{ICI}^{odd}(i)$
  $\hat{\mathbf{a}}_n^{odd}(i+1) = \hat{\mathbf{a}}_n^{odd}(i) - \hat{I}_{ISI}^{odd}(i) - \hat{I}_{ICI}^{even}(i)$
  $i = i+1$
end while
Terminate.

Table 3.1 Simulation Parameters

Parameter	**Specification**
Filter	PHYDYAS prototype filter [11]
Overlapping factor (D)	4
Channel Bandwidth	5 MHz
Total number of Subcarriers	128
Number of PRBs	6
Number of Subcarriers per PRB	12
Subcarriers spacing	15 KHz
Number of slots	2
Number of symbols per slot	7
Modulation	4-QAM, 16-QAM
Number of IIC iterations	0, 1, 2, 3, 5
LTE Channel model	EVA, ETU

3.4 Simulation Results

In this section, simulation results are presented for the proposed IIC receiver for FBMC-QAM. Also, the PSD of FBMC-QAM with a single prototype filter, FBMC-QAM with two prototype filters, FBMC-OQAM and OFDM are presented. For the filter implementation in FBMC-QAM and FBMC-OQAM, the PHYDYAS prototype filter with overlapping factor $D = 4$ is used [11]. As mentioned in Chapter 2, the choice of filter is motivated by results [53], which showed that the PHYDYAS prototype filter achieves the lowest OOB emission performance compared to other prototype filters. In addition, it is shown in [14] that the PHYDYAS prototype filter achieves good performance when applied to interference cancellation receivers. The prototype filter coefficients are defined as shown in

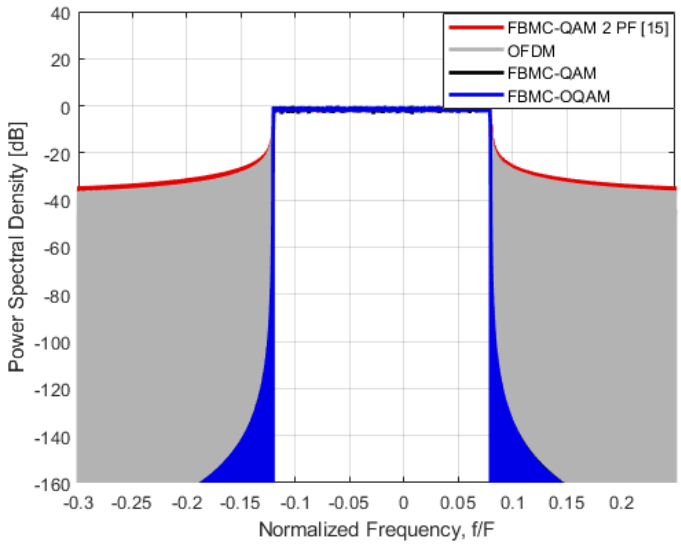

Fig. 3.4 PSD comparison between OFDM, FBMC-OQAM, FBMC-QAM orthogonal, and FBMC-QAM non-orthogonal.

2.29. For the multipath channel model, the frequency selective EVA and ETU channel models are considered as specified by 3GPP for LTE [35]. The simulation parameters are illustrated in Table 3.1.

Fig. 3.4 shows the PSDs of OFDM, FBMC-OQAM, conventional FBMC-QAM with two prototype filters and the proposed FBMC-QAM with a single prototype filter. Note that the FBMC-QAM system with two prototype filters in [19] adopts the PHYDYAS for even-numbered subcarriers and a reordered version of it for odd-numbered subcarriers in order to achieve orthogonality in AWGN channels. As shown in Fig. 3.4, the filter design in [19] results in a slightly worse OOB emission performance compared to OFDM. This is because of the discontinuities in one of the two prototype filters used for the time domain subcarrier filtering. However, Fig. 3.4 shows that the proposed FBMC-QAM system has the same OOB emission performance as FBMC-OQAM. This is mainly due to the better frequency localization of the PHYDYAS prototype filter employed for the per-subcarrier filtering in both cases.

Fig. 3.5 and Fig. 3.6 illustrate the BER performance of the proposed IIC receiver for FBMC-QAM systems in the EVA and ETU channel models, respectively. Note that the data symbols are 4-QAM modulated and a one-tap frequency domain ZF equalization is performed. As mentioned above, the receiver has perfect CSI. The results of the IIC receiver is compared with the case with perfect interference cancellation (PeIC) as well as a benchmark CP-OFDM model. For the implementation of the PeIC scenario, I_{ISI}^{even}, I_{ICI}^{odd}, I_{ISI}^{odd} and I_{ICI}^{even} are calculated directly from the transmitted signal, instead of the estimated signal. For the benchmark CP-OFDM case, a system with sufficient CP and guard band is considered, which implies that the benchmark system avoids both ISI and ICI.

It can be seen in these figures that the BER performance is improved after a few IIC iterations. As shown in Fig. 3.5, the gap from the PeIC case is approximately 2 dB after 3 IIC iterations, measured at

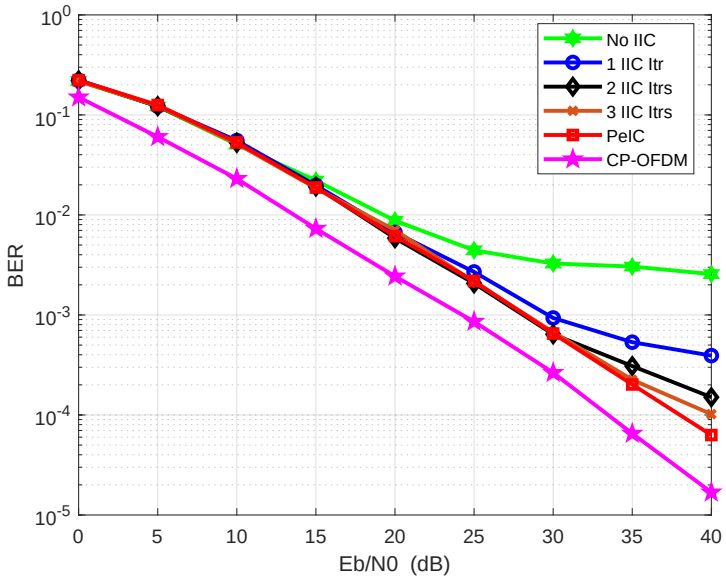

Fig. 3.5 BER performance of uncoded FBMC-QAM with IIC using 4-QAM over LTE-EVA Channel.

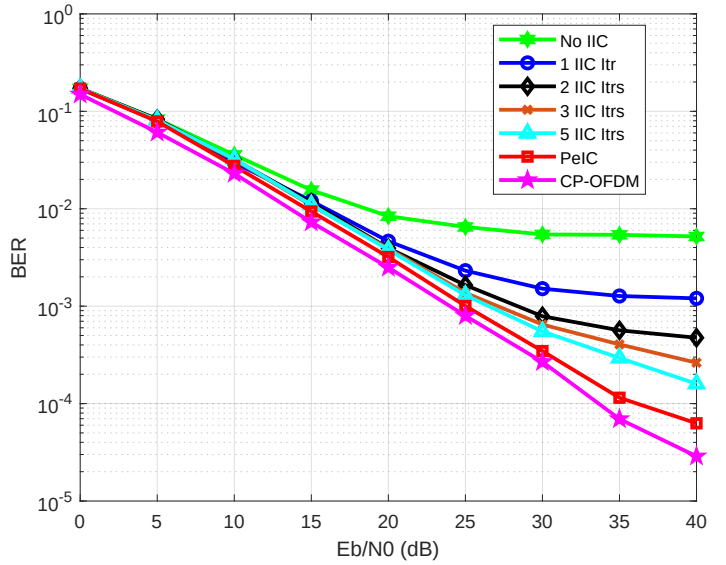

Fig. 3.6 BER performance of uncoded FBMC-QAM with IIC using 4-QAM over LTE-ETU Channel.

10^{-4} BER. Moreover, the benchmark CP-OFDM systems achieves better performance by using extra resources as CP and guard band. From Fig. 3.6, it is observed that even after 5 iterations there still remains an error floor under the ETU channel, though the error floor performance is improved after each iteration. In addition it can be seen that the gap between PeIC results and the benchmark OFDM becomes narrow in in ETU channel. This is because with the higher selectivity in ETU affects the

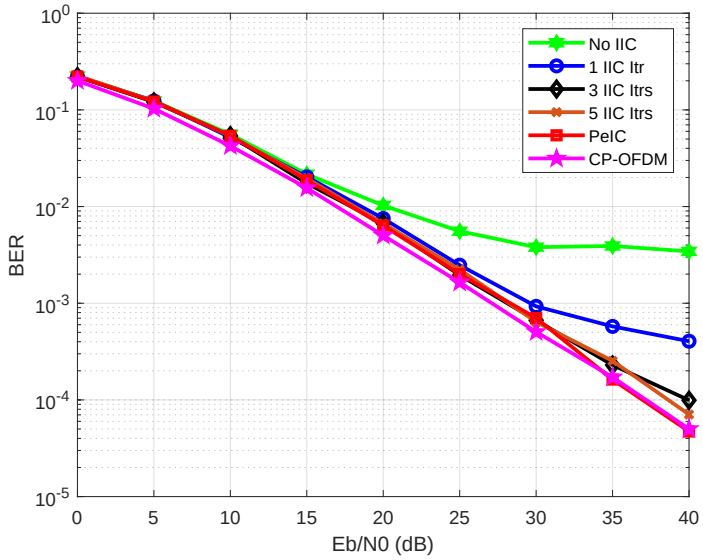

Fig. 3.7 BER performance of uncoded FBMC-QAM with IIC using 16-QAM over LTE-EVA Channel.

performance of CP-OFDM. Chapter 4 will consider the use of channel coding and iterative decoding to address the error floor problem in this chapter. In addition, Chapter 4 will present a comprehensive study of the convergence and complexity of the IIC receiver with iterative decoding.

Fig. 3.7 shows the BER performance of the proposed IIC receiver for FBMC-QAM systems with 16-QAM over the EVA channel. As can be observed from Fig. 3.7, the error floor is improved significantly after 5 iterations. Measured at 10^{-4}, the gap between 5 iterations of IIC and the PeIC case is less than 2 dB. This implies that 5 iterations are enough to obtain an acceptable BER performance and more than 5 iterations will not improve the performance much. To fully understand the benefit of the proposed receiver, its complexity compared to the benchmark CP-OFDM case is essential. The complexity analysis of the IIC receiver is presented in Chapter 4.

3.5 Summary

In this chapter, the use of IIC to remove the intrinsic interference in FBMC-QAM systems is investigated. In order to effectively cancel the intrinsic interference in FBMC-QAM systems, a receiver is proposed which separates the received signal into even- and odd-numbered subcarrier components, and uses the decoded even- and odd-numbered subcarrier symbols to iteratively cancel the interference from subsequent symbols. Numerical simulations show that the IIC algorithm can significantly improve the BER performance of the proposed FBMC-QAM system under different time-varying channels. For example, for the case of 16-QAM in the EVA channel, it is shown that 5 IIC iterations achieve near optimum BER performance. Also, the OOB emission performance is identical to FBMC-OQAM and is superior to that of both OFDM and conventional FBMC-QAM with two

prototype filters. Since the IIC receiver shows the capability to address the intrinsic interference problem, FBMC-QAM becomes a suitable alternative to OFDM for future wireless applications due to its high spectral efficiency and suitability for asynchronous transmissions. However, in order to solve the error floor problem in this chapter and improve the IIC performance, Chapter 4 will investigate the use of channel coding and decoding in FBMC-QAM.

Chapter 4

Iterative Interference Cancellation based BICM-ID in Coded FBMC-QAM Systems

4.1 Introduction

In Chapter 3, it was shown that an IIC receiver is capable of removing the intrinsic interference in FBMC-QAM systems. However, in highly frequency selective channels an error floor appears in the BER performance at high SNR. To improve the decoding performance, efficient channel coding and the corresponding BICM-ID are essential in modern wireless communication system design [131, 132]. Through multiple detection and decoding iterations, BICM-ID receivers can approach the optimal decoding performance of different communication systems. Thus, BICM-ID is an essential technique for meeting the high data rate and reliability requirements of future wireless applications. As introduced in Chapter 2, the BICM-ID receiver consists of a SISO demapper and a channel decoder that iteratively exchange "soft" information to improve detection performance. Recently, some works in the literature have investigated the combination of BICM-ID and IIC to remove the interference terms in multicarrier systems [14, 130, 133, 134]. In [134], the application of non-binary LDPC coding to FBMC-OQAM was investigated. It was shown that existing adaptive coding and modulation schemes can be easily modified to accommodate the properties of non-binary LDPC and FBMC-OQAM. An LDPC-based BICM-ID receiver is investigated for a single antenna FBMC-OQAM and a MIMO FBMC-OQAM in [130] and [133], respectively.

The purpose of this chapter is to show that the error floor problem encountered in Chapter 3 can be tackled effectively through the application of channel encoding at the transmitter and a corresponding BICM-ID at the receiver of an FBMC-QAM system. Thus, the IIC processing at the receiver side becomes more efficient in cancelling the intrinsic interference introduced by the loss of orthogonality in FBMC-QAM. Specifically, LDPC encoding is used to encode the transmitted bits at the transmitter

side whereas a combination of BICM-ID and IIC is implemented at the receiver side to improve the decoding performance. The proposed receiver consists of two components: (1) *inner decoder* - which performs FBMC-QAM demodulation and demapping in the one direction and FBMC-QAM modulation and symbol mapping in the opposite direction; (2) *outer decoder* - which is an LDPC decoder.

The remainder of the chapter is organized as follows. Section 4.2 describes the FBMC-QAM system model. The structure of the proposed IIC-based BICM-ID receiver is presented in Section 4.3. The convergence behaviour of the proposed iterative receiver using EXIT-chart analysis is presented in Section 4.4. Performance and complexity evaluation of the BICM-ID receiver for different frequency-selective channels are illustrated in Section 4.5. Finally, a summary of this chapter is presented in Section 4.6.

4.2 System Model

The transceiver structure of the proposed IIC-based BICM-ID system is shown in Fig. 4.1. Similar to Chapter 3, a single antenna FBMC-QAM system is considered in this chapter. In addition, a single prototype filter is used on both even and odd subcarriers to maintain the superior OOB emission property of FBMC systems. Moreover, to address the error floor problem in the uncoded FBMC-QAM system considered in Chapter 3, a coded FBMC-QAM system is implemented in this chapter. At the transmitter, a stream of information bits $\mathbf{b} = [b_1, b_2, \ldots, b_{L_b}]$ of length L_b are encoded by a channel encoder. The encoder outputs a codeword $\mathbf{c} = [c_1, c_2, \ldots, c_{L_c}]$ of length L_c with a coding rate of $R_c = L_b/L_c$. An LDPC encoder is considered in this chapter due to its advantages over turbo coding, which has resulted in its widespread application in modern communication systems, such as IEEE 802.11n and 5G NR. The encoded bits are randomly interleaved in order to randomize the burst errors and a set of $\mathscr{M}$ interleaved bits $\{a_n^1, a_n^2, \ldots, a_n^{\mathscr{M}}\}$ are QAM modulated to the n-th FBMC-QAM symbol $\mathbf{a}_n$, where $a_n^q \in \{\pm 1\}$ denotes the q-th bit of $\mathbf{a}_n$. The resulting signal goes through FBMC-QAM modulation, which consists of a serial-to-parallel converter, IFFT, a SFB block and a parallel-to-serial converter. After IFFT, the discrete time-domain FBMC-QAM signal vector associated with the n-th symbol can be expressed as

$$\mathbf{s}_n = \Phi^H \mathbf{a}_n \tag{4.1}$$

where $\mathbf{a}_n = [a_{0,n}, a_{1,n}, \ldots, a_{M-1,n}]$ is the $M \times 1$ symbol vector in the frequency domain before IFFT, $a_{m,n}$ is the data at the m-th subcarrier of the n-th symbol, M is the total number of subcarriers and Φ is the $M \times M$ unitary DFT matrix whose entry on the l-th row and t-th column is $(1/\sqrt{M})e^{-j\frac{2\pi lt}{M}}$.

The IFFT output is oversampled by the overlapping factor D and filtered by the SFB. The oversampling is performed because the duration of typical prototype filter in FBMC systems is

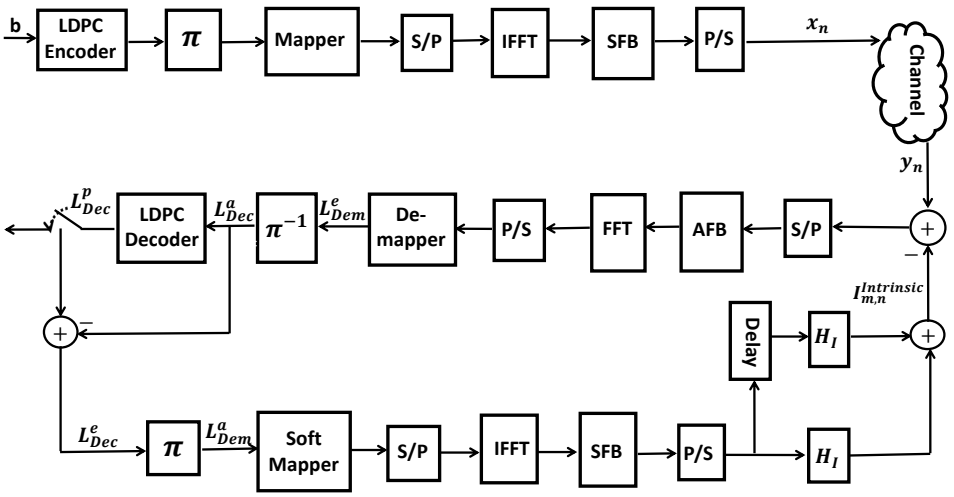

Fig. 4.1 Block diagram of transmitter and BICM-ID receiver

multiple times the FFT size. The signal after SFB processing is given as

$$\begin{aligned} \mathbf{x}_n &= \mathbf{G}\mathbf{s}_n \\ &= \mathbf{G}\Phi^H \mathbf{a}_n \end{aligned} \tag{4.2}$$

where $\mathbf{x}_n = [x_{0,n}, x_{1,n}, \ldots, x_{L_p-1,n}]$ is the vector of the transmitted data, $L_p = D \times M$ and $\mathbf{G}$ is the SFB matrix whose l-th row and t-th column is given as [129]

$$[\mathbf{G}]_{lt} = \begin{cases} g[(l-t)M], & \text{for } 0 \leq l-t < D \\ 0, & \text{otherwise} \end{cases} \tag{4.3}$$

with $g[i]$ as the prototype filter impulse response. As in Chapter 3, the PHYDYAS prototype filter is employed for the per-subcarrier filtering in this chapter.

In the presence of a frequency-selective fading channel, the discrete-time domain FBMC-QAM signal vector at the receiver is given by

$$\mathbf{y}_n = \mathbf{H}\mathbf{x}_n + \mathbf{z}_n \tag{4.4}$$

where $\mathbf{H}$ denotes the $L_p \times L_p$ multipath channel matrix with entries given as

$$[\mathbf{H}]_{\tau_1,\tau_2} = \begin{cases} h(\tau_1 - \tau_2), & \text{for } 0 \leq \tau_1 - \tau_2 < L_{ch}, \\ 0, & \text{otherwise} \end{cases} \tag{4.5}$$

$h(\tau)$ is the time-domain multipath channel impulse response, τ is the multipath delay, L_{ch} is the length of the channel and $\mathbf{z}_n$ is the $L_p \times 1$ vector representing the AWGN. The received signal is passed

through the FBMC-QAM demodulator, which reverses the operations of the FBMC-QAM modulator (See Fig. 4.3). First, the received signal is processed by the AFB. The AFB is chosen to be the complex conjugate and time reverse version of the SFB in order to satisfy the NPR condition [130]. Thus, the signal at the output of AFB after receive filtering is expressed as

$$\begin{aligned}\mathbf{y}_n^f &= \mathbf{G}^H\mathbf{y}_n \\ &= \mathbf{G}^H\mathbf{H}\mathbf{x}_n + \mathbf{G}^H\mathbf{z}_n \\ &= \mathbf{H}^f\mathbf{a}_n + \mathbf{z}_n^f\end{aligned} \tag{4.6}$$

where $\mathbf{H}^f = \mathbf{G}^H\mathbf{H}\mathbf{G}\Phi^H$ is the $L_p \times L_p$ effective channel matrix after filtering and $\mathbf{z}_n^f = \mathbf{G}^H\mathbf{z}_n$. Then, down-sampling followed by FFT is performed on the filtered signal to obtain the frequency domain signal vector, $\mathbf{r}_n = [r_{0,n}, r_{1,n}, \ldots, r_{M-1,n}]$. The output of the FFT is given by

$$\begin{aligned}\mathbf{r}_n &= \Phi\mathbf{y}_n^f \\ &= \Phi\mathbf{H}^f\mathbf{a}_n + \Phi\mathbf{z}_n^f \\ &= \tilde{\mathbf{H}}\mathbf{a}_n + \tilde{\mathbf{z}}_n\end{aligned} \tag{4.7}$$

where $\tilde{\mathbf{H}} = \Phi\mathbf{G}^H\mathbf{H}\mathbf{G}\Phi^H$ represents the $M \times M$ effective channel matrix after FFT and $\tilde{\mathbf{z}} = \Phi\mathbf{G}^H\mathbf{z}_n$ is the coloured noise. From (4.7), the received FBMC-QAM signal associated with m-th subcarrier and the n-th symbol can be expressed as

$$r_{m,n} = \tilde{\mathbf{H}}_{m,n}a_{m,n} + I_{m,n}^{intrinsic} + \tilde{z}_{m,n} \tag{4.8}$$

where $I_{m,n}^{intrinsic}$ represents the intrinsic interference caused by the loss of complex orthogonality in FBMC-QAM, which can be expressed as

$$I_{m,n}^{intrinsic} = \underbrace{\sum_{i\neq m}\tilde{\mathbf{H}}_{i,n}^{ICI}a_{i,n}}_{ICI} + \underbrace{\sum_{j\neq n}\sum_{m=0}^{M-1}\tilde{\mathbf{H}}_{m,j}^{ISI}a_{m,j}}_{ISI} \tag{4.9}$$

with $\tilde{\mathbf{H}}_{i,n}^{ICI}$ and $\tilde{\mathbf{H}}_{m,j}^{ISI}$ as the residual channels that lead to ICI and ISI, respectively. Note that the characteristics of $\tilde{\mathbf{H}}_{i,n}^{ICI}$ and $\tilde{\mathbf{H}}_{m,j}^{ISI}$ are determined by the type of prototype filter and the fading channel effect. Therefore, by using a single prototype filter the effective channel will vary only with the channel fading effect unless a different prototype filter is selected. To achieve optimum decoding performance, the ICI and ISI terms must be estimated and cancelled from the received signal. To do this, the interference channels $\tilde{\mathbf{H}}_{i,n}^{ICI}$ and $\tilde{\mathbf{H}}_{m,j}^{ISI}$ must be estimated at the receiver. The interference channel matrix can be expressed as [130]

$$\tilde{\mathbf{H}}_{i,j}^{I} = \begin{bmatrix} 0_{E\times(N-E)} & \mathbf{H}_E \\ 0_{(N-E)\times(N-E)} & 0_{(N-E)\times E}\end{bmatrix} \tag{4.10}$$

where $I = ICI, ISI$, $\mathbf{H}_E \in \mathbb{C}^{E\times E}$, with $E = L_{ch} - 1$, is given by

$$\mathbf{H}_E = \begin{bmatrix} h_{Lch-1} & \dots & \dots & h_0 \\ 0 & \ddots & & \vdots \\ \vdots & \ddots & \ddots & \vdots \\ 0 & \dots & 0 & h_{L_{ch}-1} \end{bmatrix} \tag{4.11}$$

Before detection and decoding of the received signal, the effects of the frequency-selective channel is compensated by applying a simple one-tap ZF equalizer. The resulting signal is given as

$$\begin{aligned} \tilde{r}_{m,n} &= \frac{r_{m,n}}{\tilde{\mathbf{H}}_{m,n}} \\ &= a_{m,n} + \frac{I_{m,n}^{intrinsic}}{\tilde{\mathbf{H}}_{m,n}} + \frac{\tilde{z}_{m,n}}{\tilde{\mathbf{H}}_{m,n}} \end{aligned} \tag{4.12}$$

The equalized signal is deinterleaved and passed to the LDPC decoder for decoding and detection. The receiver processing is repeated for several iterations to get rid of the intrinsic interference through decoding and IIC. This is described in detail in the next section.

4.3 IIC-based BICM-ID Receiver

In order to recover the transmitted bits, an IIC-based BICM-ID receiver is proposed as shown in Fig. 4.2. It is made up of two component decoders:

- The *Inner Decoder* - which consists of a soft mapper, a soft demapper, an FBMC-QAM modulator and demodulator, and an IIC operation.
- The *Outer Decoder* - which is an LDPC decoder consisting of two types of nodes: VND and CND.

This receiver structure is chosen in order to aid the efficient detection and decoding of the received signal through SISO decoding and interference cancellation. In each receiver iteration, the inner decoder uses the received signal vector $\mathbf{y}_n$ and the *a priori* LLR from the outer decoder to improve the decoding performance. In addition, the inner decoder enables symbol regeneration and interference cancellation to remove the intrinsic interference in FBMC-QAM. Specifically, the proposed IIC-based BICM-ID receiver performs two iterative processes: (i) the exchange of MI between the VND and CND of the outer decoder and (ii) the exchange of MI between the inner decoder and outer decoder. The inner decoder takes the received signal vector $\mathbf{y}_n$ and the *a priori* information of the coded bits, $L_{Dem,a}^{q,n}$, from the outer decoder ($L_{Dem,a}^{q,n} = 0$ in the first receiver iteration) and computes the *a posteriori* LLRs as

$$L_{Dem}^{q,n} = L_{Dem,a}^{q,n} + L_{Dem,e}^{q,n} \tag{4.13}$$

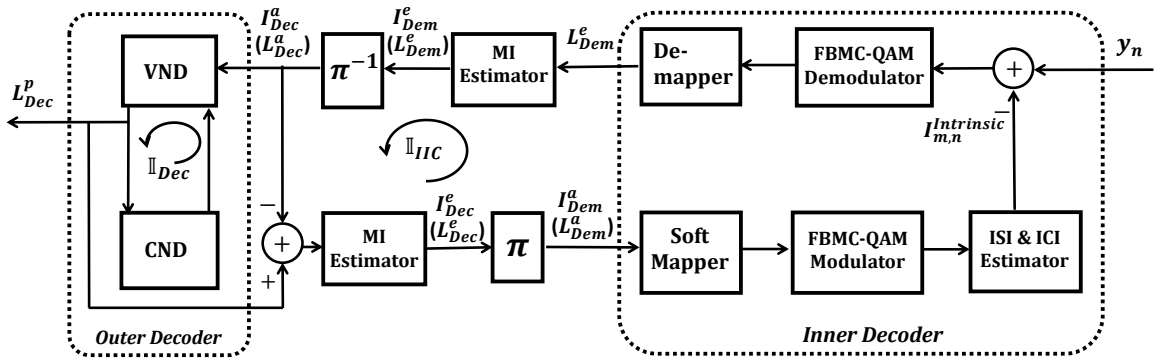

Fig. 4.2 IIC-based BICM-ID system model for EXIT chart analysis

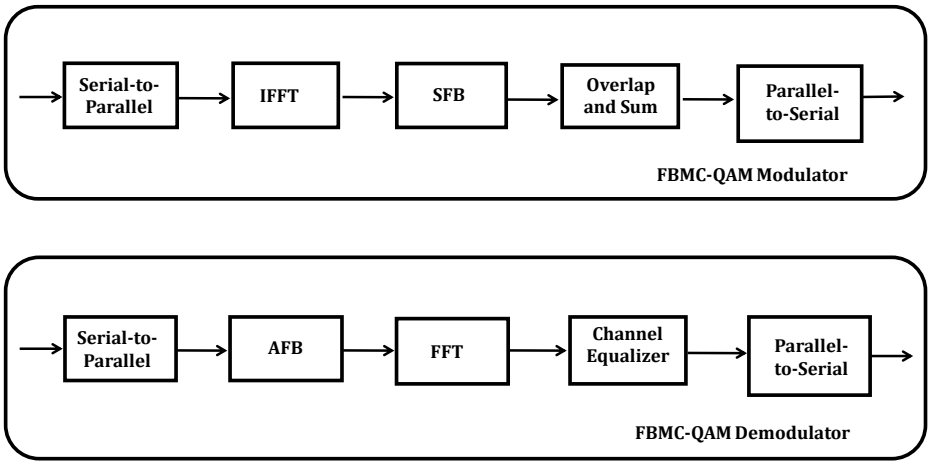

Fig. 4.3 FBMC-QAM modulator and demodulator

where $L^{q,n}_{Dem,e}$ is the extrinsic LLR values of the inner decoder. Using the maximum *a posteriori* demapping algorithm, $L^{q,n}_{Dem,a}$ and $L^{q,n}_{Dem,e}$ can be expressed as [132]

$$L^{q,n}_{Dem,a} = \log \frac{p(a^q_n = +1 \mid \tilde{r}_n)}{p(a^q_n = -1 \mid \tilde{r}_n)} \tag{4.14}$$

and

$$L^{q,n}_{Dem,e} = \log \frac{\sum\limits_{a \in a^+_q} p(\tilde{r}_n \mid a) \prod\limits_{\substack{q'=1 \\ q' \neq q}} p(a^{q'}_n)}{\sum\limits_{a \in a^-_q} p(\tilde{r}_n \mid a) \prod\limits_{\substack{q'=1 \\ q' \neq q}} p(a^{q'}_n)} \tag{4.15}$$

The extrinsic LLR values, $L^{q,n}_{Dem,e}$, are de-interleaved and passed to the outer decoder as *a priori* LLR, $L^{q,n}_{Dec,a}$, for channel decoding. After a number of iterations between the CND and VND of the

Algorithm 2 IIC-based BICM-ID Receiver Algorithm

Require: $\mathbf{r}_n$, $\mathbb{I}_{Dec}^{max}$, $\mathbb{I}_{IIC}^{max}$. Initialize number of iterations $i = 0$
while $i \leq \mathbb{I}_{IIC}^{max}$ **do**
  Perform FBMC-QAM demodulation of received signal.
  Calculate extrinsic LLR values at soft demapper.
  Deinterleave extrinsic LLR values to obtain *a priori* LLR , $L_{Dec,a}^{q,n}$.
  while $i \leq \mathbb{I}_{Dec}^{max}$ **do**
    Pass $L_{Dec,a}^{q,n}$ between VND and CND for defined number of iterations.
  end while
  Interleave extrinsic LLR values of LDPC decoder to obtain *a priori* LLR for soft mapper.
  Determine estimate of the transmit signal $\hat{\mathbf{a}}_n$.
  Pass the estimated signal through the FBMC-QAM modulator.
  Estimate intrinsic interference as shown in (4.9).
  Subtract the estimated interference terms from the received signal.
  $i = i + 1$
end while
Make hard decision to obtain final estimates of the transmitted bits, $\hat{\mathbf{b}}$.
Terminate.

outer decoder, it computes *a posteriori* LLRs, $L_{Dec,p}^{q,n}$. The outer decoder extrinsic information, defined as $L_{Dec,e}^{q,n} = L_{Dec,p}^{q,n} - L_{Dec,a}^{q,n}$, is re-interleaved and passed to the soft mapper as *a priori* information, $L_{Dem,a}^{q,n}$. To estimate and cancel the effect of the intrinsic interference term in (4.12), the output of the soft mapper is FBMC-QAM modulated and the estimated symbols are subtracted from the received signal for the next iteration as shown in Fig. 4.2. The number of iterations between the inner decoder and the outer decoder is denoted by $\mathbb{I}_{IIC}$ and the number of iterations within the outer decoder is denoted by $\mathbb{I}_{Dec}$. After the final iteration in both iterative processes, $L_{Dec,p}^{q,n}$ is used to generate the hard-decision estimates of the transmitted bits. The iterative process of the proposed IIC-based BICM-ID receiver proceeds as shown in Algorithm 2. Furthermore, the complexity analysis of the proposed receiver is presented in subsection 4.4.4.

4.4 Convergence Analysis of IIC-Based BICM-ID Receiver

EXIT charts are useful for studying the convergence of iterative decoders [135]. In EXIT chart analysis the exchange of MI between the components of an iterative receiver is tracked in order to predict the required number of iterations and convergence threshold of the receiver. As explained in Chapter 2, the EXIT chart is an important analytical technique since it can be used to gain insight into the convergence properties of an iterative receiver without an actual simulation of the transmitter and receiver. Therefore, in this chapter, EXIT chart analysis is used to visualize the exchange of MI between the inner decoder and outer decoder. This provides an indication of the convergence behaviour of the proposed IIC-based BICM-ID receiver. Note that the MI expression for the inner and outer decoders are derived as shown in Chapter 2.

4.4.1 EXIT Chart of Inner Decoder

Notice from Fig. 4.2 that the MI at the output of the inner decoder is dependent on two inputs, namely, the *a priori* MI, I^a_{Dem}, coming as feedback from the outer decoder and the received signal coming from the channel. Thus, following the derivations in Subsection 2.4.4, the inner decoder's EXIT characteristics can be defined by the *a priori*-extrinsic transfer function $\mathbb{T}$ as

$$I^e_{Dem} = \mathbb{T}[I^a_{Dem}, \sigma_n^2] \tag{4.16}$$

where $I^e_{Dem} = I[x; L^{q,n}_{e,Dem}]$, $0 \leq I^e_{Dem} \leq 1$, is the extrinsic MI of the inner decoder and σ_n^2 is the channel noise variance. I^e_{Dem} can be obtained from (2.64) as

$$I^e_{Dem} = 1 - \frac{1}{T}\sum_{t=1}^{T} \log_2[1 + \exp(-x_t \cdot L^{q,n}_{e,Dem})] \tag{4.17}$$

The extrinsic LLR of the inner decoder, $L^{q,n}_{e,Dem}$, is then deinterleaved and passed to the outer decoder as *a priori* LLR, $L^{q,n}_{a,Dec}$.

4.4.2 EXIT Chart of Outer Decoder

The outer decoder accepts *a priori* input, $L^{q,n}_{a,Dec}$, from the inner decoder and alternates this information between the VND and CND processing for a predefined number of iterations, $\mathbb{I}_{Dec}$. When the decoding process is complete it returns extrinsic LLR, $L^{q,n}_{e,Dec}$. This is represented by the transfer function

$$I^e_{Dec} = \mathbb{T}[I^a_{Dec}] \tag{4.18}$$

where $I^a_{Dec} = I[x; L^{q,n}_{a,Dec}]$, $0 \leq I^a_{Dec} \leq 1$, is the MI between the encoded bits stream and the *a priori* LLR, $L^{q,n}_{a,Dec}$ and $I^e_{Dec} = I[x; L^{q,n}_{e,Dec}]$, $0 \leq I^e_{Dec} \leq 1$ is the extrinsic MI of the outer decoder which can be computed according to (2.64) as

$$I^e_{Dec} = 1 - \frac{1}{T}\sum_{t=1}^{T} \log_2[1 + \exp(-x_t \cdot L^{q,n}_{e,Dec})] \tag{4.19}$$

For the next IIC iteration the extrinsic LLR from the outer decoder, $L^{q,n}_{e,Dec}$, is re-interleaved and passed to the inner decoder as *a priori* LLR, $L^{q,n}_{a,Dem}$.

4.4.3 Convergence Analysis

Given the MI of the inner and outer decoders, the convergence behaviour of the IIC-based BICM-ID receiver can be visualized by plotting the EXIT characteristics of the two decoders on an EXIT chart. The inner decoder EXIT curve is dependent on the noise variance or the SNR value of the received signal while the outer decoder EXIT curve varies with the number of decoder iterations, $\mathbb{I}_{Dec}$. The

outer decoder's extrinsic MI, I^e_{Dec}, is feedback to the inner decoder as *a priori* MI, I^a_{Dem}, and is plotted on the x-axis of the EXIT chart. Likewise, the inner decoder's extrinsic MI, I^e_{Dem}, is passed to the outer decoder as *a priori* information, I^a_{Dec}, which represents the y-axis of the EXIT chart. For near capacity decoding performance, a pair of inner and outer decoder EXIT curves should not intersect before the (1,1) point on the EXIT chart. In this case, an open area or tunnel exists between the two curves and the exchange of MI can be visualized as a "zig-zag" trajectory on the EXIT chart as shown in Fig. 4.6. The wider the tunnel, the lower the number of iterations required to reach the (1,1) point and vice versa. On the other hand, if any pair of inner and outer decoder EXIT curves intersect before reaching $I^a_{Dem} = 1$ on the horizontal axis, the tunnel is said to be "blocked". In this case the EXIT chart does not converge and a poor BER performance is obtained even with a high number of IIC iterations. Therefore, to achieve near capacity performance at a low receiver complexity, a trade-off between the SNR values, number of outer decoder iterations and the width of the EXIT tunnel must be obtained. That is, on the one hand, a high SNR can help achieve a wider EXIT tunnel at the expense of increased transmit power. On the other hand, a large number of outer decoder iterations will increase receiver complexity. For any system, the optimal choice of these parameter can be predicted using the EXIT chart analysis. The convergence behaviour of the proposed receiver is studied by Monte-Carlo simulations in the next section.

4.4.4 Complexity Analysis

This subsection presents the complexity evaluation of the proposed IIC-based BICM-ID receiver for FBMC-QAM compared with the benchmark CP-OFDM system. The overall complexity of the receiver depends on: (i) the modulator/demodulator processing in the inner decoder (ii) the VND and CND processing in the outer decoder and (iii) the number of outer decoder and IIC iterations. Mathematically, this complexity can be expressed as [136]

$$C_{BICM-ID} = \mathbb{I}_{Dec} \cdot (\mathbb{I}_{IIC} + 1) \cdot C_{outer} \cdot N_b + N_s \cdot [C_{inner,1} + \mathbb{I}_{IIC} \cdot C_{inner,i}] \tag{4.20}$$

where C_{outer} denotes the complexity of the outer decoder, $C_{inner,1}$ is the complexity of the first iteration of the inner decoder with no *a priori* information from the outer decoder and $C_{inner,i}$ is the complexity of the i-th iteration of the inner decoder considering the *a priori* information from the outer decoder. N_b and N_s represent the number of information bits at the input of the LDPC encoder and number of symbols, respectively. Recall that $\mathbb{I}_{Dec}$ and $\mathbb{I}_{IIC}$ are the number of outer decoder and IIC iterations, respectively. C_{outer} depends on the scheduling used to exchange messages between the CND and VND. Also, $C_{inner,1}$ depends on the complexity of the multicarrier (CP-OFDM or FBMC-QAM) demodulator during the initial decoder iteration whereas, $C_{inner,i}$ is the combined complexity of the multicarrier modulator and demodulator in subsequent decoder iterations.

As mentioned above, there is negligible intrinsic interference in the benchmark CP-OFDM system due to the use of sufficient CP and guard band. Therefore, there is no IIC iterations for the benchmark

CP-OFDM system. As a result, its complexity can be expressed as

$$\begin{aligned} C_{BICM-ID}^{OFDM} &= \mathbb{I}_{Dec} \cdot C_{outer} \cdot N_b + N_s \cdot C_{inner,1}^{OFDM} \\ &= \mathbb{I}_{Dec} \cdot C_{outer} \cdot N_b + N_s \cdot M/2\log_2(M) \end{aligned} \tag{4.21}$$

where $C_{inner,1}^{OFDM} = M/2\log_2(M)$ is the complexity of the CP-OFDM demodulator, computed by considering the number of complex multiplications in the M-point FFT of OFDM [16]. On the other hand, due to the loss of orthogonality in FBMC-QAM there exist intrinsic interference. Therefore, IIC is required to cancel the interference. Thus, the complexity of FBMC-QAM using the proposed BICM-ID receiver is given as

$$C_{BICM-ID}^{FBMC} = \mathbb{I}_{Dec} \cdot (\mathbb{I}_{IIC} + 1) \cdot C_{outer} \cdot N_b + N_s \cdot (1 + 2\mathbb{I}_{IIC}) \left[M/2\log_2(M) + DM\right] \tag{4.22}$$

The proof of (4.22) is given in Appendix A.1.

Notice from Fig. 4.6 that there is no significant gain in MI of the outer decoder beyond 8 iterations. Therefore, as an example, the number of outer decoder iterations in the CP-OFDM system is set to $\mathbb{I}_{Dec} = 8$. For this example, (4.21) can be rewritten as

$$C_{BICM-ID}^{OFDM} = 8 \cdot C_{outer} \cdot N_b + N_s \cdot M/2\log_2(M) \tag{4.23}$$

Moreover, as shown in Fig. 4.7, the FBMC-QAM system requires $\mathbb{I}_{Dec} = 2$ and $\mathbb{I}_{IIC} = 3$ to achieve a comparable BER performance with the benchmark CP-OFDM. In terms of complexity, this translates to

$$C_{BICM-ID}^{FBMC} = 8 \cdot C_{outer} \cdot N_b + 7N_s \cdot \left[M/2\log_2(M) + DM\right] \tag{4.24}$$

From (4.23) and (4.24) it can be seen that the complexity of the outer decoder is similar for both CP-OFDM and FBMC-QAM. Therefore, the difference in complexity between CP-OFDM and FBMC-QAM is dominated by the structure of their respective modulator/demodulator and the number of IIC iterations. Hence, (4.23) and (4.24) can be simplified as

$$C_{BICM-ID}^{OFDM} = N_s \cdot M/2\log_2(M) \tag{4.25}$$

and

$$C_{BICM-ID}^{FBMC} = 7N_s \cdot \left[M/2\log_2(M) + DM\right], \tag{4.26}$$

respectively.

Using the simulation parameters in Table 4.2 ($D = 4$ and $M = 128$), the computational complexity of the two systems are shown in Table 4.1. It can be observed that the number of complex multiplications increase with the number of IIC iterations. For $\mathbb{I}_{IIC} = 3$, which achieves similar BER performance as the CP-OFDM benchmark, the FBMC-QAM system requires 15 times more complexity than CP-OFDM. Note however that, the CP-OFDM benchmark consumes additional resources in

Table 4.1 Complexity of IIC-based BICM-ID receiver for CP-OFDM and FBMC-QAM

$\mathbb{I}_{IIC}$	**OFDM** (4.25)	**FBMC** (4.26)	**Hybrid**	**OFDM-FBMC Ratio**	**OFDM-Hybrid Ratio**
0	448	960	960	2.14	2.14
1	-	2880	2880	6.4	6.4
2	-	4800	-	10.7	-
3	-	6720	-	15	-

terms of CP and guard band in order to maintain orthogonality and avoid intrinsic interference. Since future IoT applications are expected to connect billions of user terminals, the extra resources and signaling required to maintain synchronous communication between terminals may be prohibitive. Furthermore, OFDM has been shown to perform poorly in asynchronous communications [130, 7]. This is as a result of the increased interference to adjacent subbands caused by the high spectrum leakage in OFDM. Moreover, it is shown in [130] that in the case of insufficient CP and guard band residual interference exist in CP-OFDM and IIC iterations may be needed to cancel this interference, which can increase the complexity of CP-OFDM.

Also, as shown in Table 4.1 the complexity of the proposed receiver is dominated by the signal processing at the FBMC-QAM modulator and demodulator inside the inner decoder. Therefore, to reduce complexity of the BICM-ID receiver for FBMC-QAM, the interference reconstruction can be based on the output of the soft mapper. This is equivalent to bypassing the FBMC-QAM modulator/demodulator in some IIC iterations. For example, consider a hybrid iterative system in which the first IIC iteration ($\mathbb{I}_{IIC} = 1$) involves both the FBMC-QAM modulator and demodulator. However, in subsequent IIC iterations ($\mathbb{I}_{IIC} > 1$), the interference cancellation is performed at the output of the soft mapper. This implies that, after the initial iteration without IIC and the first IIC iteration, the complexity of the hybrid iterative receiver is independent of the signal processing in the FBMC-QAM modulator/demodulator. From the example shown in Table 4.1, it can be seen that the ratio of complexity of the iterative receiver to that of CP-OFDM saturates at about 6.4 and increasing the number of IIC iterations will not significantly increase the complexity. Thus, the hybrid receiver can serve as a suboptimal approach that is capable of providing a trade-off between complexity and BER performance of the proposed iterative receiver. This implies that, with a small increase in complexity, the proposed IIC-based BICM-ID receiver can effectively remove the intrinsic interference in FBMC-QAM. With such a receiver, FBMC-QAM becomes a promising alternative to CP-OFDM in future applications due to its high spectral efficiency and suitability for grant-free asynchronous transmissions.

4.5 Simulation Results

In this section, numerical simulation results are presented to illustrate the OOB emission performance of different FBMC systems compared to CP-OFDM. Also, the EXIT chart analysis and BER performance of the proposed IIC-based BICM-ID receiver under different fading channel conditions are presented. The complexity of the proposed receiver for FBMC-QAM is studied and compared to the complexity of a CP-OFDM benchmark.

4.5.1 Simulation Setup

To evaluate the effectiveness of the IIC-based BICM-ID receiver for FBMC-QAM, computer simulations are conducted. For the LDPC decoder, an irregular parity-check matrix has been used whereas the sum-product decoding algorithm is employed as demapper [91]. To achieve effective convergence in the EXIT chart analysis, anti-gray mapping schemes have been proposed in the literature. Scheme such as set partitioning (SP), modified set partitioning (MSP), maximum squared Euclidean weight (MSEW) and the optimized mapping $M16^r$ have been shown to perform better than classical Gray mapping in EXIT chart analysis [137]. Therefore, for efficient performance, $M16^r$ is adopted in this simulation. For comparison, synchronous CP-OFDM is considered as a benchmark. For the benchmark implementation, it is assumed that the CP-OFDM system has sufficient CP and guard band in order to maintain orthogonality and synchronization between subbands. Also, the number of outer decoder iterations for CP-OFDM is set as $\mathbb{I}_{Dec} = 8$. This is because, as shown in Fig. 4.6, the MI of the outer decoder converges after 8 iterations, with negligible difference in MI from 8 to 10 iterations. Note that, similar to Chapter 3, an FBMC-QAM system with a single prototype filter for all subcarriers is considered in this chapter. For the filter implementation, the PHYDYAS prototype filter with overlapping factor $D = 4$ is used. The prototype filter coefficients are defined as shown in the Chapter 3.

To study the effect of fading on the proposed system, the 3GPP standardized channel models EPA, EVA and ETU are considered in this chapter. Moreover, perfect channel state information is assumed at both the transmitter and receiver. The simulation parameters are presented in Tables 4.2.

4.5.2 OOB Emission Performance

The PSD of CP-OFDM, FBMC-QAM with twin filters and FBMC-QAM with a single filter are given in Fig. 4.4. The FBMC-QAM system with twin filters, presented in [19], adopts the conventional PHYDYAS filter for even-numbered subcarriers and a reordered version of it for odd-numbered subcarriers in order to achieve orthogonality in AWGN channels. As can be seen, it achieves OOB emission that is worse than that of CP-OFDM. In frequency selective channels the orthogonality is lost because of the presence of residual interference, which degrades the BER performance. The optimized twin filters in [127] are designed to find a trade-off between intrinsic interference and OOB performance. As shown in Fig. 4.4, the optimized filter set improves the OOB performance compared

Table 4.2 Simulation Parameters

Parameter	**Specification**
Filter	PHYDYAS prototype filter
Overlapping factor (D)	4
Channel Bandwidth	1.4 MHz
Total number of subcarriers	12
Number of resource blocks (RBs)	6
Number of subcarriers per RBs	12
Subcarriers spacing	15 kHz
Number of slots per RBs	2
Number of symbols per slot	7
Modulation	16-QAM
LDPC Code rate	1/2
Mapping	$M16^r$
Number of IIC iterations	0, 1, 2, 3
Channel models	EPA, EVA, ETU

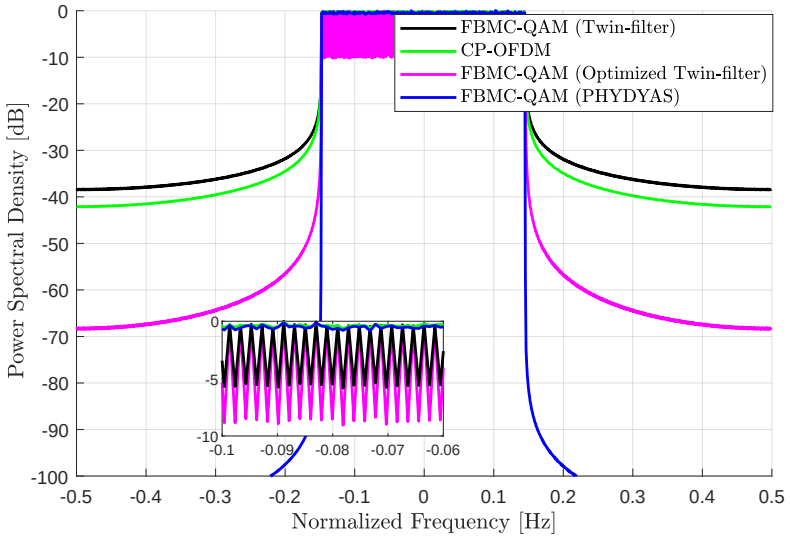

Fig. 4.4 PSD comparison of CP-OFDM, FBMC-QAM with twin filters and FBMC-QAM with single filter.

to both CP-OFDM and the filter set in [19]. The in-band spectrum of the different waveforms are also shown in Fig. 4.4. The twin-filter waveforms show an in-band fluctuation, as was the case in [129], which is absent in both CP-OFDM and FBMC-QAM with single filter.

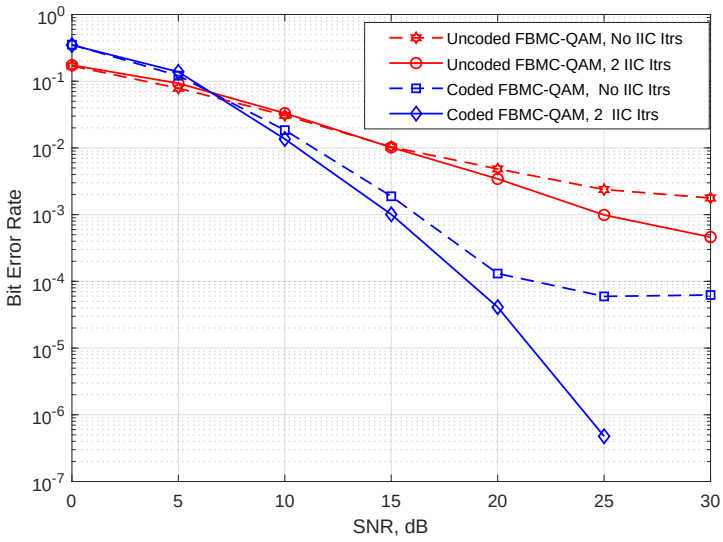

Fig. 4.5 BER performance of uncoded IIC receiver and proposed IIC-based BICM-ID receiver

By completely relaxing the orthogonality condition it can be seen that FBMC-QAM with single prototype filter has much lower OOB leakage than CP-OFDM and FBMC-QAM with twin filters. The ultra-low OOB emission means there is very low leakage interference between subbands (or users occupying these subbands). This implies that in asynchronous communications, FBMC-QAM users occupying adjacent subbands will cause negligible interference to each other. For mMTC applications, synchronous communication will be extremely difficult to manage due to the large number of user terminals. Moreover, the signaling overhead associated with the synchronous communication in CP-OFDM can consume a significant amount of the available time and frequency resources. Therefore, FBMC-QAM can enable the benefits of asynchronous and grant-free user transmissions to improve system capacity in future IoT applications.

4.5.3 Performance Comparison of Coded and Uncoded Systems

Fig. 4.5 compares the BER performance of the uncoded IIC receiver in Chapter 3 with the proposed IIC-based BICM-ID receiver over the EVA channel. As is expected, the results obtained for the IIC-based BICM-ID receiver outperforms that of the uncoded IIC receiver in Chapter 3. It can be seen from Fig. 4.5 that the error floor of the coded system can be significantly improved after just 2 iterations. However, the BER performance of the uncoded system is still poor after 2 iterations even at high SNR. This shows the benefit of the BICM-ID scheme employed in this chapter.

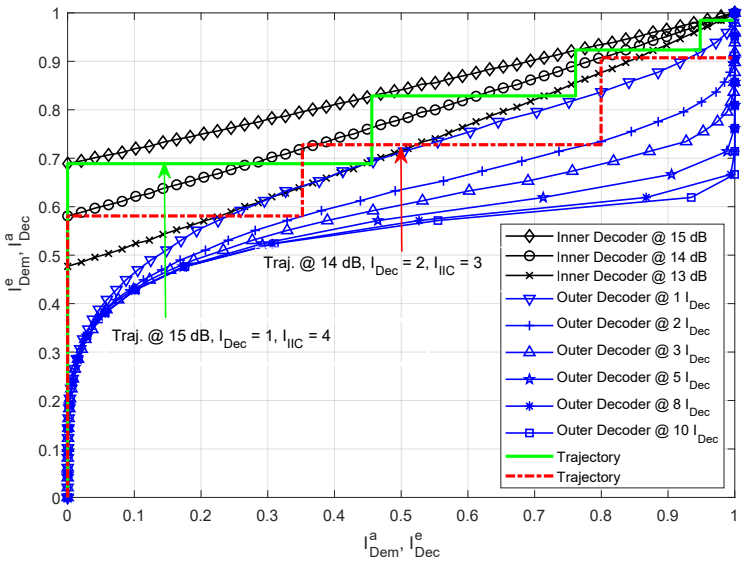

Fig. 4.6 EXIT function and decoding trajectories of the proposed IIC-based BICM-ID receiver over EPA channel.

4.5.4 EXIT Chart Performance of Single Fading Channel Realization

Fig. 4.6 and Fig. 4.7 show the performance of the proposed IIC-based BICM-ID receiver for FBMC-QAM and synchronous CP-OFDM over a single realization of the EPA channel. Recall that the MI of the inner decoder depends on the SNR values while the MI of the outer decoder varies with the number of iterations, $\mathbb{I}_{Dec}$. The EXIT curves of the inner and outer decoders are shown in Fig. 4.6. On the figure, the "zig-zag" trajectories represent the exchange of MI between the inner decoder and the outer decoder. Observe from Fig. 4.6 that at SNR of 13dB and $\mathbb{I}_{Dec} = 1$, the EXIT curve of the two component decoders intersect at $I^a_{Dem} \approx 0.25$. Therefore, as explained in Chapter 2, there is no open tunnel between the two curves and the decoding iteration does not converge. In this case, the tunnel between the two EXIT curves is said to be blocked. Therefore, increasing the number of IIC iterations, $\mathbb{I}_{IIC}$, will not improve the system performance. However, by increasing either the SNR or $\mathbb{I}_{Dec}$, the area between the two curves widens, resulting in an improved convergence behaviour of the BICM-ID receiver. For example, by increasing the SNR to 14dB and setting $\mathbb{I}_{Dec} = 2$ a tunnel opens between the two EXIT curves. The number of trajectories between the two curves show the number of iterations required to achieve convergence. The wider the tunnel between the two curves, the lower the number of trajectories (IIC iterations) required to reach the (1,1) point on the EXIT chart and the faster the receiver converges. The information on the number of iterations ($\mathbb{I}_{Dec}$ and $\mathbb{I}_{IIC}$) provided by the EXIT chart analysis can enable the prediction of the complexity of the proposed BICM-ID receiver.

The results on the EXIT chart is validated by the BER performance presented in Fig. 4.7. As can be seen, for $\mathbb{I}_{Dec} = 1$ the convergence threshold (turbo cliff/waterfall region) is obtained around

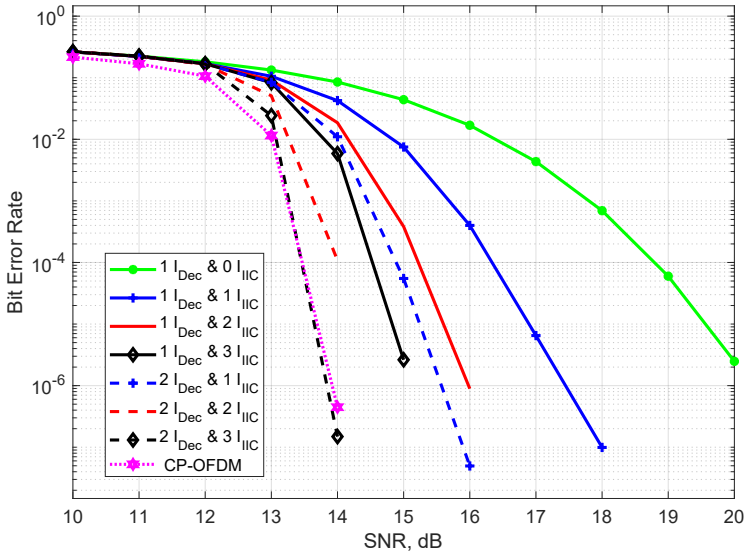

Fig. 4.7 BER performance of the proposed IIC-based BICM-ID receiver for FBMC-QAM and CP-OFDM over EPA channel

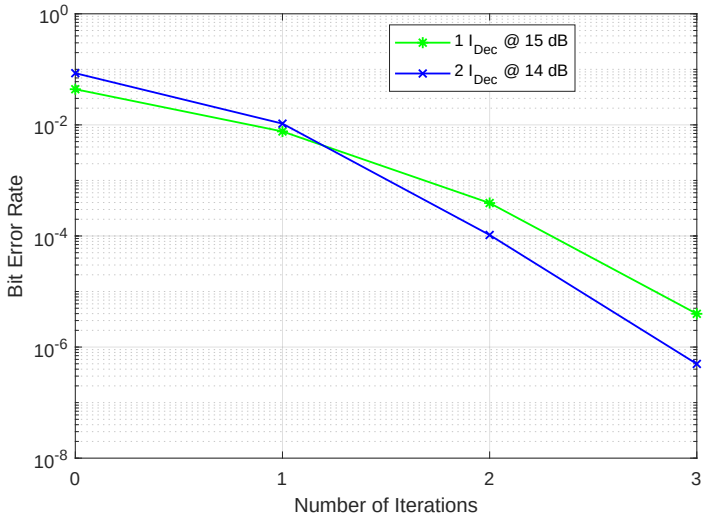

Fig. 4.8 BER performance vs number of IIC iterations of proposed receiver

14dB. Therefore, by increasing the number of IIC iterations the BER performance is significantly improved. Measured at a BER of 10^{-6} for $\mathbb{I}_{IIC}$ values of 1, 2 and 3, the proposed receiver show about 3dB, 4dB and 5dB SNR gain, respectively, when compared to the case with no IIC iterations. Moreover, by increasing $\mathbb{I}_{Dec}$ from 1 to 2 the convergence threshold occurs below 14dB. Hence, the decoding performance can be further improved with increasing IIC iterations. Compared to the benchmark CP-OFDM system, FBMC-QAM show about 6dB loss at 10^{-6} BER when no IIC

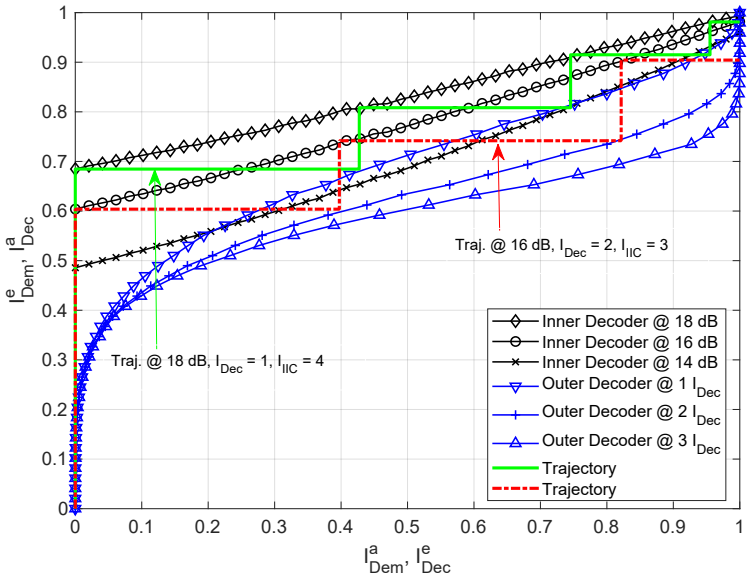

Fig. 4.9 EXIT function and decoding trajectories of the proposed IIC-based BICM-ID receiver over EVA channel.

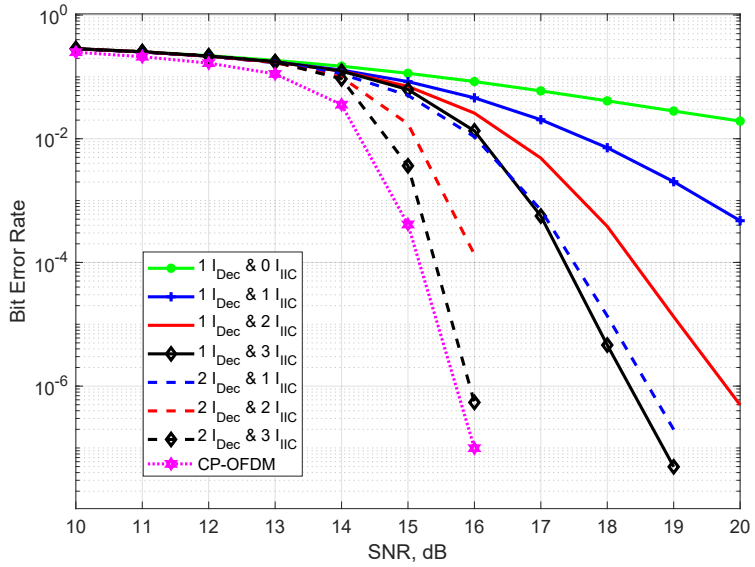

Fig. 4.10 BER performance of the proposed IIC-based BICM-ID receiver for FBMC-QAM and CP-OFDM over EVA channel

iterations are applied. Setting $\mathbb{I}_{Dec} = 2$ and $\mathbb{I}_{IIC} = 3$, FBMC-QAM achieve the same BER performance as the CP-OFDM benchmark. The BER plot versus number of IIC iterations is shown in Fig. 4.8 for $\mathbb{I}_{Dec} = 1$ and $\mathbb{I}_{Dec} = 2$. Fig. 4.8 highlights the fact that, for a fixed $\mathbb{I}_{Dec}$, increasing $\mathbb{I}_{IIC}$ improves the BER performance.

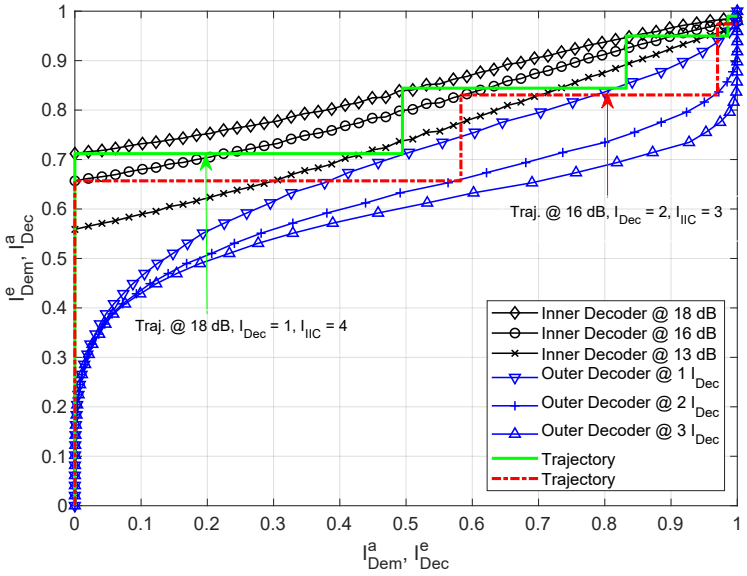

Fig. 4.11 EXIT function and decoding trajectories of the proposed IIC-based BICM-ID receiver over ETU channel.

Similarly, the performance of the proposed IIC-based BICM-ID receiver for FBMC-QAM and CP-OFDM over a single realization of the EVA and ETU channels are shown in Figs. 4.9, 4.10, 4.11 and 4.12. From Fig. 4.9, it can be seen that even though the EXIT curves at 14dB and $\mathbb{I}_{Dec} = 1$ allow an open tunnel in the EPA channel (see Fig. 4.6), they intersect in the EVA channel. This implies that either higher SNR values or more outer decoder iterations will be required to open a tunnel in the EVA channel. This is confirmed in Fig. 4.7 and Fig. 4.10 which show that with $\mathbb{I}_{Dec} = 1$ and $\mathbb{I}_{IIC} = 2$, a BER of 10^{-6} is obtained for the EPA channel at SNR of 16dB. However, an SNR of about 19.8dB is required to achieve a similar BER performance for the EVA channel. This is mainly due to the high frequency-selectivity of the EVA channel compared to EPA, which degrades the BER performance. Analogous to EPA, Fig. 4.10 and Fig. 4.12 show that once a tunnel has been created between the inner and outer decoder EXIT curves, increasing the number of IIC iteration can greatly improve the system performance by cancelling the interference caused by the non-orthogonality of FBMC-QAM and the high frequency selectivity of the EVA and ETU channels. Notice from Fig. 4.10 and Fig. 4.12 that, for $\mathbb{I}_{Dec} = 2$ and $\mathbb{I}_{IIC} = 3$ FBMC-QAM has 0.5dB and 1dB SNR loss compared to the benchmark CP-OFDM for EVA and ETU, respectively. Furthermore, it can be observed from Fig. 4.10 and Fig. 4.12 that the error floor encountered in the uncoded FBMC-QAM in Chapter 3 can be completely removed after a few IIC iterations. This shows that the intrinsic interference in FBMC-QAM can be cancelled effectively with a combination of BICM-ID and IIC.

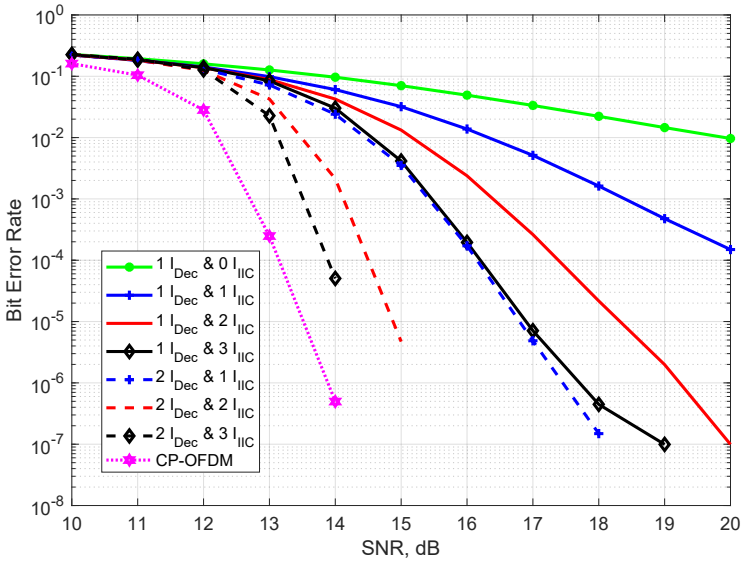

Fig. 4.12 BER performance of the proposed IIC-based BICM-ID receiver for FBMC-QAM and CP-OFDM over ETU channel

4.5.5 EXIT Chart Performance of Multiple Fading Channel Realizations

The above BER and EXIT curves have been shown for specific instances of the respective random fading channels. This is because EXIT charts are defined for fading channels only if very long codes and a channel that changes with the symbol rate are considered. For multiple random instances of a frequency-selective channel, each realization will produce a different inner decoder EXIT curve. In order to generalize the use of EXIT chart in random fading channels, a model that allows an outage probability of $\rho\%$ in the EXIT chart analysis is investigated [3]. That is, considering a $\rho\%$ outage probability line on the EXIT curve, its convergence behaviour is expected to be satisfied by $(1-\rho)\%$ of the channel instances. As an example, the inner decoder EXIT curves for 50 random realizations of the EVA channel at SNR of 17dB is depicted in Fig. 4.13. The black (solid) lines represent the inner decoder EXIT curves for the individual realizations. Different levels of outage probability are also represented on Fig. 4.13. Note for instance the MI of the 90th percentile line. It is expected that this MI can be achieved by 90% of the random fading channels (45 out of 50 in this case), with the remaining 10% in outage. Furthermore, if a tunnel exists between the 90th percentile line and the outer decoder EXIT curve, the decoding iterations will converge for 90% of channel instances.

Fig. 4.14 and Fig. 4.15 show the EXIT chart and BER performance, respectively, of the proposed IIC-based BICM-ID receiver over 1000 realizations of the EVA channel, assuming 10% outage probability. This means that, 900 of the resulting inner decoder EXIT curves must satisfy the properties of the EXIT curve in Fig. 4.14. Notice that the inner decoder EXIT curve at 16dB intersects with the outer decoder EXIT curve using $\mathbb{I}_{Dec} = 1$. This implies that the tunnel between the two curves is blocked and therefore increasing the number of IIC iteration will not improve BER performance. By

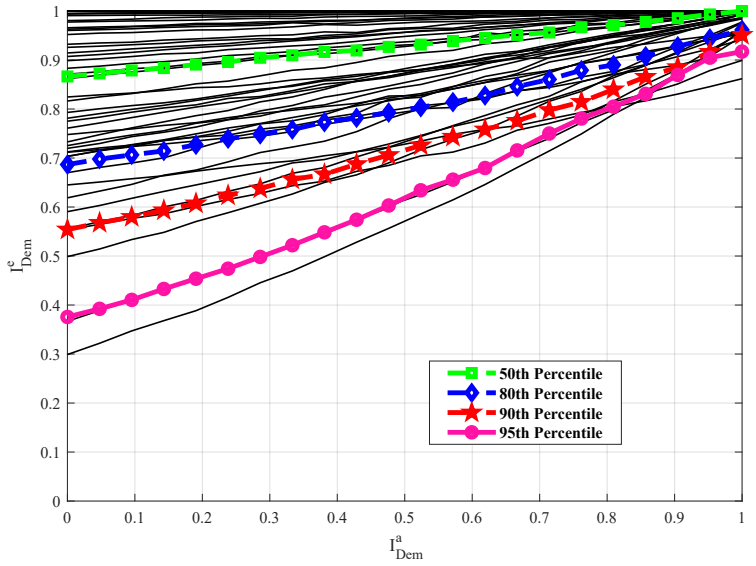

Fig. 4.13 Inner decoder EXIT curves for 50 random realizations of EVA channel showing different levels of outage probability.

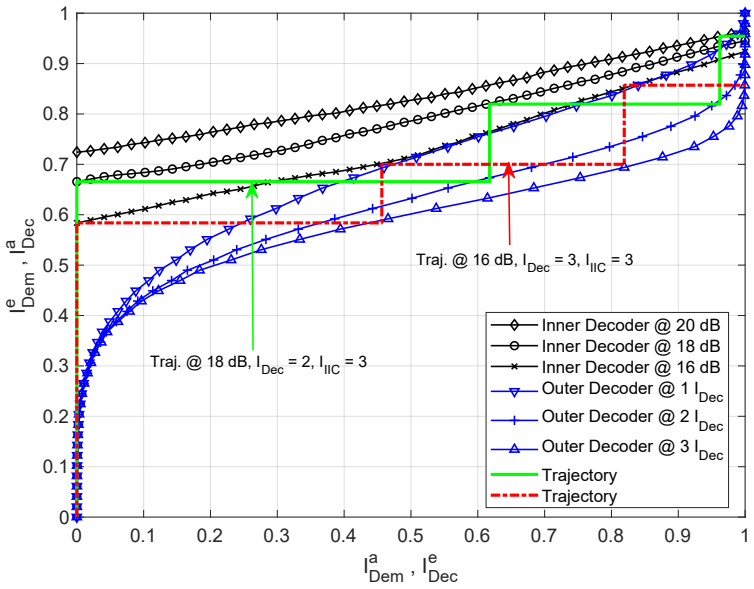

Fig. 4.14 EXIT function and decoding trajectories of the proposed receiver with 10% outage probability over multiple realizations of EVA channel

increasing $\mathbb{I}_{Dec}$ to 2 and SNR to 18dB, a tunnel is created between the two EXIT curves as shown by the green trajectory line in Fig. 4.14. This translates to a significant improvement in BER performance as shown in Fig. 4.15. Note that, in this case, the BER performance in Fig. 4.15 will be achieved for 90% of channel instances. Different levels of outage performance may be tolerated depending on the system requirements.

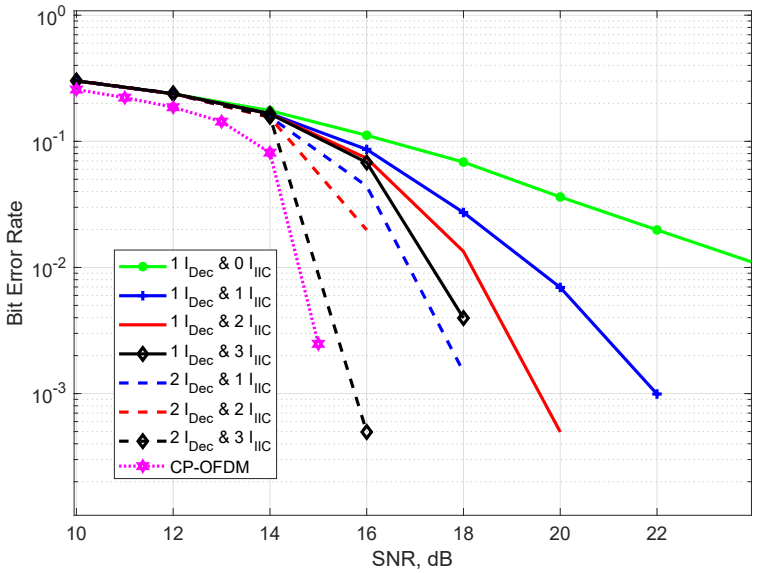

Fig. 4.15 BER performance of the proposed receiver for FBMC-QAM and CP-OFDM with 10% outage probability over multiple realizations of EVA channel

4.6 Summary

In this chapter, a coded FBMC-QAM system has been studied to remove the error floor encountered in the uncoded FBMC-QAM case investigated in Chapter 3. The key issue with FBMC-QAM is the high intrinsic interference caused by the loss of complex orthogonality between subcarriers. To address the interference problem, an IIC-based BICM-ID receiver is proposed and analysed for FBMC-QAM systems. Furthermore, the convergence behaviour of the proposed receiver is studied using EXIT chart analysis. Based on the EXIT chart analysis, the number of iterations of the BICM-ID receiver required to achieve a target BER performance and the corresponding complexity is predicted. The results show that the IIC-based BICM-ID receiver can remove the intrinsic interference in FBMC-QAM systems under time-varying channels with an increase in computational complexity compared to CP-OFDM. For example, in the case of the EPA channel, FBMC-QAM with IIC requires about 15 times more complexity (due to the inner modulator/demodulator) than in a benchmark CP-OFDM system with no IIC. However, the EXIT chart analysis can be used to minimise complexity for a given system by choosing the optimum number of inner and outer iterations. Also, there is the potential for a hybrid receiver that bypasses the FBMC-QAM modulator/demodulator after the initial IIC iteration to be used as a low complexity implementation of the proposed receiver. In summary, the proposed receiver is capable of effectively addressing the intrinsic interference problem in FBMC-QAM. This will enable the practical implementation of FBMC-QAM in asynchronous applications due to its ultra-low OOB emission, which causes very low leakage interference between asynchronous users. In Chapter 5, the possibility of exploiting the intrinsic interference in FBMC-QAM as a useful signal for wireless energy harvesting will be investigated. Also, in Chapter 6 the BICM-ID receiver with interference

cancellation will be employed to remove the interference in a multi-user multiple access channel considering both single and mixed numerologies systems.

Chapter 5

Multi-User Wireless Information and Power Transfer in FBMC-Based IoT Networks

5.1 Introduction

In Chapters 3 and 4, IIC-based receivers are investigated to address the intrinsic interference problem in FBMC-QAM systems, which is treated as an undesired signal. However, apart from the need for efficient information reception, it is essential for future wireless networks to be self-sustaining [138]. Recently, SWIPT has been recognized as a promising approach to provide device self-sustainability and prolong the battery life of energy-constrained wireless nodes [21, 106]. Unlike traditional wireless communication networks in which interference signals are undesirable, SWIPT systems are capable of exploiting interference signals as a source of wireless power [139].

The purpose of this chapter is to investigate ways in which the intrinsic interference in FBMC-QAM systems can be exploited as a useful signal. Motivated by the advantages of FBMC-QAM systems over conventional OFDM, this chapter focuses on the combination of FBMC-QAM and SWIPT for future wireless applications. By harnessing the benefits of FBMC-QAM and SWIPT, energy constrained wireless devices can be effectively connected and powered anywhere, any time. Specifically, a multi-user FBMC-based system is considered in this chapter, in which a single antenna BS transmits signals to multiple UNs in the DL and receives signals from the UNs in the UL. Each UN can decode information and harvest energy from the received signal. Moreover, a non-linear EH model, which is more practical, is adopted in this chapter. In order to remove the intrinsic interference in FBMC-QAM, an IIC receiver is employed for the information decoding at both the BS and UN [130, 140, 141]. A weighted sum-rate (WSR) maximization problem is formulated with the aim of optimizing the weight allocation, time allocation, and power allocation of each UN under the total DL transmit power and EH constraints. To effectively solve the WSR problem, it is converted to

an equivalent WMMSE problem, which is then converted to two subproblems: (i) time and weight allocation problem and (ii) power allocation problem.

The remainder of this chapter is organized as follows: In Section 5.2, the proposed FBMC-based SWIPT system model and the problem formulation are described. The optimization solutions and algorithms are presented in Section 5.3. The performance and complexity analysis of the proposed FBMC-based SWIPT model are presented in Section 5.4. Finally, a summary of this chapter is provided in Section 5.5.

5.2 System Model and Problem Formulation

In this section, the details of the proposed multi-user FBMC-based SWIPT system is discussed. The proposed system, shown in Fig. 5.1, consists of a single antenna BS and K UNs. Each UN has two antennas: one dedicated to information reception and transmission, and the other dedicated to energy reception. The UNs are scheduled to transmit and receive via TDMA. Note that a single antenna is employed at the BS for analytical tractability and to focus mainly on the performance of SWIPT in FBMC systems. Moreover, the proposed system can be a special case of a distributed or cell-free MIMO system in which multiple single antenna access points cooperate to serve multiple UNs. For such a system, the proposed model studies the transmission between one access point and multiple UNs.

5.2.1 Downlink Phase

In the DL phase, each UN decodes information from its desired signal while exploiting the intrinsic interference and multi-user interference for EH. The system model for EH and ID is shown in Fig. 5.1. Recall from Chapter 3 that, in FBMC systems, data on even-numbered subcarriers causes negligible interference to other even-numbered subcarriers [129]. This is because FBMC systems employ prototype filters that are well-localized in the frequency domain which limits OOB leakage to adjacent subcarriers. Therefore, in order to reduce the level of intrinsic interference at the information receiver of each UN, QAM modulated data is inserted only on even-numbered subcarriers in the DL. With reduced interference at the UN, the complexity and power consumption of the information receiver can also be reduced. Under this setup, the n-th transmitted symbol vector from the BS to the k-th UN during its assigned time slot τ_k is given as

$$\mathbf{x}_{n,k}^{dl} = \mathbf{G}_{n,k}\Phi\mathbf{a}_{n,k}^{dl} \tag{5.1}$$

where $\mathbf{x}_{n,k}^{dl} = [x_{0,n}^{k}, x_{1,n}^{k}, \ldots, x_{L_p-1,n}^{k}]$ is the vector of the transmitted signal, $L_p = D \times M$ with D as the overlapping factor of the prototype filter, Φ is the $M \times M$ IFFT matrix with entries on the i-th row and j-th column given as $\sqrt{1/M}\exp(\sqrt{-1}\frac{2\pi ij}{M})$, M is the total number of subcarriers and $\mathbf{a}_{n,k}^{dl}$ represents

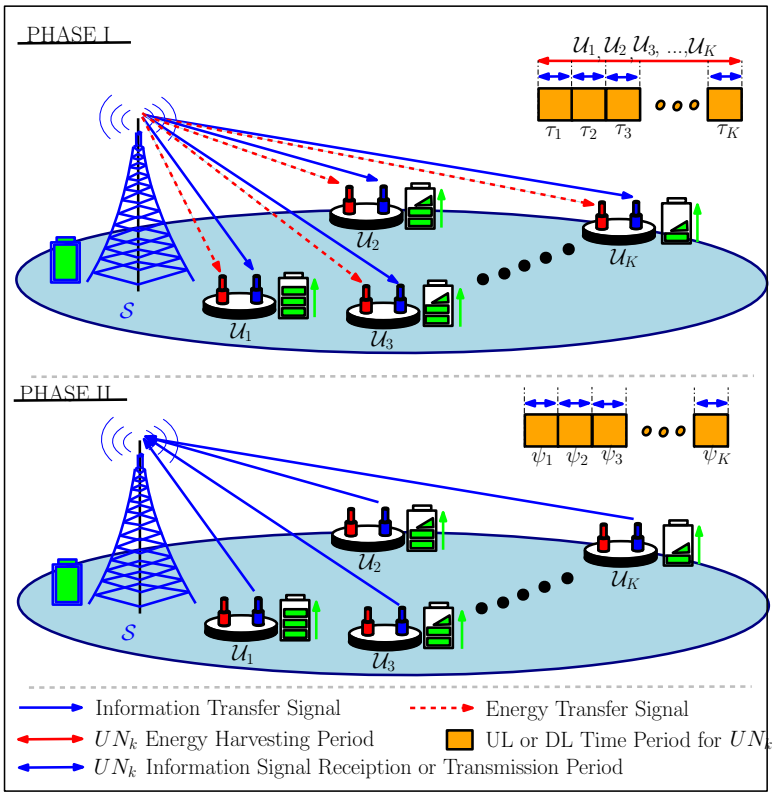

Fig. 5.1 Multi-user FBMC-QAM system model with separate antenna SWIPT architecture.

the vector of transmitted data, given as

$$\mathbf{a}_{n,k}^{dl} = \begin{cases} a_{n,m}^{e,dl}, & \text{for } m \in \{0,2,\ldots,M-2\} \\ 0, & \text{for } m \in \{1,3,\ldots,M-1\} \end{cases} \tag{5.2}$$

$\mathbf{G}_{n,k}$ represents the $L_p \times M$ prototype filter matrix whose entry on the l-th diagonal is given as

$$g_{n,k}[l] = g[l - nM] \tag{5.3}$$

where $g[i]$ is the prototype filter coefficient [129]. As in Chapter 3 and Chapter 4, the PHYDYAS prototype filter is used for the per subcarrier filtering in this chapter [11].

5.2.1.1 Information Receiver

At the information receiver, the received signal is first filtered, down-sampled and then passed through the FFT block. The resulting signal after the filtering operation is represented as

$$\begin{aligned}\mathbf{y}_{n,k}^{ID,dl} &= \mathbf{G}_{n,k}^{H}\mathbf{H}_{k}^{dl}\mathbf{x}_{n,k}^{dl} + \mathbf{G}_{n,k}^{H}\mathbf{z}_{k}^{dl} \\ &= \mathbf{G}_{n,k}^{H}\mathbf{H}_{k}^{dl}\mathbf{G}_{n,k}\Phi\mathbf{a}_{n,k}^{dl} + \mathbf{G}_{n,k}^{H}\mathbf{z}_{k}^{dl} \\ &= \tilde{\mathbf{H}}_{k}^{dl}\mathbf{a}_{n,k}^{dl} + \mathbf{G}_{n,k}^{H}\mathbf{z}_{k}^{dl}\end{aligned} \tag{5.4}$$

where $\tilde{\mathbf{H}}_{k}^{dl} = \mathbf{G}_{n,k}^{H}\mathbf{H}_{k}^{dl}\mathbf{G}_{n,k}\Phi$, $\mathbf{z}_{k}^{dl}$ is the $L_p \times 1$ AWGN vector at UN_k and $\mathbf{H}_{k}^{dl}$ is the $L_p \times L_p$ multipath fading channel matrix between the BS and UN_k. The entry on the l-th diagonal of $\mathbf{H}_{k}^{dl}$ represents the complex channel gain of the l-th subchannel of UN_k and can be modelled as [110]

$$h_{k,l} = \sqrt{A}\left(\frac{\tilde{d}}{d_k}\right)^{\frac{\kappa}{2}}\sqrt{\mathrm{g}_t\mathrm{g}_r}\exp\left(j2\pi\frac{d_k}{\lambda}\right) \tag{5.5}$$

where d_k is the distance between the BS and UN_k, $\tilde{d}$ is the reference distance for the path loss, A is the attenuation at the reference distance, κ is the path loss exponent, g_t is the BS antenna gain and g_r is the UN antenna gain. Also, λ represents the wavelength of the RF signal with frequency f_c. The frequency domain signal vector after down-sampling and FFT is given as

$$\begin{aligned}\mathbf{y}_{n,k}^{dl} &= \Phi^{H}\mathbf{y}_{n,k}^{ID,dl} \\ &= \Phi^{H}\tilde{\mathbf{H}}_{k}^{dl}\mathbf{a}_{n,k}^{dl} + \Phi^{H}\mathbf{G}_{n,k}^{H}\mathbf{z}_{k}^{dl} \\ &= \hat{\mathbf{H}}_{k}^{dl}\mathbf{a}_{n,k}^{dl} + \tilde{\mathbf{z}}_{k}^{dl}\end{aligned} \tag{5.6}$$

where $\hat{\mathbf{H}}_{k}^{dl} = \Phi^{H}\tilde{\mathbf{H}}_{k}^{dl}$ is the $M \times M$ down-sampled effective channel matrix and $\tilde{\mathbf{z}}_{k}^{dl} = \Phi^{H}\mathbf{G}_{n,k}^{H}\mathbf{z}_{k}^{dl}$ is the $M \times 1$ effective noise vector. As mentioned above, modulated data is inserted only on even-numbered subcarriers in the DL phase. Therefore, the sampled received signal on even-numbered subcarriers of the k-th UN can be expressed as

$$\mathbf{y}_{n,k}^{e,dl} = \hat{\mathbf{H}}_{k}^{e,dl}\mathbf{a}_{n,k}^{e,dl} + \tilde{\mathbf{z}}_{k}^{dl}, \tag{5.7}$$

where $\mathbf{a}_{n,k}^{e,dl} = [a_{n,0}^{e,dl}, a_{n,2}^{e,dl}, \ldots, a_{n,M-2}^{e,dl}]$ represents the data on even-numbered subcarriers and $\hat{\mathbf{H}}_{k}^{e,dl}$ is the corresponding $M/2 \times M/2$ effective channel matrix. By getting rid of the odd-numbered subcarriers, it can be assumed that there is negligible ICI between subcarriers due to the low OOB emission performance of FBMC. This implies that UN_k is only affected by ISI. Thus, the even-numbered demodulated signal associated to the m-th subcarrier and the n-th symbol for UN_k is given as

$$r_{m,n,k}^{dl} = \hat{h}_{m,n,k}^{e,dl}a_{m,n}^{e,dl} + \underbrace{\sum_{n'\neq n}\sum_{m'=0}^{M}\hat{h}_{m',n',k}^{e,dl}a_{m',n'}^{e,dl}}_{I_{ISI}^{dl}} + \tilde{z}_{k}^{dl}. \tag{5.8}$$

where $\hat{h}^{e,dl}_{m,n,k}$ is the m-th diagonal element of $\hat{\mathbf{H}}^{e,dl}_{k}$.

To eliminate the ISI term in (5.8), an IIC receiver, similar to the one used in Chapter 3, is implemented as shown in Algorithm 3. Without loss of generality, it is assumed that the receiver undergoes enough IIC iterations to completely remove the ISI term in (5.8). This assumption has been made in order to obtain insight regarding the optimization of the resource allocation in the EH and ID of the proposed scheme. Moreover, with the reduced intrinsic interference at the UN, fewer number of IIC iterations are required to remove the ISI term in (5.8). As shown in Chapter 4, the IIC algorithm is capable of removing the intrinsic interference with a few iterations. Thus, the demodulated signal after the last IIC iteration can be expressed as

$$\hat{r}^{dl}_{m,n,k} = \hat{h}^{dl}_{m,n,k} a^{e,dl}_{m,n,k} + \tilde{z}^{dl}_{k}. \tag{5.9}$$

The effective SNR of UN_k is calculated as the ratio of the signal power and the effective noise power. From (5.9), the power of the processed noise can be calculated as

$$\begin{aligned} \mathbb{E}[(\tilde{\mathbf{z}}^{dl}_{n,k})(\tilde{\mathbf{z}}^{dl}_{n,k})^H] &= \mathbb{E}[\mathbf{\Phi}^H \mathbf{G}^H_{n,k} (\mathbf{z}^{dl}_{k})(\mathbf{z}^{dl}_{k})^H \mathbf{G}_{n,k} \mathbf{\Phi}] \\ &= \mathbf{G}^H_{n,k} \mathbb{E}[(\mathbf{z}^{dl}_{k})(\mathbf{z}^{dl}_{k})^H] \mathbf{G}_{n,k} \\ &= \mathbf{G} \sigma^2_{z^{dl}_{k}} \end{aligned} \tag{5.10}$$

where $\mathbf{G} = \mathbf{G}^H_{n,k} \mathbf{G}_{n,k}$ and $\sigma^2_{z^{dl}_{k}}$ represents the noise variance. Therefore, for the n-th symbol and m-th subcarrier of UN_k the effective noise power, $\sigma^2_k = g_{m,n,k} \sigma^2_{z^{dl}_{k}}$, is Gaussian. The corresponding SNR for UN_k is defined as

$$SNR^{dl}_{m,n,k} = \frac{|\hat{h}^{dl}_{m,n,k}|^2 P^{dl}_{m,n,k}}{\sigma^2_k}, \tag{5.11}$$

where $P^{dl}_{m,n,k}$ is the power allocated to UN_k in the DL. Therefore, the DL data rate of UN_k for the time period τ_k is given by

$$R^{dl}_{k} = \alpha \tau_k T \sum_{n=1}^{N} \sum_{m=1}^{M} \log_2(1 + SNR^{dl}_{m,n,k}). \tag{5.12}$$

where N is the total number of FBMC-QAM symbols, T denote the total transmission time, and α is the time allocated for DL communication.

5.2.1.2 Energy Receiver

As mentioned above, each UN is equipped with a separate antenna for EH, which implies that each UN can harvest energy from all sub-carriers in every DL time slot. At the EH receiver, the contribution of noise is assumed to be negligible. Therefore, the received signal at the EH receiver of UN_k is given

as

$$\begin{aligned}\mathbf{y}_{n,k}^{EH,dl} &= \mathbf{H}_k^{dl}\mathbf{x}_{n,k}^{dl} \\ &= \mathbf{H}_k^{dl}\mathbf{G}_{n,k}\Phi\mathbf{a}_{n,k}^{dl} \\ &= \bar{\mathbf{H}}_k^{dl}\mathbf{a}_{n,k}^{dl}\end{aligned} \tag{5.13}$$

where $\bar{\mathbf{H}}_k^{dl} = \mathbf{H}_k^{dl}\mathbf{G}_{n,k}\Phi$. Considering the linear EH model, the total harvested power by UN_k is given as

$$\begin{aligned}P_k^{linear} &= \frac{\alpha\beta_k}{(1-\alpha)\psi_k}\sum_{j=1}^{K}\tau_j\sum_{n=1}^{N}\sum_{m=1}^{M}|\bar{h}_{m,n,j}^{dl}|^2 P_{m,n,j}^{dl} \\ &= \frac{\alpha\beta_k}{(1-\alpha)\psi_k}\gamma_{m,n,j}^{dl}\end{aligned} \tag{5.14}$$

where β_k denotes the energy conversion efficiency in the linear region of the EH circuit, ψ_k is the UL transmission time of UN_k, $\bar{h}_{m,n,j}$ represents the diagonal entries of $\bar{\mathbf{H}}_k^{dl}$ and

$$\gamma_{m,n,j}^{dl} = \sum_{j=1}^{K}\tau_j\sum_{n=1}^{N}\sum_{m=1}^{M}|\bar{h}_{m,n,j}^{dl}|^2 P_{m,n,j}^{dl}. \tag{5.15}$$

The linear EH model is employed in the literature due to its relatively simple implementation. However, it does not capture the non-linear behaviour of the EH circuit. To tackle the problem with the linear EH model, the practical EH model in [126] and [142], which uses a non-linear function to model the harvested power, is considered in this chapter. By adopting this model, the non-linear harvested power of UN_k can be expressed as

$$P_k = \begin{cases}\Delta_k\gamma_{m,n,j}^{dl}, & \text{for } \gamma_{m,n,j}^{dl} \leq P_{th} \\ \Delta_k P_{th}, & \gamma_{m,n,j}^{dl} > P_{th}\end{cases} \tag{5.16}$$

where $\Delta_k = \frac{\alpha\beta_k}{(1-\alpha)\psi_k}$ and P_{th} is the saturation threshold power of the EH receiver. During the UL time slot of UN_k, ψ_k, the UL transmit power is $P_k^{ul} = P_k$. Furthermore, each UN is capable of harvesting energy during all time slots due to their dedicated energy antenna. The energy harvested in other time slots is stored in a battery and the information receiver draws power from the battery for its processing, e.g. IIC algorithm. While the additional processing required for IIC may consume some of the power harvested, there are many applications where the DL data required to be detected at a UN is very small, and hence negligible compared to the total energy harvested.

5.2.2 Uplink Phase

Now, consider the multiple access UL communication between the BS and UNs. Since the BS has a higher processing capacity, it is assumed that modulated data is transmitted on both even and odd subcarriers in the UL. This is a practical assumption because in most mMTC applications UNs will collect data and transmit to a BS, resulting in a higher data rate requirement on the UL compared to

the DL. During time slot ψ_k, the n-th transmit symbol vector of UN_k is given as

$$\mathbf{x}_{n,k}^{ul} = \mathbf{G}_{n,k}\Phi\mathbf{a}_{n,k}^{ul} \tag{5.17}$$

Similar to the DL phase, the received signal at the BS is filtered, down-sampled and converted to the frequency domain using the FFT operation. The signal at the output of the receive filter is expressed as

$$\begin{aligned}\mathbf{y}_{n,k}^{ID,ul} &= \mathbf{G}_{n,k}^H\mathbf{H}_k^{ul}\mathbf{x}_{n,k}^{ul} + \mathbf{G}_{n,k}^H\mathbf{z}^{ul} \\ &= \mathbf{G}_{n,k}^H\mathbf{H}_k^{ul}\mathbf{G}_{n,k}\Phi\mathbf{a}_{n,k}^{ul} + \mathbf{G}_{n,k}^H\mathbf{z}^{ul} \\ &= \tilde{\mathbf{H}}_k^{ul}\mathbf{a}_{n,k}^{ul} + \mathbf{G}_{n,k}^H\mathbf{z}^{ul}.\end{aligned} \tag{5.18}$$

where $\tilde{\mathbf{H}}_k^{ul} = \mathbf{G}_{n,k}^H\mathbf{H}_k^{ul}\mathbf{G}_{n,k}\Phi$, $\mathbf{z}^{ul}$ is the $L_p \times 1$ AWGN vector and $\mathbf{H}_k^{ul}$ is the $L_p \times L_p$ multipath fading channel matrix between UN_k and the BS. After down-sampling and FFT, the frequency domain signal vector for UN_k is given as

$$\begin{aligned}\mathbf{y}_{n,k}^{ul} &= \Phi^H\mathbf{y}_{n,k}^{ID,ul} \\ &= \Phi^H\tilde{\mathbf{H}}_k^{ul}\mathbf{a}_{n,k}^{ul} + \Phi^H\mathbf{G}_{n,k}^H\mathbf{z}^{ul} \\ &= \hat{\mathbf{H}}_k^{ul}\mathbf{a}_{n,k}^{ul} + \tilde{\mathbf{z}}^{ul}\end{aligned} \tag{5.19}$$

where $\hat{\mathbf{H}}_k^{ul} = \Phi^H\tilde{\mathbf{H}}_k^{ul}$ and $\tilde{\mathbf{z}}^{ul} = \Phi^H\mathbf{G}_{n,k}^H\mathbf{z}^{ul}$. Note that, unlike the UNs, the BS suffer from both ICI and ISI. Therefore, the demodulated signal associated with the m-th subcarrier and the n-th symbol of UN_k is given as

$$r_{m,n,k}^{ul} = \hat{h}_{m,n,k}^{ul}a_{m,n}^{ul} + \underbrace{\sum_{n'\neq n}\sum_{m'=0}^{M}\hat{h}_{m',n',k}^{ul}a_{m',n'}^{ul}}_{I_{ISI}^{ul}} + \underbrace{\sum_{m'\neq m}\hat{h}_{m',n,k}^{ul}a_{m',n}^{ul}}_{I_{ICI}^{ul}} + \tilde{z}^{ul} \tag{5.20}$$

where $\hat{h}_{m,n,k}^{ul}$ is the m-th diagonal element of $\hat{\mathbf{H}}_k^{ul}$. As in the DL case, the ICI and ISI terms are estimated and removed by applying a fixed number of IIC iterations at the BS. Assuming perfect cancellation of the intrinsic interference after IIC, the resulting processed signal is given as

$$\hat{r}_{m,n,k}^{ul} = \hat{h}_{m,n,k}^{ul}a_{m,n,k}^{ul} + \tilde{z}^{ul}. \tag{5.21}$$

The effective noise power, σ^2, is calculated as shown in (5.10). Thus, the SNR and rate at the BS from the received signal of UN_k can be represented respectively as

$$SNR_{m,n,k}^{ul} = \frac{|\hat{h}_{m,n,k}^{ul}|^2P_{m,n,k}^{ul}}{\sigma^2} \quad \text{and} \tag{5.22}$$

$$R_k^{ul} = (1-\alpha)\psi_k T\sum_{n=1}^{N}\sum_{m=1}^{M}\log_2(1+SNR_{m,n,k}^{ul}), \tag{5.23}$$

respectively.

5.2.3 Problem Formulation

Consider the fact that, at each transmit node (UNs or BS), a maximum power threshold is set on the transmit power and that each node's transmission is restricted to its allocated time slot. Under these constraints, an UL-DL WSR maximization problem is investigated to optimize the WSR of each UN. Mathematically, the UL-DL WSR maximization problem for the proposed FBMC-based SWIPT system is formulated as

$$\begin{aligned} P(1): \underset{L_g}{\text{maximize}} \quad & \sum_{k=1}^{K} \left[\omega_k^{dl} R_k^{dl} + \omega_k^{ul} R_k^{ul} \right] \\ \text{subject to} \quad & \sum_{m=1}^{M} \sum_{n=1}^{N} P_{m,n,k}^{dl} \leq P_{0,max}^{dl}, \\ & \omega_k^{dl} \geq 0, \\ & \sum_{m=1}^{M} \sum_{n=1}^{N} P_{m,n,k}^{ul} \leq P_k^{ul} - P_c, \\ & \omega_k^{ul} \geq 0, \\ & \alpha \sum_{k=1}^{K} \tau_k + (1-\alpha) \sum_{k=1}^{K} \psi_k = T, \end{aligned} \tag{5.24}$$

where $L_g = [\alpha, \{P_{m,n,k}^{dl}\}, \{P_{m,n,k}^{ul}\}, \{\psi_k\}, \{\tau_k\}, \{\omega_k^{dl}\}, \{\omega_k^{ul}\}]$, $P_{0,max}^{dl}$ is the maximum transmit power at the BS and P_c is the power consumed by UN_k for information processing. Also, ω_k^{dl} and ω_k^{ul} are the DL and UL weights for UN_k. To reduce the complexity involved in solving problem $P(1)$, it is converted to an equivalent WMMSE minimization problem [22]. The WSR to WMMSE conversion steps are presented in Appendix B.1. The WMMSE problem is expressed as

$$\begin{aligned} P(2): \underset{L_g}{\text{minimize}} \quad & \sum_{k=1}^{K} \sum_{n=1}^{N} \sum_{m=1}^{M} \left[\bar{\omega}_k^{dl} e_{m,n,k}^{dl} + \bar{\omega}_k^{ul} e_{m,n,k}^{ul} \right] \\ \text{subject to} \quad & \sum_{n=1}^{N} \sum_{m=1}^{M} P_{m,n,k}^{dl} \leq P_{0,max}^{dl}, \\ & \bar{\omega}_k^{dl} \geq 0, \\ & \sum_{k=1}^{K} \sum_{n=1}^{N} \sum_{m=1}^{M} P_{m,n,k}^{ul} \leq P_k^{ul} - P_c, \\ & \bar{\omega}_k^{ul} \geq 0, \\ & \alpha \sum_{k=1}^{K} \tau_k + (1-\alpha) \sum_{k=1}^{K} \psi_k = T, \end{aligned} \tag{5.25}$$

where $\bar{\omega}_k^{dl}$ and $\bar{\omega}_k^{ul}$ are the WMMSE weights for UN_k on the DL and UL, respectively. Also,

$$e_{m,n,k}^{dl} = \frac{\sigma_{z^{dl}}^2}{|\hat{h}_{m,n,k}^{dl}|^2 P_{m,n,k}^{dl} + \sigma_k^2} \tag{5.26}$$

and

$$e_{m,n,k}^{ul} = \frac{\sigma_{z^{ul}}^2}{|\hat{h}_{m,n,k}^{ul}|^2 P_{m,n,k}^{ul} + \sigma^2} \tag{5.27}$$

represent the MMSE for the DL and UL of UN_k (see Appendix B.1). Problem $P(2)$ can be split into the time and weight resource (TRS) allocation problem and the power resource (PRS) allocation problem as shown in Appendix B.1. This is expressed as

$$\begin{aligned} \underset{\alpha,\{\psi_k\},\{\tau_k\},\omega_k^{dl},\omega_k^{ul}}{\text{minimize}} \quad & T_{RS} \\ \text{subject to} \quad & \alpha \sum_{k=1}^{K} \tau_k + (1-\alpha) \sum_{k=1}^{K} \psi_k = T, \\ & \omega_k^{ul} \geq 0, \\ & \sum_{n=1}^{N} \sum_{m=1}^{M} P_{m,n,k}^{ul} \leq P_k^{ul} - P_c, \\ & \omega_k^{dl} \geq 0 \end{aligned} \tag{5.28}$$

and

$$\begin{aligned} \underset{\{P_{m,n,k}^{dl}\},\{P_{m,n,k}^{ul}\}}{\text{minimize}} \quad & P_{RS} \\ \text{subject to} \quad & \sum_{k=1}^{K} \sum_{n=1}^{N} \sum_{m=1}^{M} P_{m,n,k}^{dl} \leq P_{0,max}^{dl} \\ & \sum_{n=1}^{N} \sum_{m=1}^{M} P_{m,n,k}^{ul} \leq P_k^{ul} - P_c, \end{aligned} \tag{5.29}$$

respectively. Here, T_{RS} and P_{RS} are defined as

$$T_{RS} = \frac{MN}{2} \sum_{k=1}^{K} [x_k - \log_2(x_k)] + MN \sum_{k=1}^{K} [z_k - \log_2(z_k)] \tag{5.30}$$

and

$$P_{RS} = \sum_{k=1}^{K} \sum_{n=1}^{N} \sum_{m=1}^{M} \log_2 \Big(\frac{\sigma_k^2}{|\hat{h}_{m,n,k}^{dl}|^2 P_{m,n,k}^{dl} + \sigma_k^2} \Big) + \sum_{k=1}^{K} \sum_{n=1}^{N} \sum_{m=1}^{M} \log_2 \Big(\frac{\sigma^2}{|\hat{h}_{m,n,k}^{ul}|^2 P_{m,n,k}^{ul} + \sigma^2} \Big). \tag{5.31}$$

where $x_k = \frac{\alpha \tau_k \omega_k^{dl} T}{\log(2)}$ and $z_k = \frac{(1-\alpha)\psi_k \omega_k^{ul} T}{\log(2)}$.

Algorithm 3 IIC Algorithm

Set the maximum number of IIC iterations, I_{max}
Initialize iteration counter $i = 0$
while $i \leq I_{max}$ **do**
  if DL Communication **then**
    Estimate I_{ISI}^{dl} as described in Section 5.3.1
    Subtract the estimated term from (5.8), i.e.
    $\hat{r}_{n,k}^{dl}(i+1) = \hat{r}_{n,k}^{dl}(i) - \hat{I}_{ISI}^{e,dl}$, let $i = i+1$
  else
    Estimate I_{ICI}^{ul} and I_{ISI}^{ul} as described in Section 5.3.1
    Subtract the estimated terms from (5.20), i.e.
    $\hat{r}_{n,k}^{ul}(i+1) = \hat{r}_{n,k}^{ul}(i) - \hat{I}_{ICI}^{ul} - \hat{I}_{ISI}^{ul}$
  end if
  $i = i+1$
end while
Terminate

5.3 Interference Cancellation and Optimization Solutions

In this section, the IIC algorithm and the detailed solution for WMMSE problem, $P(2)$, are presented. The optimized parameters obtained from solving $P(2)$ are used in a joint resource allocation algorithm to solve $P(1)$.

5.3.1 Iterative Interference Cancellation

In this subsection, the IIC algorithm employed in this chapter is presented. As mentioned in Chapter 2, FBMC systems achieve improved frequency confinement compared to OFDM. However, this comes with the loss of complex orthogonality between subcarriers, resulting in high intrinsic interference. Similar to Chapters 3 and 4, the interference terms in (5.8) and (5.20) are removed using an IIC receiver. Notice from (5.8) and (5.20) that the interference terms are determined by the type of prototype filter, FFT/IFFT, and the fading channel effect. Unless a different prototype filter is selected, the interference terms vary mainly with the fading channel. After the initial decoding iteration, the receiver node (UN or BS), estimates the multipath channel responses ($\mathbf{H}_k^{dl}$ and $\mathbf{H}_k^{ul}$) and compute the effective channel matrices $\hat{\mathbf{H}}_k^{dl}$ and $\hat{\mathbf{H}}_k^{ul}$ using the filter response matrix $\mathbf{G}_{n,k}$ and the IFFT matrix Φ. In each iteration, the detected signal is remodulated to obtain estimates of the transmitted data symbols ($\mathbf{a}_{n,k}^{dl}$ or $\mathbf{a}_{n,k}^{ul}$). To obtain the ICI term in (5.20) the current estimated data symbol is multiplied by the estimated channel and filter responses. On the other hand, the ISI terms in (5.8) and (5.20) are obtained by multiplying the previous estimated data symbols by the estimated channel and filter responses. The calculated ICI and ISI terms are then subtracted from the received signal in order to achieve a better version of the demodulated signal in the next iteration. Details of the IIC receiver is shown in Algorithm 3.

5.3.2 Optimal Resource Allocation (ORA)

The scheme for solving problem $P(1)$ is presented in this subsection. As shown in the previous section, $P(1)$ can be converted to a WMMSE problem, $P(2)$, which is further split into the TRS and PRS allocation problems. The solutions for the TRS and PRS problems are presented as follows:

5.3.2.1 TRS Optimization

The solution for the TRS allocation problem is presented in Theorem 1.

Theorem 1. *The optimal time and weight allocation for the WSR maximization problem is equal time and weights allocation, that is,* $\tau_1 = \ldots = \tau_K, \psi_1 = \ldots = \psi_K$ *and* $\omega_1^{dl} = \ldots = \omega_K^{dl}, \omega_1^{ul} = \ldots = \omega_K^{ul}$. *Hence,* $\alpha = 1/2$, $\tau_k = 1/K$, $\psi_k = 1/K$ *and* $\omega_k^{dl} = \omega_k^{ul} = \frac{2Kx^\star \log(2)}{T^2}$, *where* $x^\star$ *is the minimum value of the function* $f(x) : min[x - \log_2(x)]$.

Proof. See Appendix B.3 □

5.3.2.2 PRS Optimization

The closed-form solutions for $P_{m,n,k}^{dl}$ and $P_{m,n,k}^{ul}$ are derived by differentiating the Lagrangian of (5.29) with respect to $P_{m,n,k}^{dl}$ and $P_{m,n,k}^{ul}$, respectively, and equating the differential to zero. Thus, the optimal DL and UL power allocation for UN_k can be expressed as

$$P_{m,n,k}^{dl\star} = \Big[\frac{1}{\log(2)A} - \frac{\sigma_k^2}{|\hat{h}_{m,n,k}^{dl}|^2}\Big] \tag{5.32}$$

and

$$P_{m,n,k}^{ul\star} = \Big[\frac{1}{\lambda_k^{ul\star}\log(2)} - \frac{\sigma^2}{|\hat{h}_{m,n,k}^{ul}|^2}\Big], \tag{5.33}$$

with $A = (\lambda^{dl\star} - \tau_k \sum_{n=1}^{N}\sum_{m=1}^{M}|\hat{h}_{m,n,k}^{dl}|^2 \sum_{j=1}^{K}\frac{\alpha\beta_j\lambda_j^{ul}}{(1-\alpha)\psi_j})$. Note that $\lambda^{dl\star}$ can be found using the bisection method and $\lambda_k^{ul\star}$ is given as

$$\lambda_k^{ul\star} = \frac{MN}{\log(2)\Big(B - P_c + \sum_{m=1}^{M}\frac{N\sigma_{z^{ul}}^2}{|\hat{h}_{m,n,k}^{ul}|^2}\Big)}, \tag{5.34}$$

with $B = \frac{\alpha\beta_k}{(1-\alpha)\psi_k}\sum_{j=1}^{K}\tau_j\sum_{n=1}^{N}\sum_{m=1}^{M}|\hat{h}_{m,n,j}^{dl}|^2 P_{m,n,j}^{dl}$.

Proof. See Appendix B.4 □

As shown in Appendix B.4, the PRS problem is non-convex considering all variables jointly. Hence, an iterative algorithm is used to find the local optimum solutions of the DL and UL power allocations as shown in Algorithm 4.

Algorithm 4 Power Resource Allocation Algorithm

Set time and weight allocations α, τ_k, ψ_k, ω_k^{dl} and ω_k^{ul}
repeat
  Calculate λ_k^{ul} using (5.34)
  Calculate $P_{m,n,k}^{ul}$ using (5.33)
  Find λ^{dl} using bisection method
  Calculate $P_{m,n,k}^{dl}$ using (5.32)
until (5.29) converges

Algorithm 5 WSR: Joint Resource Allocation Algorithm

Run line search to find $x^\star$ for the TRS optimization
Set time resource allocation to equal allocation
Calculate the weight using $\omega_k^\star = \frac{2x^\star K \log(2)}{T^2}$
Perform UL and DL IIC using Algorithm 3
Find $P_{m,n,k}^{dl}$ and $P_{m,n,k}^{ul}$, using Algorithm 4
Calculate sum-rate using the objective function in (5.24)

5.3.2.3 WSR: Joint Resource Allocation

The optimal solutions of the TRS and PRS allocation problems in addition to the IIC algorithm are used in a joint resource allocation algorithm to find the maximum WSR as described in Algorithm 5. The performance of the optimal joint resource allocation algorithm is compared with five suboptimal schemes in the next section.

5.3.3 Complexity Analysis

Here, the complexity analysis for the proposed optimal SWIPT protocol is compared to five suboptimal schemes. The list of schemes presented in this section are OOOA, FEFA, FEOA, FOOA, EEOA and EEFA. The labelling of the various schemes use 'O' to represent optimal allocation, 'F' to represent fixed allocation, and 'E' to represent equal allocation. Also, each of the first three letters in the scheme names represent the type of allocation for a particular resource. The first letter represents the time allocation type, the second letter represents the power allocation type, the third letter represents the weight allocation type, and the last letter stands for 'allocation', that is, 'time', 'power', 'weight', 'allocation'. For example, OOOA means optimal time, optimal power, and optimal weights allocations. The various schemes' names and descriptions are given in Table 5.1.

A centralized processing approach is utilized for the optimal resource allocation, in which all the processing involved in solving problem $P(1)$ are implemented at the BS. This is because the BS has a larger processing capacity, can obtain the global CSI and has a constant power supply. The optimal time and power allocations and weight values are sent to the UNs in the DL phase. Note that the fixed weight for each UN is set as 5 in the simulation. In addition, the fixed time allocation is achieved by randomly choosing the time allocated for each UN.

Table 5.1 List of Resources and Weights Allocation Schemes

Scheme	Considerations
OOOA	Optimal time, Optimal power and Optimal weights Allocations
FEFA	Fixed time, Equal power and Fixed weights Allocations
FEOA	Fixed time, Equal power and Optimal weights Allocations
FOOA	Fixed time, Optimal power and Optimal weights Allocations
EEOA	Equal time, Equal power and Optimal weights Allocations
EEFA	Equal time, Equal power and Fixed weights allocations

Now, considering the computational complexity, assume that the processing complexity of the optimal joint resource allocation algorithm, IIC algorithm, power allocation algorithm and the line search method are given by $\mathcal{O}(I_{WSR})$, $\mathcal{O}(I_{IIC})$, $\mathcal{O}(I_{PWR})$, and $\mathcal{O}(I_{LSM})$, respectively. In addition, the computation of an arithmetic operation is defined as $\mathcal{O}(A)$. Note that the big O value for each algorithm includes all the arithmetic calculations involved in that algorithm. For example $\mathcal{O}(I_{WSR})$ consists of the computational complexities of the IIC algorithm, power allocation algorithm and the line search algorithm for finding the time and weight allocations. Hence the order of complexity in this simulation follows as $\mathcal{O}(I_{WSR}) \gg \mathcal{O}(I_{IIC}) \geq \mathcal{O}(I_{PWR}) > \mathcal{O}(I_{LSM}) \gg \mathcal{O}(A)$. The value of $\mathcal{O}(I_{IIC})$ may be greater or equal to $\mathcal{O}(I_{PWR})$ because the IIC algorithm depends on the complexity of the FBMC modulation and demodulation and the number of iteration, as shown in Chapter 4. From the simulation results, the line search method converges quickly and involves fewer computations compared to the power algorithm. Also, a lower number of computations is needed to perform an arithmetic operation.

First, the OOOA scheme runs the joint resource allocation algorithm with complexity $\mathcal{O}(I_{WSR})$. Hence, the complexity of the OOOA scheme is given as $\mathcal{O}(I_{WSR}) = \mathcal{O}(I_{IIC}) + \mathcal{O}(I_{PWR}) + \mathcal{O}(I_{LSM}) + \mathcal{O}(A)$. Next, in the FEFA and EEFA schemes only the IIC algorithm is implemented. Thus, their complexity is given by $\mathcal{O}(I_{IIC})$. The FEOA and EEOA schemes perform the IIC algorithm and some arithmetic operations to obtain the optimal weights. Therefore, the complexity in both schemes is given as $\mathcal{O}(I_{IIC}) + \mathcal{O}(A)$. Finally, for the FOOA scheme the IIC algorithm, power allocation algorithm and arithmetic operations are implemented, with complexity given as $\mathcal{O}(I_{IIC}) + \mathcal{O}(I_{PWR}) + \mathcal{O}(A)$. The complexity analysis for the centralized approach is presented in Table 5.2.

Note that the centralized approach reduces the processing complexity and power consumption at the UN. However, each UN must perform IIC at the information receiver, which requires local CSI. A detailed complexity analysis of the IIC algorithm is given in Chapter 4, including a discussion on alternative approaches to reducing this complexity. It is shown in Chapter 4 that only a few IIC iterations are sufficient to remove the intrinsic interference in FBMC-QAM. Furthermore, the batteries at the UNs are recharged continuously, while the IIC processing is only needed when the node receives a downlink packet. In most mMTC applications, the amount of downlink data received is very small

Table 5.2 Complexity of Different Schemes

Scheme	Node	Computational Complexity
OOOA	BS	$\mathcal{O}(I_{IIC}) + \mathcal{O}(I_{PWR}) + \mathcal{O}(I_{LSM}) + \mathcal{O}(A)$
	UN	$\mathcal{O}(I_{IIC})$
FEFA	BS	$\mathcal{O}(I_{IIC})$
	UN	$\mathcal{O}(I_{IIC})$
FEOA	BS	$\mathcal{O}(I_{IIC}) + \mathcal{O}(A)$
	UN	$\mathcal{O}(I_{IIC})$
FOOA	BS	$\mathcal{O}(I_{IIC}) + \mathcal{O}(I_{PWR}) + \mathcal{O}(A)$
	UN	$\mathcal{O}(I_{IIC})$
EEOA	BS	$\mathcal{O}(I_{IIC}) + \mathcal{O}(A)$
	UN	$\mathcal{O}(I_{IIC})$
EEFA	BS	$\mathcal{O}(I_{IIC})$
	UN	$\mathcal{O}(I_{IIC})$

compared to the uplink transmission. As such the IIC processing will be implemented periodically and can therefore be supported by the harvested power in the batteries.

5.4 Simulation Results

In this section, numerical results are presented for the proposed multi-user FBMC-based SWIPT system. A set up with 1.4 MHz channel bandwidth and 4-QAM modulation is considered in the simulation. The noise spectral density is set as $N_0 = -174$ dBm/Hz. The UNs are assumed to be randomly distributed within a 10 m radius around the BS. For the channel model, the Friis model is assumed for the path loss with $\kappa = 2$, $A = 1$ and $\tilde{d} = \lambda/4\pi$ [110]. Here, the energy conversion efficiency in the linear region of the EH receiver is set to 0.5 [109]. Unless otherwise stated, each plot assumes $K = 4$ UNs.

5.4.1 Proof and Convergence Analysis

In this subsection, simulation results on Theorem 1, and the convergence of Algorithm 4 are discussed.

5.4.1.1 TRS Allocation Results

For the time resource allocation, simulation results are presented to affirm Theorem 1. Fig. 5.2 shows plots for the T_{RS} of two UNs for DL (top half) and UL (bottom half) communications. It can be observed from these plots that the T_{RS} allocations of both UNs are similar for both UL and DL. This is consistent with Theorem 1, which states that the x value in (5.30) is the same for all UNs in both UL and DL. Also, time and weight allocations are the same. A similar deduction on the x value can be inferred from Fig. 5.3.

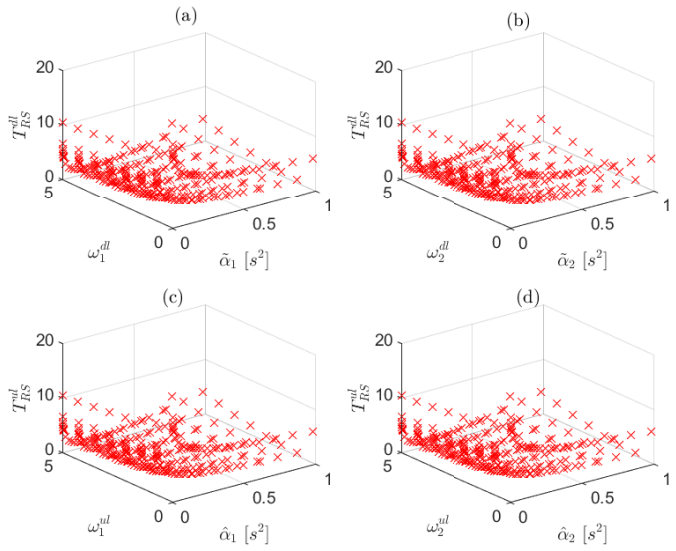

Fig. 5.2 $T_{RS}^{(dl/ul)}$ convexity plot with respect to the weight and time resource of two UNs, where $K = 2$. The 3D plot of T_{RS}^{dl} against the; (a) UN_1's DL weight and time allocation, (b) UN_2's DL weight and time allocation. The 3D plot of T_{RS}^{ul} against (c) UN_1's UL weight and time allocation, and (c) UN_2's UL weight and time allocation.

From Fig. 5.3 it is shown that both the x and z functions in (5.30) for DL and UL communications are the same and possess the same optimal value. This implies that, the BS only has to determine x once, and this can be done by using a simple line search method. In this chapter, the Golden Section Search method is used [143]. Fig. 5.4 shows the convergence curve for the Golden Section Search method. From Fig. 5.4, it can be observed that the line search method converges after 10 iterations. This implies that determining the value of x and the time and weight allocations would not be computationally intensive.

5.4.1.2 PRS Allocation Results

Fig. 5.5 shows the convergence plot for the DL and UL power allocation algorithm. From the figure, it can be observed that 10 iterations is enough to achieve convergence in Algorithm 4. Hence, Algorithm 4 will also not result in a huge computational burden at the BS.

5.4.2 Harvested Power Simulations

In this subsection, simulation results on the energy harvested in the proposed system considering a non-linear EH model are presented. With the antenna threshold effect, the maximum amount of energy harvested by each UN can not exceed $\Delta_k P_{th}$, due to the non-linear behaviour of the EH circuit. The saturation threshold power is set as 7 dBm [22].

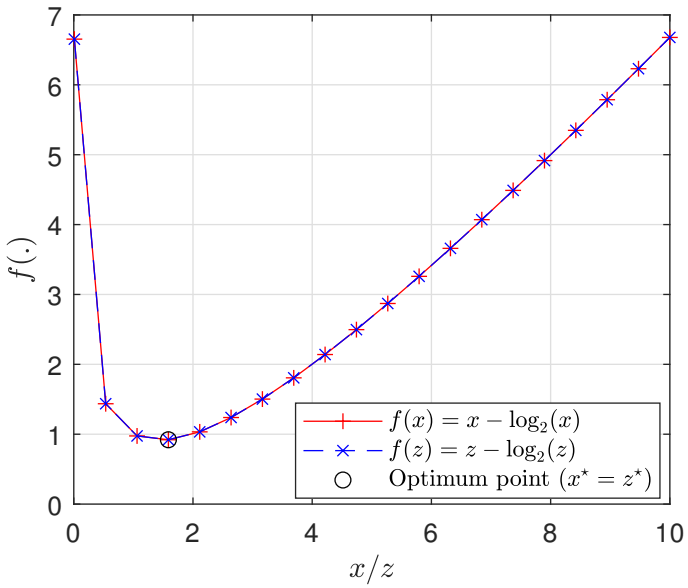

Fig. 5.3 Concavity plot of x-log and z-log functions

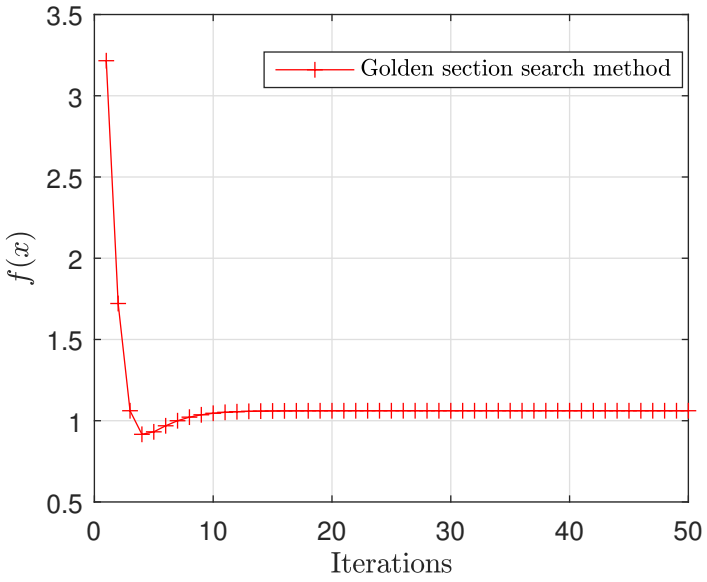

Fig. 5.4 Convergence plot for the x-log function

Fig. 5.6 shows a plot of the amount of power harvested against the BS transmit power. From the figure, it can be observed that as the transmit power increases, the amount of power harvested by each UN increases. There is a constant increase until the EH threshold is reached, which occurs around $P^{dl}_{0,max} = 35$ dBm in Fig. 5.6. At this point, the power harvested cannot exceed the threshold due to

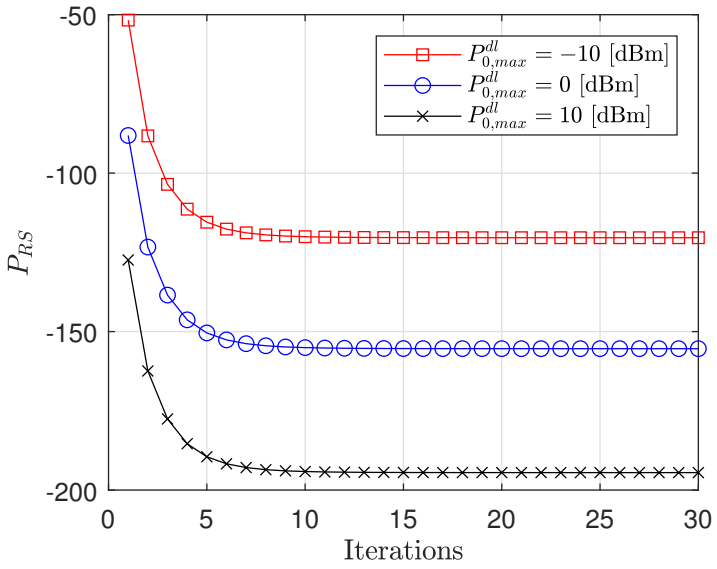

Fig. 5.5 P_{RS} function convergence plot with increasing number of algorithm iterations, where $K = 4$ and $P^{dl}_{0,max} = -10$dB, 0dB, and 10dB.

the non-linear behaviour of the energy harvester. It can be seen from Fig. 5.6 that, in the range of BS transmit power considered in the simulation, the EH receiver operates predominantly in the linear region for $P_{th} = 7$ dBm. If a different value of P_{th} is selected, the linear and non-linear regions of the EH receiver will be shifted accordingly. In addition, Fig. 5.6 shows that all the schemes with equal power allocation (i.e., FEFA, FEOA, EEOA, and EEFA) show a completely linear behaviour over the range of BS transmit powers.

From Fig. 5.6 (a) it is shown that the available power at each UN is the same for the OOOA scheme because of the equal time allocation for the DL and UL communication. A similar behaviour is observed for the EEOA and the EEFA schemes. Also, in the FEFA scheme, UNs have equal power because of the equal power allocation in the DL. However, for the FOOA and FEOA schemes, since there are different time allocations for the DL and UL, the power harvested by each UN is different. Fig. 5.6 (a) shows that for a BS transmit power of 30 dBm, each UN can harvest power of 0 dBm (1 mW) using the proposed optimal scheme. Assuming a typical mMTC device that transmits data for a time duration of 450 ms with a maximum peak power of 200 mW and a duty cycle of 10 %, it is shown in [144] that if the data transmission occurs every minute the average power transmitted over the period is 0.15 mW. This implies that the amount of energy harvested by the proposed scheme is more than six times the average transmit power required in the UL transmission of such a device. This results show that, the intrinsic interference in FBMC systems can be exploited as a useful signal to power energy constrained devices.

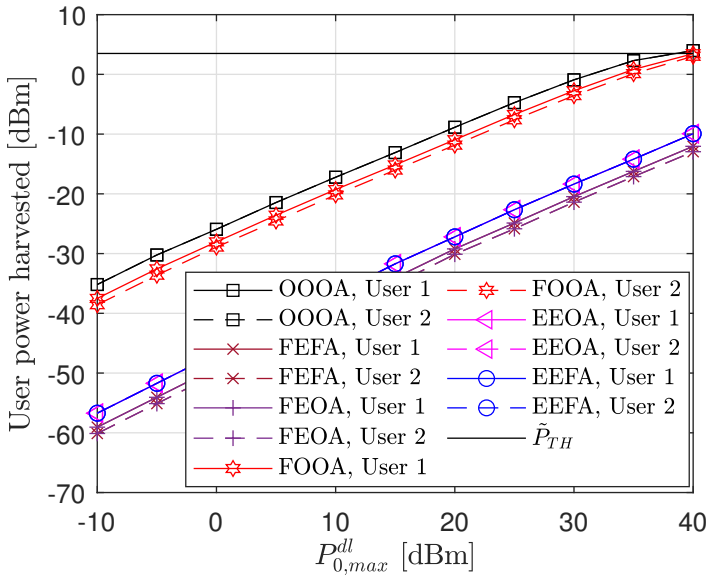

(a) User power harvested, $K = 2$.

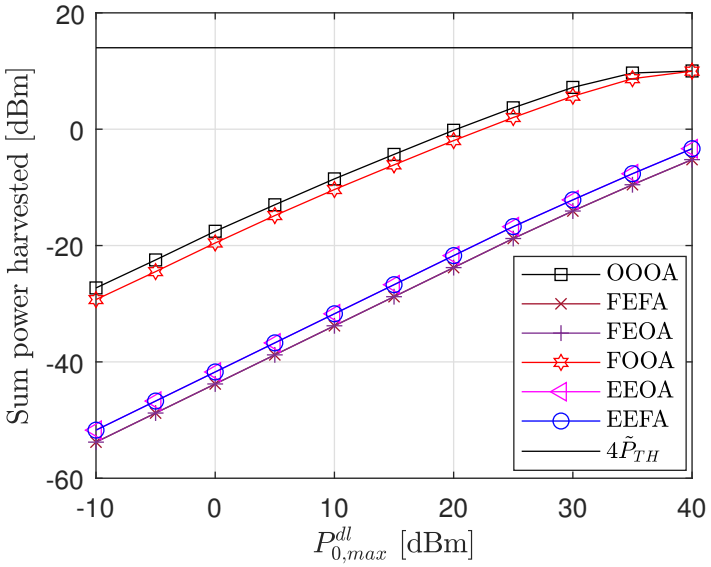

(b) Total power harvested, where $K = 4$

Fig. 5.6 Power harvested versus BS transmit power

Moreover, the amount of harvested energy could be maximised by exploiting the information antenna as an energy antenna during the time slots when it is not decoding information. That is, the UN can operate with the separate receiver architecture during its ID time slot. However, a TS scheme can be used to switch the information antenna to an energy antenna in other time slots. This means that each UN can collect energy with two antennas instead of one, in $K-1$ time slots, which can significantly increase the power harvested by each UN.

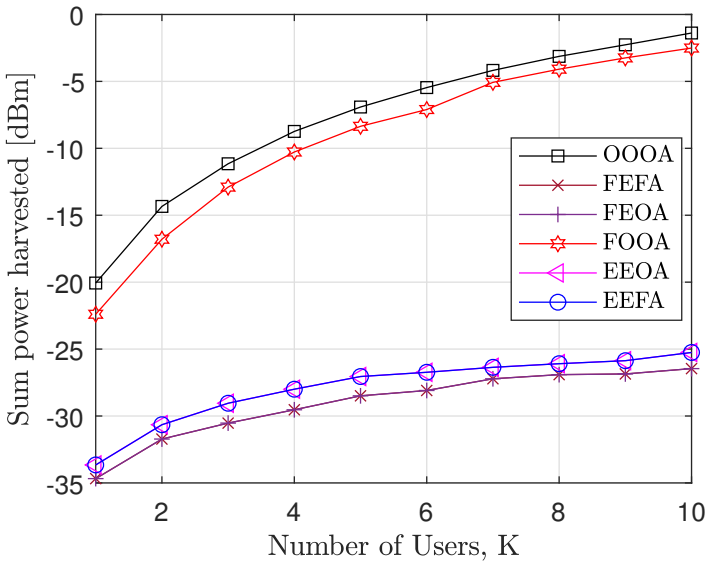

Fig. 5.7 Total power harvested versus increasing number of UNs, where $P_{0.max}^{dl} = 0$ dBm.

Unlike Fig. 5.6 (a), which shows the amount of power harvested by each UN, Fig. 5.6 (b) shows a plot of the total power harvested by 4 UNs. It can be observed from Fig. 5.6 (b) that the OOOA harvests the most energy and therefore has the highest power available for its UL communication. The order of decreasing amount of power harvested is as follows: OOOA, FOOA, FEFA, EEOA, EEFA, and FEFA. Fig. 5.7 shows the total amount of power harvested for each scheme with an increasing number of UNs. From the figure, it can be observed that the amount of energy harvested increases with an increasing number of UNs. For the schemes with equal power allocation, increasing the number of UNs beyond $K = 6$ does not significantly improve the amount of power harvested. This implies that optimizing the power allocated to each UN is necessary to maximize the amount of harvested energy.

5.4.3 Weighted Sum-Rate and Bit-Error-Probability Simulations

5.4.3.1 Weighted Sum-Rate

Fig. 5.8 (a) shows a plot of the weighted sum-rate against BS transmit power. From the plot the descending order of performance is as follows: OOOA, FOOA, EEOA, FEOA, EEFA and FEFA. It can be observed from the figure that the schemes with optimized resource allocations performed better compared to the schemes with fixed resource allocations. Also, it can be seen that the optimal scheme (OOOA) attains the best performance as expected. Note, however, that the scheme with fixed time allocation is only slightly poorer than the fully optimal scheme. This affirms the deductions made in the previous section that the fixed time allocation coincides with the optimal time allocation.

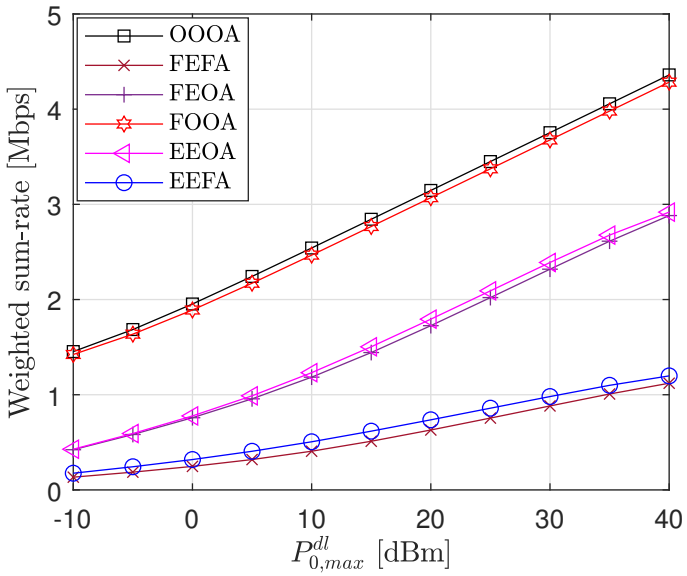

(a) $K = 4$

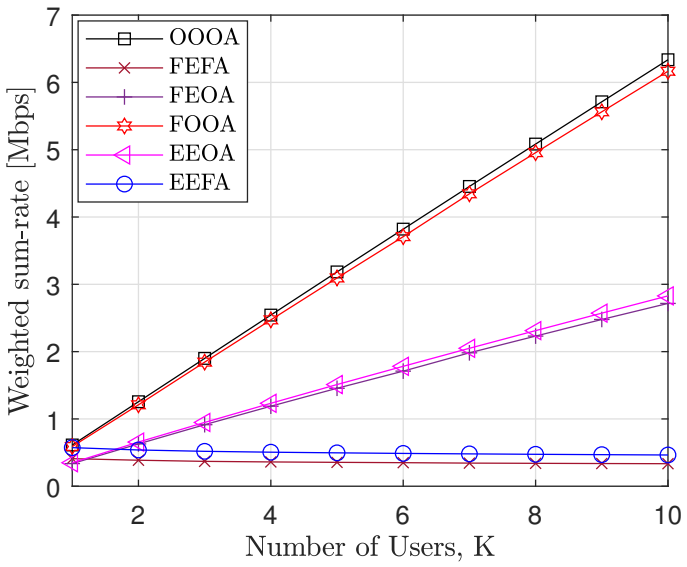

(b) $P^{dl}_{0,max} = 10$ dBm

Fig. 5.8 Weighted sum-rate versus (a) BS transmit power (b) number of UNs

A plot showing the effect of increasing number of UNs on the weighted sum-rate is presented in Fig. 5.8 (b). As expected, with an increasing number of UNs the weighted sum-rate increases for all schemes except FEFA and EEFA. The weighted sum-rate for the FEFA and EEFA schemes remains constant as the number of UNs increases. This is due to the equal/fixed time, power and weight allocations. However, the schemes with either time, power or weight allocations being optimized

compensates for the poor performance of the other equally allocated resources, as shown for the EEOA and FEOA curves.

5.4.3.2 Bit-Error-Probability

The bit-error-probability (BEP) expression for the k-th UN can be obtained as in [145], and is given by

$$BEP_k^i = \frac{1}{NM} \sum_{m=1}^{M} \sum_{n=1}^{N} Q(\sqrt{SNR_{m,n,k}^i}) \tag{5.35}$$

where $Q(\cdot)$ denotes the Q-function and i is the transmission phase, i.e. DL or UL.

Figs. 5.9 (a) and 5.9 (b) show the average BEP for the DL and the UL communications, respectively. From Fig. 5.9 (a), all schemes with equal power allocations have the same BEP values. In addition, the OOOA has a similar BEP when compared to the FOOA scheme due to the use of the DL optimal power and weight allocations for both schemes. Fig. 5.9 (b) considers the UL BEP for the various schemes. The UL depends on the UL power for each UN, which in turn depends on the amount of power harvested during the DL communication phase (i.e., the power available depends on both the DL and UL time allocations). As expected, OOOA and FOOA have better performance compared to the other schemes. In addition, the UL BEP of EEFA, EEOA, FEFA and FEOA schemes are different due to both the time (i.e., equal DL and UL time allocations) and the optimal UL power allocation in each scheme. As can be seen from 5.9 (b), a BEP of 10^{-4} can be achieved by the OOOA scheme on the uplink when the BS transmits with a power of 10 dBm.

5.5 Summary

In a multi-user mMTC network with energy-constrained devices, SWIPT can serve as a source of power for UNs and provide network self-sustainability. In addition, FBMC-QAM is a promising waveform for future wireless applications due to its high spectral efficiency and suitability for asynchronous transmissions. This chapter investigated the combination of SWIPT and FBMC-QAM for future networks. Specifically, a multi-user FBMC-based SWIPT system is considered where each UN has two antennas, one for EH and the other for ID. A practical non-linear model is considered at the energy receiver, whereas an IIC receiver is employed at the information receiver. A WMMSE problem is solved to optimize the time, weight and power allocations. Five sub-optimal schemes are proposed for comparison. The complexity analysis of the proposed optimal and sub-optimal schemes is also presented. The results show that the optimal time and weight allocations coincide with equal time and weight allocation. In terms of average sum-rate at BS transmit power of 20 dBm, the optimal scheme outperforms the scheme with equal time, equal power, and optimal weight allocation by about 40%. In summary, the proposed FBMC-based SWIPT system is a promising technique for future applications due to the capability of achieving network self-sustainability, high spectral efficiency and suitability for asynchronous transmissions simultaneously. Furthermore, the results

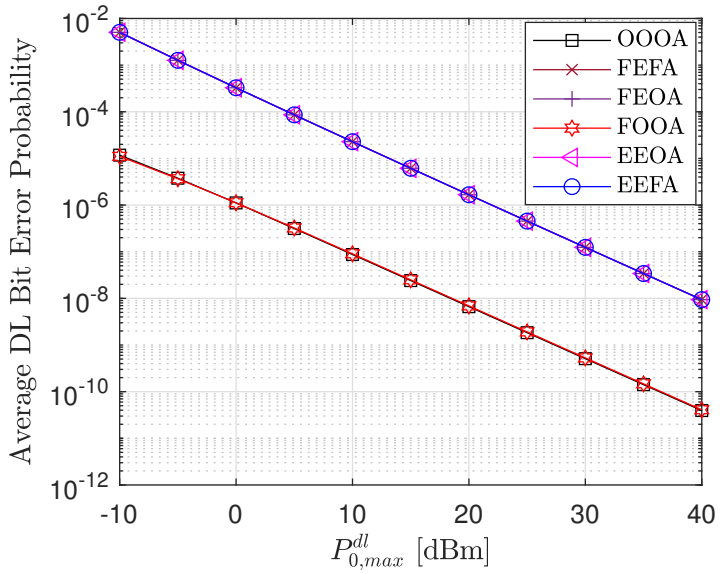

(a) DL

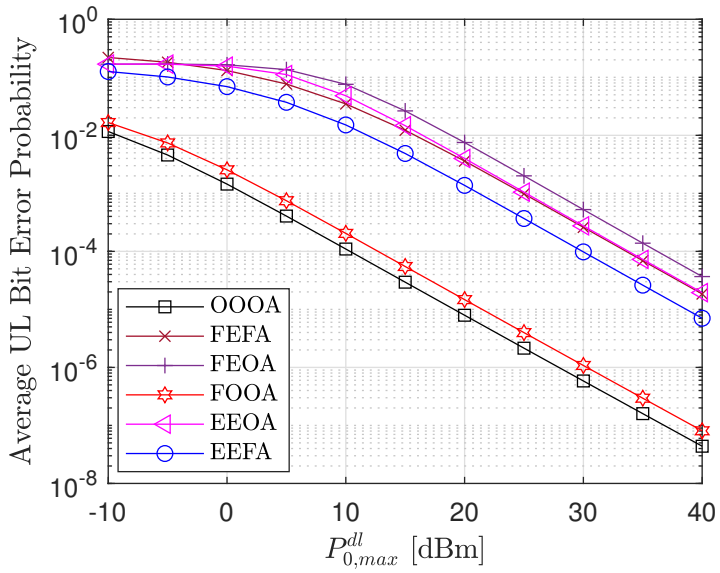

(b) UL

Fig. 5.9 Average BEP versus source transmit power, where $K = 4$

show that the intrinsic interference in FBMC systems can be opportunistically exploited to power energy constrained devices. In Chapter 6, a multi-user systems is investigated in which UNs with different requirements are served with different numerologies. In addition, the benefit of FBMC over OFDM in asynchronous scenarios will be studied.

Chapter 6

Multi-User Interference Cancellation for Uplink FBMC-based Multiple Access Channel

6.1 Introduction

As outlined in Chapter 2, future wireless networks are expected to handle the coexistence of many use cases, including eMBB, mMTC and URLLC. In order to connect to the network, UN performs an uplink synchronization procedure by sending a scheduling request to the BS and waiting for the BS to grant it radio resources [146]. For some use cases, such as mMTC, this grant-based multiple access will result in a huge synchronization overhead due to the high connection density. To resolve this problem, grant-free transmission has been investigated for mMTC applications, in which each UN operates in a wake-up-and-transmit manner [146]. However, in a grant-free system there is timing misalignment of UN transmissions which introduces asynchronous interference in the demodulated signal of each UN [147]. CP-OFDM, which has been adopted for 5G NR, requires the grant-based synchronization procedure in order to maintain orthogonality between subcarriers [31]. However, CP-OFDM has been shown to be inefficient for the relaxed synchronization required in grant-free transmissions [148, 149].

From the perspective of the PHY, the different use cases can be supported by assigning different BWPs with different numerologies [148, 150]. For instance, mMTC applications might require a BWP with smaller subcarrier spacing and longer symbol duration in order to support a high number of delay-tolerant devices. On the other hand, URLLC applications will require significantly shorter symbol duration compared with mMTC scenarios, due to their more stringent latency and reliability requirements. The purpose of this chapter is to investigate a novel interference cancellation receiver for asynchronous multi-user uplink FBMC-based systems. First, the case of a single numerology multi-user FBMC-QAM system is considered. In addition, an FDM based multi numerology system

is considered in which different BWPs, with different requirements, adopt different numerologies. In both systems, the corresponding challenges with interference are tackled using the proposed interference cancellation receiver. Following the results obtained in Chapter 4, the proposed receiver uses BICM-ID which combines FBMC-QAM demodulation and SISO decoding for signal detection. To cancel the interference terms the proposed receiver employs PIC and IIC. During the initial decoding iteration, each UN's transmit signal is estimated and used to cancel MUI or INI in the PIC phase. In the subsequent decoding iterations IIC is used to cancel the intrinsic interference present in each UN's received signal.

The remainder of this chapter is organized as follows: Section 6.2 presents the case for single numerology uplink asynchronous FBMC-QAM system. Subsections 6.2.1, 6.2.2, 6.2.3 and 6.2.4 present the transmitter model, received signal without TO, received signal with TO and FBMC-QAM demodulation, respectively. The system model for the mixed numerology FBMC-QAM system is presented in Section 6.3. In Section 6.4 the proposed BICM-ID receiver with interference cancellation is presented. Simulation results are presented in Section 6.5 to illustrate the performance of the proposed receiver for both single numerology and mixed numerology models. Finally, concluding remarks are made in Section 6.6.

6.2 System Model with Single Numerology

6.2.1 Transmit Signal

Consider an uplink FBMC-QAM system in which K UNs transmit data to a single antenna BS in a grant-free manner. A FDMA scheme is employed in which each UN transmits its data sporadically on a portion of the M available subcarriers. Note that, unlike Chapter 5 which employed TDMA for the resource allocation, FDMA is used in this chapter because of the nature of the 5G NR mixed numerology system. As mentioned in Chapter 2, 5G NR divides the available system bandwidth into different BWPs, that can have different numerologies or subcarrier spacing. In this section, a single numerology FBMC-QAM system is considered, in which BWPs with the same numerology are assigned to UNs with identical network requirements. There is a total of N FBMC-QAM symbols on each subcarrier. The transmitter of each UN is identical to the one discussed in Chapter 4, where a stream of information bits $\mathbf{b}$ are encoded to generate a coded bit stream $\mathbf{c}$. The encoded bits are randomly interleaved and mapped onto a QAM constellation to generate the data symbols. Let $d_{m,n}^{(k)}, \in \mathscr{M}_k$ denote the QAM modulated data of UN k associated with subcarrier index m and symbol n, where $\mathscr{M}_k$ constitute the set of subcarriers assigned to UN k and $\mathbb{E}\left[|d_{m,n}^{(k)}|^2\right] = 1$. Here, it is assumed that each subcarrier is allocated to only one UN. Thus, $\cup_{k=1}^{K} \mathscr{M}_k = \{0,1,\ldots,M-1\}$ and $\mathscr{M}_l \cap \mathscr{M}_t = \phi$ for $l \neq t$. Following the system model in Chapter 4, the discrete time FBMC-QAM transmit signal of UN k can be expressed as

$$s_k[i] = \sum_{m \in \mathscr{M}_k} \sum_{n=0}^{N-1} d_{m,n}^{(k)} g_{m,n}^{(k)}[i] \tag{6.1}$$

where i represents the sample index and $g_{m,n}^{(k)}[i]$ is the time and frequency shifted version of the the prototype filter impulse response, $g[i]$, given as

$$g_{m,n}^{(k)}[i] = g[i - nM_k/2]e^{j\frac{2\pi mi}{M_k}} \tag{6.2}$$

where M_k is the number of elements in the set $\mathscr{M}_k$, the sequence $g[i]$ has length $L_k = D \times M_k$ with D as the overlapping factor. Note that the exponential term in (6.2) represents the IFFT operation. As shown in Chapter 4, an efficient and low complexity implementation of the prototype filtering in FBMC systems is the PPN [129]. Adopting the PPN implementation and following the notation in [151], (6.1) can be rewritten in vector form as

$$\mathbf{s}_k = \mathbf{G}_k \mathbf{d}_k \tag{6.3}$$

with

$$\mathbf{d}_k = \left[d_{1,1}^{(k)} d_{2,1}^{(k)} \dots d_{M_k,1}^{(k)} d_{1,2}^{(k)} d_{2,2}^{(k)} \dots d_{M_k,N}^{(k)}\right]^T$$

$$\mathbf{G}_k = \left[\mathbf{g}_{1,1}^{(k)} \mathbf{g}_{2,1}^{(k)} \dots \mathbf{g}_{M_k,1}^{(k)} \mathbf{g}_{1,2}^{(k)} \mathbf{g}_{2,2}^{(k)} \dots \mathbf{g}_{M_k,N}^{(k)}\right]$$

Here, $\mathbf{s}_k \in \mathbb{C}^{F_k \times 1}$ is the transmit signal vector of UN k, $\mathbf{d}_k \in \mathbb{C}^{P_k \times 1}$ is the vector of stacked data on all N symbols and M_k subcarriers of UN k, where $F_k = L_k N$ and $P_k = M_k N$. In addition, $\mathbf{g}_{m,n}^{(k)} \in \mathbb{C}^{F_k \times 1}$ is the vector of all samples of $g_{m,n}^{(k)}[i]$ and $\mathbf{G}_k \in \mathbb{C}^{F_k \times P_k}$ is the transmit filter matrix.

6.2.2 Received Signal without Timing Offset

In the absence of TO, the received signal at the BS from all UNs can be expressed as

$$y[i] = \sum_{k=1}^{K} (s_k[i] * h_k[i]) + z[i] \tag{6.4}$$

where $h_k[i]$ for $0 \leq i \leq L_{ch} - 1$ is the L_{ch}-tap multipath fading channel between UN k and the BS and $z[i]$ represents the AWGN with zero mean and variance σ_0^2. The vector form of (6.4) is expressed as

$$\mathbf{y} = \sum_{k=1}^{K} \mathbf{H}_k \mathbf{s}_k + \mathbf{z} \tag{6.5}$$

where $\mathbf{H}_k \in \mathbb{C}^{F_k \times F_k}$ is the circulant channel matrix of the k-th UN based on $h_k[i]$ and $\mathbf{z} \in \mathbb{C}^{F_k \times 1}$ AWGN vector. Note that each element of $\mathbf{H}_k$ is assumed to be an independent and identically distributed (i.i.d.) complex Gaussian random variable with zero mean and variance $\sigma_h^2 = \mathbb{E}\left[|h_k[i]|^2\right]$.

6.2.3 Received Signal with Timing Offset

Consider the scenario of grant-free uplink transmission, in which each UN transmits its data asynchronously. In this scenario, signals from different UNs arrive at the BS with different TO, τ_k. The two cases of TO are illustrated below:

6.2.3.1 Timing error to the right (Signals arrive τ_k samples early)

In this case, τ_k samples to the right side of the current FBMC-QAM symbol are replaced with samples from the next symbol. From (6.1), let the time-domain sequence of the n-th symbol be expressed as $s_{n,k}[i] = \sum_{m \in \mathscr{M}_k} d_{m,n}^{(k)} g_{m,n}^{(k)}[i]$. Thus, the received signal at the BS based on TO to the right can be represented as

$$y_n^r[i] = \sum_{k=1}^{K} \left(x_{n,k}[i+\tau_k] \times R_k[i] + x_{n+1,k}^r[i+\tau_k] \times \bar{R}_k[i] \right) + z[i] \tag{6.6}$$

where $x_{n,k}[i] = s_{n,k}[i] * h_k[i]$ represents the current symbol and $x_{n+1,k}^r[i+\tau_k]$ is the next symbol. Also, $R_k[i]$ denotes the TO variable with a value of 1 when sample i is selected and 0 when sample i is not selected, i.e.

$$R_k[i] = \begin{cases} 1, & 0 \le i \le L_k - \tau_k - 1 \\ 0, & L_k - \tau_k \le i \le L_k - 1 \end{cases} \tag{6.7}$$

and $\bar{R}_k[i]$ is a complement of $R_k[i]$ obtained by swapping 0s and 1s. Substituting (6.1) into (6.6) and following the notation in [152], the received signal in (6.6) can be represented in vector form as

$$\mathbf{y}^r = \sum_{k=1}^{K} \left(\mathbf{R}_k \mathbf{H}_k \mathbf{G}_k \mathbf{d}_k + \bar{\mathbf{R}}_k \mathbf{H}_k \begin{bmatrix} \mathbf{G}_{k,1} \mathbf{d}_k^{next} \\ \mathbf{G}_{k,2} \mathbf{d}_k \end{bmatrix} \right) + \mathbf{z} \tag{6.8}$$

where $\mathbf{R}_k$ and $\bar{\mathbf{R}}_k \in \mathbb{C}^{F_k \times F_k}$ are the TO matrices, given respectively as

$$\mathbf{R}_k = \begin{bmatrix} \mathbf{0}_{(F_k-\tau_k)\times\tau_k} & \mathbf{I}_{(F_k-\tau_k)} \\ \mathbf{0}_{\tau_k} & \mathbf{0}_{\tau_k \times (F_k-\tau_k)} \end{bmatrix},$$

$$\bar{\mathbf{R}}_k = \begin{bmatrix} \mathbf{0}_{(F_k-\tau_k)\times\tau_k} & \mathbf{0}_{(F_k-\tau_k)} \\ \mathbf{I}_{\tau_k} & \mathbf{0}_{\tau_k \times (F_k-\tau_k)} \end{bmatrix}.$$

Also, $\mathbf{G}_{k,1} \in \mathbb{C}^{(F_k - L_{ch}) \times P_k}$ and $\mathbf{G}_{k,2} \in \mathbb{C}^{L_{ch} \times P_k}$ are sub-matrices of $\mathbf{G}_k$ that can be expressed as

$$\mathbf{G}_{k,1} = \mathbf{G}_k(1 : (F_k - L_{ch}), :),$$

$$\mathbf{G}_{k,2} = \mathbf{G}_k((F_k - L_{ch} + 1) : F_k, :).$$

The received signal in (6.8) can be expanded as

$$\begin{aligned}\mathbf{y}^r &= \sum_{k=1}^{K} \left(\left(\mathbf{R}_k \mathbf{H}_k \mathbf{G}_k + \bar{\mathbf{R}}_k \mathbf{H}_{k,2} \mathbf{G}_{k,2} \right) \mathbf{d}_k + \bar{\mathbf{R}}_k \mathbf{H}_{k,1} \mathbf{G}_{k,1} \mathbf{d}_k^{next} \right) + \mathbf{z} \\ &= \sum_{k=1}^{K} \left(\mathbf{B}_{k,2}^r \mathbf{d}_k + \mathbf{B}_{k,1}^r \mathbf{d}_k^{next} \right) + \mathbf{z}\end{aligned} \tag{6.9}$$

where $\mathbf{H}_{k,1}$ and $\mathbf{H}_{k,2}$ are sub-matrices of $\mathbf{H}_k$, i.e. $\mathbf{H}_k = [\mathbf{H}_{k,1} \mathbf{H}_{k,2}]$. Also, $\mathbf{B}_{k,2}^r = \mathbf{R}_k \mathbf{H}_k \mathbf{G}_k + \bar{\mathbf{R}}_k \mathbf{H}_{k,2} \mathbf{G}_{k,2}$ and $\mathbf{B}_{k,1}^r = \bar{\mathbf{R}}_k \mathbf{H}_{k,1} \mathbf{G}_{k,1}$.

6.2.3.2 Timing error to the left (Signals arrive τ_k samples late)

In this case, τ_k samples to the left side of the current FBMC-QAM symbol are replaced with samples from the previous symbol. In CP-based waveforms, e.g. CP-OFDM and GFDM, the impact of TO to the left can be compensated for using a large enough CP. For a CP duration L_{cp}, only $t = \max(L_{ch} - (L_{cp} + \tau_k), 0)$ samples of the previous symbol interfere with the current symbol. However, since FBMC systems do not employ CP, τ_k symbols of the previous symbol will affect the current symbol. Therefore, similar to (6.6), the received signal at the BS based on TO to the left can be expressed as

$$y_n^l[i] = \sum_{k=1}^{K} \left(x_{n,k}[i + \tau_k] \times R_k[i] + x_{n-1,k}^l[i + \tau_k] \times \bar{R}_k[i] \right) + z[i] \tag{6.10}$$

where $x_{n-1,k}^l[i + \tau_k]$ is the previous symbol. Similar to (6.8), the vector form of (6.10) is represented as

$$\mathbf{y}^l = \sum_{k=1}^{K} \left(\mathbf{R}_k \mathbf{H}_k \mathbf{G}_k \mathbf{d}_k + \bar{\mathbf{R}}_k \mathbf{H}_k \begin{bmatrix} \mathbf{G}_{k,1} \mathbf{d}_k \\ \mathbf{G}_{k,2} \mathbf{d}_k^{prev} \end{bmatrix} \right) + \mathbf{z}. \tag{6.11}$$

In this case, $\mathbf{R}_k$ and $\bar{\mathbf{R}}_k \in \mathbb{C}^{F_k \times F_k}$ are defined respectively as

$$\mathbf{R}_k = \begin{bmatrix} \mathbf{I}_{(F_k - \tau_k)} & \mathbf{0}_{(F_k - \tau_k) \times \tau_k} \\ \mathbf{0}_{\tau_k \times (F_k - \tau_k)} & \mathbf{0}_{\tau_k} \end{bmatrix},$$

$$\bar{\mathbf{R}}_k = \begin{bmatrix} \mathbf{0}_{(F_k - \tau_k)} & \mathbf{0}_{(F_k - \tau_k) \times \tau_k} \\ \mathbf{0}_{\tau_k \times (F_k - \tau_k)} & \mathbf{I}_{\tau_k} \end{bmatrix}.$$

By expanding the signal in (6.11), we obtain

$$\begin{aligned}\mathbf{y}^l &= \sum_{k=1}^{K} \left((\mathbf{R}_k \mathbf{H}_k \mathbf{G}_k + \bar{\mathbf{R}}_k \mathbf{H}_{k,1} \mathbf{G}_{k,1}) \, \mathbf{d}_k + \; \bar{\mathbf{R}}_k \mathbf{H}_{k,2} \mathbf{G}_{k,2} \mathbf{d}_k^{prev} \right) \\ &\quad + \mathbf{z} \\ &= \sum_{k=1}^{K} \left(\mathbf{B}_{k,1}^l \mathbf{d}_k + \mathbf{B}_{k,2}^l \mathbf{d}_k^{prev} \right) + \mathbf{z}\end{aligned} \tag{6.12}$$

where $\mathbf{B}_{k,1}^l = \mathbf{R}_k \mathbf{H}_k \mathbf{G}_k + \bar{\mathbf{R}}_k \mathbf{H}_{k,1} \mathbf{G}_{k,1}$ and $\mathbf{B}_{k,2}^l = \bar{\mathbf{R}}_k \mathbf{H}_{k,2} \mathbf{G}_{k,2}$.

6.2.4 FBMC Demodulation

The received signal is passed through the FBMC-QAM demodulator which consists of receive filtering and FFT operation as shown in Fig. 6.4. Considering the case of received signal without TO, the frequency domain signal for the k-th UN after filtering and FFT is given as

$$\begin{aligned}\hat{\mathbf{d}}_k &= \mathbf{G}_k^H \mathbf{y} \\ &= \mathbf{G}_k^H \mathbf{H}_k \mathbf{G}_k \mathbf{d}_k + \sum_{u=1, u \neq k}^{K} \mathbf{G}_k^H \mathbf{H}_u \mathbf{G}_u \mathbf{d}_u + \mathbf{G}_k^H \mathbf{z}\end{aligned} \tag{6.13}$$

Using (6.1) and (6.4), the first term in (6.13) can be expanded as

$$\begin{aligned}\mathbf{G}_k^H \mathbf{H}_k \mathbf{G}_k \mathbf{d}_k &= s_k[i] * h_k[i] \\ &= \sum_{i=-\infty}^{\infty} \sum_{m \in \mathscr{M}_k} \sum_{n=0}^{N-1} d_{m,n}^{(k)} g_{m',n'}^{(k)*}[i] g_{m,n}^{(k)}[i] * h_k[i]\end{aligned} \tag{6.14}$$

Note that, in CP-OFDM systems the transmit and receive filters are designed to satisfy the orthogonality condition, i.e.

$$\sum_{i=-\infty}^{\infty} g_{m',n'}^{(k)*}[i] g_{m,n}^{(k)}[i] = \delta_{m,m'} \delta_{n,n'} \tag{6.15}$$

where $\delta_{\{.\}}$ denoted the Kronecker delta function with $\delta_{m,m'} = 1$ if $m = m'$ and $\delta_{m,m'} = 0$ if $m \neq m'$. However, in FBMC-QAM systems, the prototype filters cannot achieve subcarrier orthogonality. Therefore, the expression in (6.14) can be rewritten as

$$\mathbf{G}_k^H \mathbf{H}_k \mathbf{G}_k \mathbf{d}_k = d_{m',n'}^{(k)} H_k + I_{m',n'}^{(k)} H_k \tag{6.16}$$

where $H_k = \sum_{i=1}^{L_{ch}} h_k[i] e^{-j\frac{2\pi m i}{M_k}}$ denotes the channel frequency response and $I_{m,n}^{(k)}$ is the intrinsic interference caused by the lack of subcarrier orthogonality in FBMC-QAM, which is expressed as

$$I_{m',n'}^{(k)} = \sum_{(m',n') \neq (m,n)} d_{m,n}^{(k)} \sum_{i=-\infty}^{\infty} g_{m',n'}^{(k)*}[i] g_{m,n}^{(k)}[i] \tag{6.17}$$

Before detection and decoding of the demodulated signal, the effect of the frequency-selective channel is compensated by applying a simple one-tap ZF equalizer. Substituting (6.16) into (6.13), the estimated data of UN k associated with the m'-th subcarrier of the n'-th symbol after equalization is given by

$$\hat{d}^{(k)}_{m',n'} = d^{(k)}_{m',n'} + I^{(k)}_{m',n'} + \underbrace{\sum_{u=1,u\neq k}^{K} \tilde{\mathbf{H}}_u \mathbf{d}_u}_{\text{MUI}} + \tilde{\mathbf{z}} \tag{6.18}$$

where $\tilde{\mathbf{H}}_u = \mathbf{H}_k^{-1}\mathbf{G}_k^H\mathbf{H}_u\mathbf{G}_u$ and $\tilde{\mathbf{z}} = \mathbf{H}_k^{-1}\mathbf{G}_k^H\mathbf{z}$.

On the other hand, considering the case with TO, the frequency domain signal of k-th UN after FBMC-QAM demodulation and equalization is given as

$$\begin{aligned}\hat{\mathbf{d}}_k &= \mathbf{G}_k^H \mathbf{y}^J \\ &= \mathbf{G}_k^H \mathbf{B}^J_{k,\nu}\mathbf{d}_k + \mathbf{G}_k^H \mathbf{B}^J_{k,\nu}\mathbf{d}_k^Q + \sum_{u=1,u\neq k}^{K} \left(\mathbf{G}_k^H \mathbf{B}^J_{u,\nu}\mathbf{d}_u + \mathbf{G}_k^H \mathbf{B}^J_{u,\nu}\mathbf{d}_u^Q\right) + \tilde{\mathbf{z}}\end{aligned} \tag{6.19}$$

where $\mathbf{d}_k^Q$ represents the data on the next or previous symbol of UN k, $\{\cdot\}^J$ represents either $\{\cdot\}^r$ or $\{\cdot\}^l$ and ν is either 1 or 2. The second term in (6.19) represents the TO-induced interference (TOI). Similar to (6.13), the first term in (6.19) consist of the desired signal and intrinsic interference terms. Thus, after equalization, the detected data signal associated with the m'-th subcarrier of the n'-th symbol in the presence of timing errors can be written as

$$\hat{d}^{(k)}_{m',n'} = d^{(k)}_{m',n'} + I^{(k)}_{m,n} + \underbrace{\tilde{\mathbf{H}}_{k,\nu}\mathbf{d}_k^Q}_{\text{TOI}} + \underbrace{\sum_{u=1,u\neq k}^{K} \left(\tilde{\mathbf{H}}_{u,\nu}\mathbf{d}_u + \tilde{\mathbf{H}}_{u,\nu}\mathbf{d}_u^Q\right)}_{\text{MUI}} + \tilde{\mathbf{z}} \tag{6.20}$$

where $\tilde{\mathbf{H}}_{k,\nu} = \mathbf{H}_k^{-1}\mathbf{G}_k^H\mathbf{B}^J_{k,\nu}$.

6.3 System Model with Mixed Numerologies

In the scenario with mixed numerologies, the frame structure of UNs are specified based on their communication requirements. Applications with similar requirement share the same numerology, whereas different numerologies are assigned to applications with significantly different requirements, such as eMBB and URLLC [148]. In the current 5G NR air interface standardization, a generalized synchronized design with an integral least common multiplier (LCM) symbol duration is adopted as the family of numerologies. Considering the LCM approach the subcarrier spacing and symbol duration of different numerologies are related as

$$\triangle f^{(\iota)} = n_\iota \triangle f^{(\iota+1)},\ T^{(\iota+1)} = n_\iota T^{(\iota)},\ n_\iota = 2^\mu \tag{6.21}$$

where $\triangle f^{(\iota)}$ and $T^{(\iota)}$ represent the subcarrier spacing and symbol duration, respectively, of numerology ι and μ is an integer. Typically, the total system bandwidth is split into several BWPs shared by multiple UNs. UNs with similar (different) performance requirements are assigned to BWPs with the same (different) numerologies. Here, it is assumed that different BWPs have the same sampling rate [150]. Without loss of generality, the special case of two adjacent BWPs, each occupied by one UN is considered in this section in order to simplify the derivation. For this case, we have $\triangle f^{(1)} = n_1 \triangle f^{(2)}$ and $T^{(2)} = n_1 T^{(1)}$. In the frequency domain, this means that the subcarrier spacing of BWP 1 is n_1 times larger than the subcarrier spacing of BWP 2. In the time domain, on the other hand, this implies that n_1 symbols of BWP 1 have the same duration as one symbol of BWP 2.

In order to simplify the derivation and analysis of INI, the scenario with n_1 FBMC-QAM symbols in BWP 1 and one FBMC-QAM symbol in BWP 2 is considered, i.e. $N^{(1)} = n_1$ and $N^{(2)} = 1$. Therefore, following the vector notation in (6.3), the transmit signals at the two UNs can be expressed as

$$\mathbf{s}_{n_1}^{(1)} = \mathbf{G}_{n_1}^{(1)} \mathbf{d}_{n_1}^{(1)}; \;\; \mathbf{s}_1^{(2)} = \mathbf{G}_1^{(2)} \mathbf{d}_1^{(2)} \tag{6.22}$$

where $\mathbf{d}_{n_1}^{(1)} \in \mathbb{C}^{P^{(1)} \times 1}$ and $\mathbf{G}_{n_1}^{(1)} \in \mathbb{C}^{F^{(1)} \times P^{(1)}}$ represent the data signal vector and the transmit filter matrix, respectively, of BWP 1. Here, $P^{(1)} = n_1 M^{(1)}$ and $F^{(1)} = n_1 L^{(1)}$, where $M^{(1)}$ and $L^{(1)}$ represent the number of subcarriers and prototype filter length of BWP 1, respectively. Also, $\mathbf{d}_1^{(2)} \in \mathbb{C}^{M^{(2)} \times 1}$ and $\mathbf{G}_1^{(2)} \in \mathbb{C}^{L^{(2)} \times M^{(2)}}$ represent the data signal vector and the transmit filter matrix, respectively, of BWP 2. Note that the subscripts indicate the number of symbols for each UN.

Considering the case without TO, the received signal at the BS can be written as

$$\mathbf{y} = \mathbf{H}_{n_1}^{(1)} \mathbf{G}_{n_1}^{(1)} \mathbf{d}_{n_1}^{(1)} + \mathbf{H}_1^{(2)} \mathbf{G}_1^{(2)} \mathbf{d}_1^{(2)} + \mathbf{z} \tag{6.23}$$

where $\mathbf{H}_{n_1}^{(1)}$ and $\mathbf{H}_1^{(2)}$ are the circulant matrices of UN 1 and UN 2, respectively and $\mathbf{z}$ is the AWGN vector. Similar to (6.13), the demodulated signal of UN 1 can be expressed as

$$\begin{aligned} \hat{\mathbf{d}}_{n_1}^{(1)} &= \mathbf{G}_{n_1}^{(1)H} \mathbf{y} \\ &= \mathbf{G}_{n_1}^{(1)H} \mathbf{H}_{n_1}^{(1)} \mathbf{G}_{n_1}^{(1)} \mathbf{d}_{n_1}^{(1)} + \mathbf{G}_{n_1}^{(1)H} \mathbf{H}_1^{(2)} \mathbf{G}_1^{(2)} \mathbf{d}_1^{(2)} + \mathbf{G}_{n_1}^{(1)H} \mathbf{z} \end{aligned} \tag{6.24}$$

Following the derivation in (6.16), the first term in (6.24) can be decomposed into the desired signal and intrinsic interference terms. The second term in (6.24) denotes the INI from BWP 2 to BWP 1. After equalization of the demodulated signal, the estimated data of UN 1 associated with the m'-th subcarrier of the n'-th symbol after equalization is given by

$$\hat{d}_{m',n'}^{(1)} = d_{m',n'}^{(1)} + I_{m',n'}^{(1)} + \underbrace{\tilde{\mathbf{H}}_1 \mathbf{d}_1^{(2)}}_{\text{INI}} + \tilde{\mathbf{z}}^{(1)} \tag{6.25}$$

where $\tilde{\mathbf{H}}_1 = \mathbf{H}_{n_1}^{(1)-1} \mathbf{G}_{n_1}^{(1)H} \mathbf{H}_1^{(2)} \mathbf{G}_1^{(2)}$, $I_{m',n'}^{(1)}$ is the intrinsic interference in UN 1 due to the lack of subcarrier orthogonality in FBMC-QAM and $\tilde{\mathbf{z}}^{(1)} = \mathbf{H}_{n_1}^{(1)-1} \mathbf{G}_{n_1}^{(1)H} \mathbf{z}$. Also, the demodulated signal of

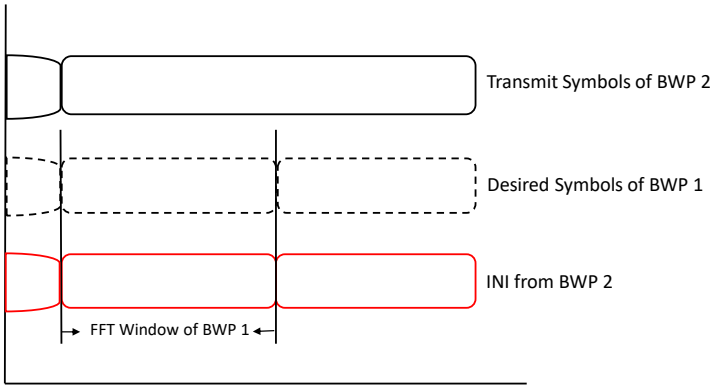

Fig. 6.1 Illustration of the INI affecting BWP 1.

UN 2 can be expressed as

$$\begin{aligned}\hat{\mathbf{d}}_1^{(2)} &= \mathbf{G}_1^{(2)H}\mathbf{y} \\ &= \mathbf{G}_1^{(2)H}\mathbf{H}_1^{(2)}\mathbf{G}_1^{(2)}\mathbf{d}_1^{(2)} + \mathbf{G}_1^{(2)H}\mathbf{H}_{n_1}^{(1)}\mathbf{G}_{n_1}^{(1)}\mathbf{d}_{n_1}^{(1)} + \mathbf{G}_1^{(2)H}\mathbf{z}\end{aligned} \tag{6.26}$$

Therefore, the estimated data signal of UN 2 after equalization can be expressed as

$$\hat{d}_{m',1}^{(2)} = d_{m',1}^{(2)} + I_{m',1}^{(2)} + \underbrace{\tilde{\mathbf{H}}_{n_1}\mathbf{d}_{n_1}^{(1)}}_{\text{INI}} + \tilde{\mathbf{z}}^{(2)} \tag{6.27}$$

where $\tilde{\mathbf{H}}_1 = \mathbf{H}_1^{(2)-1}\mathbf{G}_1^{(2)H}\mathbf{H}_{n_1}^{(1)}\mathbf{G}_{n_1}^{(1)}$, $I_{m',1}^{(2)}$ represents the intrinsic interference in UN 2 and $\tilde{\mathbf{z}}^{(2)} = \mathbf{H}_1^{(2)-1}\mathbf{G}_1^{(2)H}\mathbf{z}$.

An illustration of the INI in a mixed numerology system with $n_1 = 2$ is shown in Figs. 6.1 and 6.2. Note that for the purposes of illustration Figs. 6.1 represents the case without TO. As shown in Fig. 6.1, the FFT window of BWP 1 (with shorter symbol duration) is shorter than one symbol of BWP 2 (with longer symbol duration). Therefore, the two symbols of BWP 1 overlap with parts of the single symbol of BWP 2. As a result, the INI experienced by BWP 1 comes from only one symbol of BWP 2. On the other hand, as shown in Fig. 6.2, the FFT window of BWP 2 is longer than the length of one symbol of BWP 1. Specifically, the one symbol of BWP 2 overlaps with two symbols of BWP 1. Therefore, the INI affecting BWP 2 comes from two symbols of BWP 1. Similar to the single numerology system, in the presence of TO additional interference may be experienced from the next or previous FBMC-QAM symbol depending on whether the TO is to the left or to the right. The derivation of TOI in this case follows from Subsection 6.2.3 and is therefore omitted here. However, in Section 6.5, the case with TO will be considered for the simulation of the mixed numerology system. In the next section the proposed interference cancellation based BICM-ID receiver is illustrated.

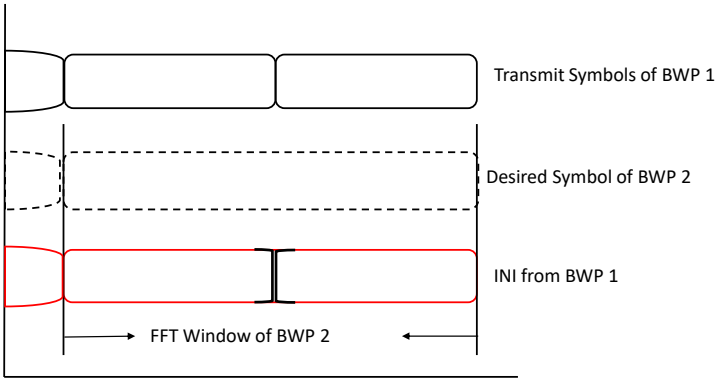

Fig. 6.2 Illustration of the INI affecting BWP 2.

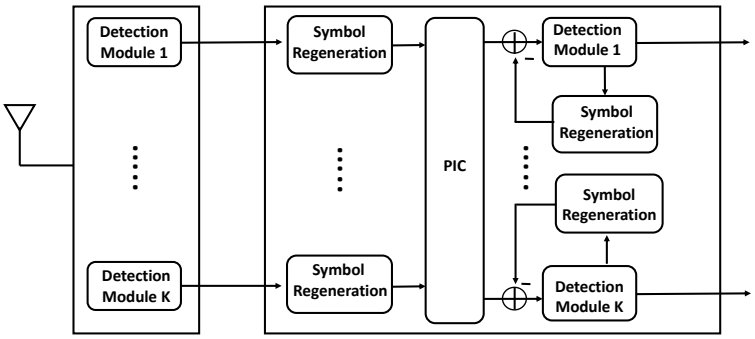

Fig. 6.3 Proposed BICM-ID receiver with interference cancellation.

6.4 BICM-ID Receiver with Interference Cancellation

In this section, an iterative receiver is proposed to cancel the different interference terms present in the system models described in Sections 6.2 and 6.3, respectively. For simplicity of analysis, it is assumed that the CSI is known at the BS. As shown in Fig. 6.3, the proposed receiver consist of three main parts. First, the Detection Module which is made up of the receive filter or AFB, the FFT operation, channel equalization, soft demapper, interleaver and SISO decoder. Next, Symbol Regeneration which is used to estimate the different interference terms. Last, the Interference Cancellation part, which cancels the interference terms in the demodulated signals using the output of the Symbol Regeneration phase. The different components of the proposed receiver are presented below.

6.4.1 Detection Module

In the detection model, the AFB, FFT and equalization make up the FBMC-QAM demodulation, which is described above for both single numerology and mixed numerology models. The soft demapper and SISO decoder are described below.

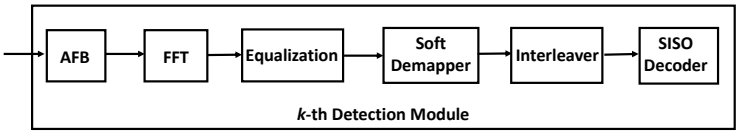

Fig. 6.4 Block diagram of the detection module.

6.4.1.1 Soft Demapper

The demodulated signal is passed to the soft demapper which computes the extrinsic LLRs of the b-th bit of the n-th symbol of the desired UN using sum-product decoding [149]. The extrinsic LLRs, L^e_{Dem}, are deinterleaved and passed to the SISO decoder as *a priori* LLR, L^a_{Dec}.

6.4.1.2 SISO Decoder

The SISO decoder calculates the *a posteriori* LLRs of the coded bits L^p_{Dec}, after a predefined number of iterations. As in Chapter 4, a LDPC decoder with an irregular parity-check matrix is considered as the SISO decoder. For the next iteration of the receiver, the extrinsic LLRs, defined as $L^e_{Dec} = L^p_{Dec} - L^a_{Dec}$, are passed to the soft mapper to regenerate the transmitted symbols.

6.4.2 Symbol Regeneration

In this step, the transmitted symbols of all UNs are estimated and used for interference cancellation. Specifically, the extrinsic LLRs provided by the SISO decoder are interleaved and passed to a soft mapper as *a priori* information, L^a_{Map}. The output of the soft mapper is FBMC-QAM modulated to obtain the estimates of the transmitted signal from each UN.

6.4.3 Interference Cancellation

To remove the intrinsic interference, TOI and MUI or INI terms from the detected signal, an interference cancellation operation is performed using the regenerated symbols as shown in Fig. 6.3. The proposed interference cancellation algorithm proceeds as follows:

- In the single numerology case, the receiver obtains the soft estimated signals from all UNs and removes the MUI terms in (6.18) and (6.20) by performing PIC in the first receiver iteration. That is, to decode the signal of UN k, the sum of the signals from all other UNs are subtracted from the received signal of UN k to cancel the MUI. Similarly, in the mixed numerology case, the received signal of all UNs are estimated and used to cancel the INI terms in (6.25) and (6.27) using PIC.

- In the subsequent receiver iterations, IIC is employed to remove the intrinsic interference and TOI terms. That is, for each UN the intrinsic interference and TOI terms are estimated and

subtracted from the received signal in multiple decoding iterations. The IIC implementation in this step is similar to the one employed in Chapter 4.

- When the maximum number of IIC iterations is reached, L_{Dec}^{p} is used to generate the hard-decision estimates of the transmitted bits, $\hat{\mathbf{b}}$.

6.5 Simulation Results

In this section, simulation results are presented to compare the performance of CP-OFDM and FBMC-QAM in an asynchronous uplink FDMA system. For the simulation setup, a 5G NR scenario is considered in which a group of contiguous PRB or BWP is assigned to each UN. Each PRB consists of 12 subcarriers. In this simulation, BWPs made up of 6 PRBs are assigned to each UN. For simplicity, the case of 2 UNs transmitting to the BS is considered in the simulation. In the single numerology case, both UNs adopt a subcarrier spacing of 15 kHz. However, in the mixed numerology case, the first UN adopt subcarrier spacing $\triangle f^{(1)} = 30$ kHz, while the second UN has a subcarrier spacing $\triangle f^{(2)} = 15$ kHz. The CSI is assumed to be perfectly known at the BS. Similar to Chapter 4, the EVA and ETU channel models are considered in this chapter. For the SISO decoder, an LDPC decoder with irregular parity-check matrix is employed whereas sum-product decoding is used as the demapper. In addition, the PHYDYAS prototype filter with overlapping factor $D = 4$ is used at both the UN and BS. For the synchronous CP-OFDM case, a CP of length $L_{cp} = 16$ samples is considered. A comparison of CP-OFDM and FBMC-QAM is presented for two uplink transmission scenarios: (i) the transmission of both UNs are synchronized at the BS (ii) UN transmissions arrive at the BS with a random number of samples in delay. First, the results for the single numerology model is presented for both the synchronous and asynchronous scenarios. Then the results for the mixed numerology model is presented.

6.5.1 Performance of Single Numerology System

Fig. 6.5 shows the average BER performance of two UNs using the same numerology for both CP-OFDM and FBMC-QAM. Note that the results shown in Fig. 6.5 are without interference cancellation. In the synchronous case, CP-OFDM achieves near optimum BER performance and has no error floor as shown in Fig. 6.5. This is due to the use of CP and guard band in CP-OFDM, which maintains subcarrier orthogonality and compensates the effect of channel frequency selectivity. On the other hand, an error floor appears at high SNR for FBMC-QAM. This is due to the intrinsic interference caused by the loss of subcarrier orthogonality in FBMC-QAM. As can be seen from Fig. 6.5, in the asynchronous case FBMC-QAM does not incur a significant performance loss. This is because of the improved frequency localization of FBMC-QAM which reduces its sensitivity to timing errors, without using any CP. In the case of CP-OFDM, asynchronous transmission results in a significant performance loss, especially when the CP is shorter than the number of samples in delay. Thus,

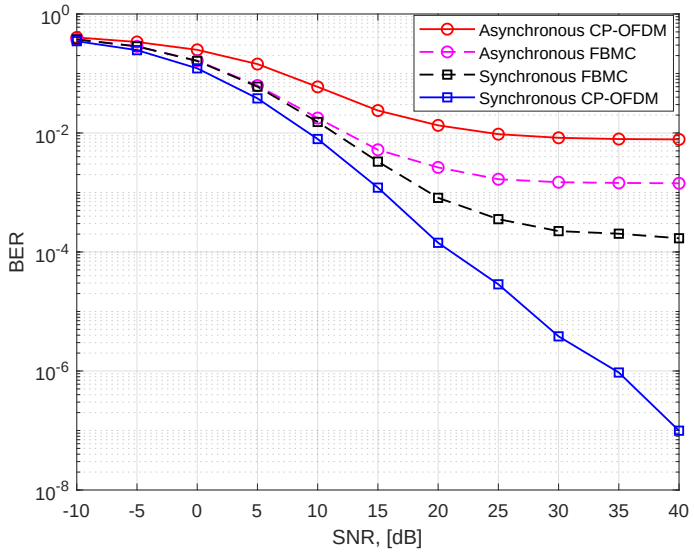

Fig. 6.5 Average BER performance of CP-OFDM vs FBMC-QAM in synchronous and asynchronous multiple access channel with single numerology.

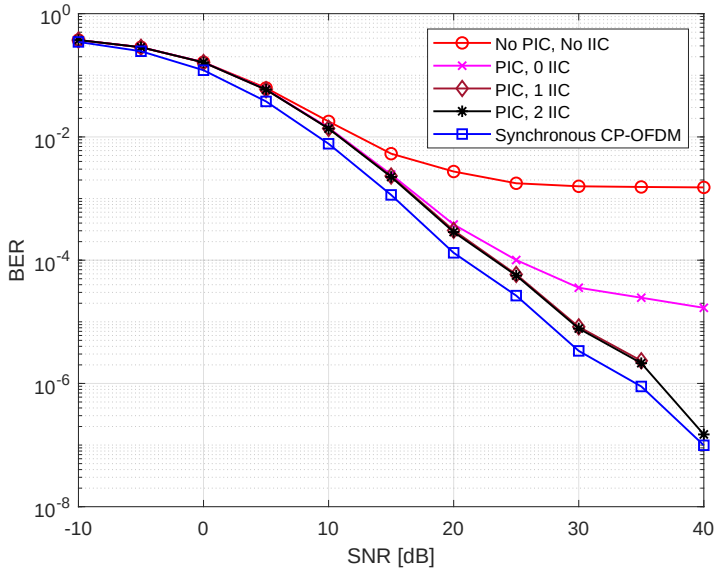

Fig. 6.6 Average BER performance of the proposed receiver for asynchronous FBMC-QAM with single numerology in EVA channel.

FBMC-QAM has the advantage of higher spectral efficiency compared to CP-OFDM since it can combat the effect of timing errors without employing additional resources in terms of CP or guard band.

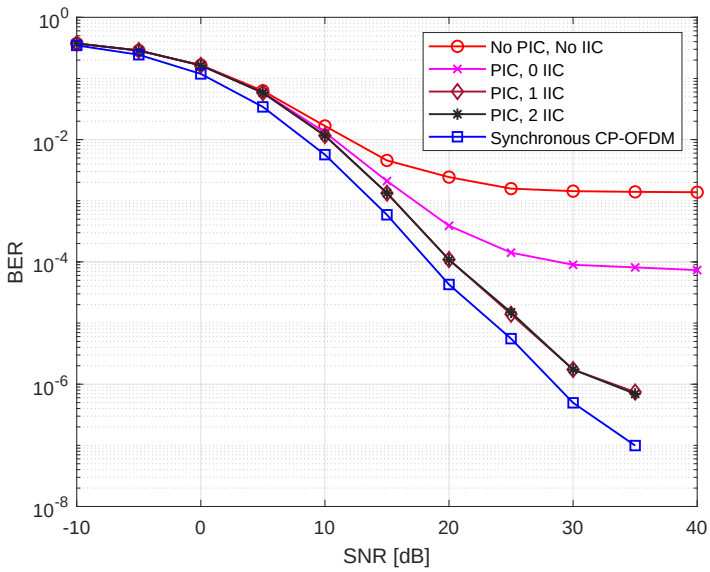

Fig. 6.7 Average BER performance of the proposed receiver for asynchronous FBMC-QAM with single numerology in ETU channel.

In Fig. 6.6 the average BER performance of the proposed BICM-ID receiver with interference cancellation is presented for asynchronous FBMC-QAM over the EVA channel model. Note that the results in Fig. 6.6 represents the case in which two UNs transmit their signals to a BS using the same numerology. As described in Section 6.4, the estimated signals of the two UNs are first used for PIC to remove the MUI term. Then, a fixed number of IIC iterations are performed to eliminate the intrinsic interference and TOI terms. It can be seen in Fig. 6.6 that the combination of PIC and IIC is able to remove the intrinsic interference, TOI and MUI in the proposed FBMC-QAM system. For example, after only one IIC iteration the error floor is completely removed as shown in Fig. 6.6. Measured at 10^{-5} the BER performance of the proposed receiver after 2 IIC iterations for asynchronous FBMC-QAM is only about 2 dB less than the BER performance of synchronous CP-OFDM. As presented in Chapter 4, a lower number of IIC iterations results in a reduced complexity for the iterative process. This implies that the intrinsic interference, TOI and MUI terms can be removed with a manageable receiver complexity.

Similarly, the average BER performance of the proposed BICM-ID receiver with interference cancellation for asynchronous FBMC-QAM over the ETU channel model is shown in Fig. 6.7. Similar to the results presented in Chapter 4, the ETU channel incurs a larger performance loss after 2 IIC iterations compared to the EVA channel. This is because of the longer delay spread in the ETU channel, which worsens the level of intrinsic interference in FBMC-QAM. Moreover, it is shown in Chapter 4 that increasing the number of SISO decoder iterations can improved the decoding performance.

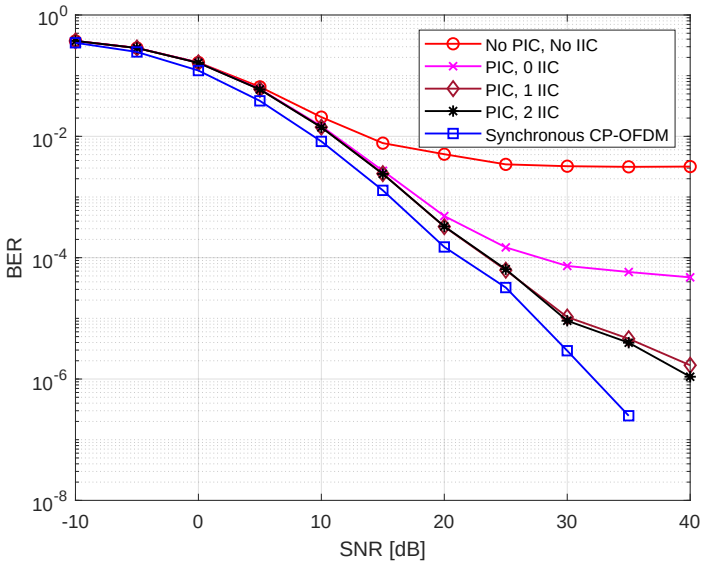

Fig. 6.8 Average BER performance of the proposed receiver for asynchronous FBMC-QAM with mixed numerology in EVA channel.

6.5.2 Performance of Mixed Numerology System

The average BER results presented above shows the performance of a single numerology system. However, as mentioned above, future networks are expected to accommodate services with different performance requirements. Thus, the performance of the proposed receiver is investigated for the case in which the two UNs transmit their signals to the BS using different numerologies. First, Fig. 6.8 shows the average BER performance of the proposed BICM-ID receiver for a mixed numerology FBMC-QAM system over the EVA channel model. Note that the two UNs transmit their signals to the BS asynchronously. As can be seen from Fig. 6.8, the proposed receiver can improve the average BER performance of a mixed numerology FBMC-QAM system through multiple interference cancellation iterations. However, compared to the single numerology case in Fig. 6.6, the mixed numerology case incurs a bigger performance loss in the high SNR regime of the EVA channel model. This is mainly due to the unusual overlap of symbols in the mixed numerology system, which causes INI as shown in Fig. 6.1 and Fig. 6.2. This implies that, for the mixed numerology case a higher number of IIC or SISO decoder iterations are required to achieve comparable BER performance with the single numerology case.

Fig. 6.9 shows the average BER performance of the proposed receiver for the mixed numerology FBMC-QAM system over the ETU channel model. It can be observed from the figure that the average BER performance degrades in the highly frequency selective ETU channel. The figure shows that an error floor appears in the high SNR regime. As mentioned above, a higher number of SISO decoder iterations will be required to completely cancel the interference terms in this case. To track the complexity and convergence of the proposed receiver, the EXIT chart analysis presented in Chapter 4

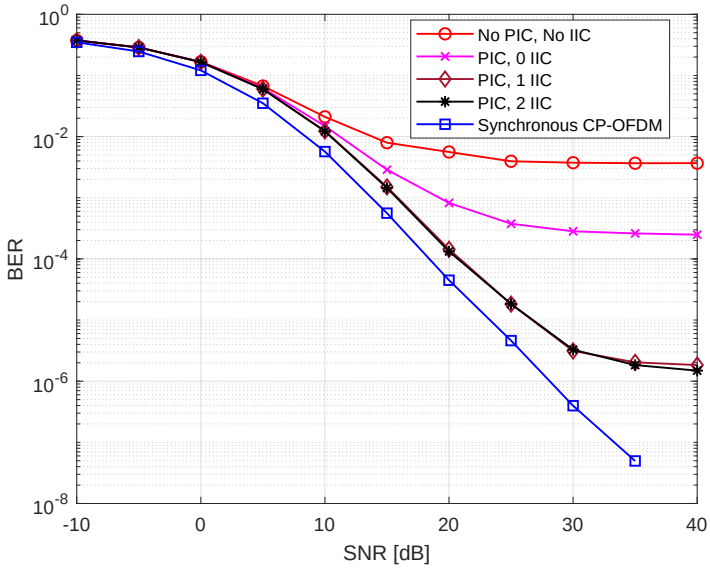

Fig. 6.9 Average BER performance of the proposed receiver for asynchronous FBMC-QAM with mixed numerology in ETU channel.

can be employed. The complexity analysis has been omitted here because it is very similar to the one presented in Chapter 4.

6.6 Summary

In this chapter, FBMC-QAM has been considered as an alternative to CP-OFDM in an uplink multi-user system in the presence of TO. This is due to the high spectral efficiency and ultra-low OOB emission in FBMC-QAM, which make it suitable for grant-free transmissions. In order to accommodate the different use cases of future mobile networks, a mixed numerology FBMC-QAM system has also been investigated. General expressions have been derived for the intrinsic interference, TOI, MUI and INI. To remove the interference terms and improve the BER performance of both the single and mixed numerology models, a BICM-ID receiver is proposed. The proposed receiver performs PIC in the initial decoding iteration to cancel the MUI or INI terms. In subsequent iterations, the receiver performs IIC to eliminate the intrinsic interference and TOI terms. The results show that for the asynchronous case the BER performance of CP-OFDM is significantly degraded compared to the synchronized case. The FBMC-QAM case, on the other hand, shows a robustness against timing offset with only a small performance loss. It is also shown that the proposed receiver can eliminate the interference terms in both the single numerology and mixed numerology systems. In summary, with a receiver that can effectively remove the interference terms, FBMC-QAM is a convenient alternative to CP-OFDM in uplink transmission due to its robustness to timing errors and high spectral efficiency, which is beneficial for future applications such as mMTC.

Chapter 7

Conclusion and Future Work

7.1 Conclusions

FBMC has emerged as a promising waveform candidate to satisfy the requirements of future wireless applications, such mMTC. This is because FBMC systems employ prototype filters that are well localized in both time and frequency domains. This results in a system with improved OOB emission and spectral efficiency compared to conventional CP-OFDM. The improved frequency localization makes FBMC systems resilient against time and frequency offsets. Therefore, FBMC with QAM has been studied in this thesis owing to its superiority compared to other methods, e.g. OQAM. Despite the various advantages of FBMC-QAM systems, its key challenge is the presence of intrinsic interference, which has been addressed in this thesis using IIC and BICM-ID.

In Chapter 3, a mathematical model is derived for an uncoded FBMC-QAM system to analyse the impact of intrinsic interference on the received FBMC-QAM signal. In order to harness the benefits of the improved frequency localization in FBMC-QAM, the received signal is separated into even- and odd-numbered subcarrier components. To effectively cancel the intrinsic interference terms, an IIC receiver is investigated. The proposed receiver uses the decoded even- and odd-numbered subcarrier symbols to iteratively cancel the intrinsic interference from the demodulated signal. The performance of the proposed receiver is then evaluated in simulation under different time-varying channels. It is shown numerically that the IIC algorithm can remove the intrinsic interference in multiple iterations. Also, the proposed FBMC-QAM system has similar OOB emission compared to FBMC-OQAM. Moreover, the proposed FBMC-QAM system significantly outperforms CP-OFDM in OOB emission.

In Chapter 4, a coding based system is investigated to improve the BER performance of FBMC-QAM. At the receiver side, an IIC-based BICM-ID receiver is proposed to cancel the intrinsic interference in FBMC-QAM. Furthermore, to track the convergence and analyse the complexity of the proposed receiver, EXIT chart analysis is investigated for the IIC-based BICM-ID receiver. Using the EXIT charts, the required number of iterations of the proposed receiver to achieve a given BER performance can be predicted. With the knowledge of the required number of iterations, the complexity of the receiver can also be estimated. A mathematical model is derived for the coding

based FBMC-QAM system in the presence of a multipath channel and additive noise. In this model, the demodulated FBMC-QAM signal at the receiver is represented in terms of the desired signal, ICI, ISI and noise. Based on the derived model, IIC and BICM-ID processing is performed at the receiver to cancel the intrinsic interference. The BER performance and EXIT chart analysis are evaluated in numerical simulations under different time-varying channels. It is shown in the results that the IIC-based BICM-ID receiver can significantly improve the BER performance in FBMC-QAM with only a few IIC iterations. Moreover, the EXIT chart analysis can be used to manage the convergence and complexity of the proposed receiver by optimizing the required number of iterations in each simulation scenario.

In Chapter 5, the EH capability of a multi-user FBMC-QAM system is investigated using SWIPT. Specifically, in the considered multi-user FBMC-based SWIPT system, each UN has two antennas. One antenna is dedicated to energy reception in the DL, whereas the other antenna is used for information reception and transmission in the DL and UL, respectively. For the EH at each UN, a practical non-linear model is considered. At the information receiver, IIC is used to cancel the intrinsic interference in FBMC-QAM. In order to optimize the DL and UL weight allocation, time allocation, and power allocation of each UN, a WSR maximization problem is formulated under total DL transmit power and EH constraints. To effectively solve the WSR problem, it is first converted to a WMMSE problem. The equivalent WMMSE problem is then presented as two subproblems for the time and weight allocation optimization and the power allocation optimization. For comparison, five sub-optimal schemes are investigated. The performance of the proposed FBMC-based SWIPT model is evaluated in terms of the harvested power, weighted sum-rate and BEP. It is shown in the simulation results that the intrinsic interference in FBMC-QAM systems can be opportunistically exploited to power energy constrained devices. The results also show that the optimal time and weight allocations coincide with equal time and weight allocation. In addition, the complexity analysis of the optimal and sub-optimal schemes of the proposed FBMC-based SWIPT system is presented.

In Chapter 6, FBMC-QAM is investigated as the PHY waveform in an uplink multi-user system. Both synchronous and asynchronous transmissions are considered in order to compare the performance of FBMC-QAM and CP-OFDM with and without TO. First, a single numerology system is considered in which all UNs transmit their signal using the same numerology, i.e. the same subcarrier spacing and symbol duration. Next, the model is extended to a mixed numerology FBMC-QAM system to accommodate the varying requirements of the different use cases of future mobile networks. Mathematical models are derived for the intrinsic interference, TOI, MUI and INI. Based on the derived models, a BICM-ID receiver is proposed to cancel the interference terms and improve the BER performance of both the single and mixed numerology models. The proposed receiver consists of two interference cancellation phases. In the first phase, PIC is performed to cancel the MUI or INI terms. In the second phase, IIC is performed to remove the intrinsic interference and TOI terms from each UN. It is shown in the simulation results that for the asynchronous case the BER performance of CP-OFDM is significantly degraded compared to the synchronized case. On the other

hand, FBMC-QAM shows a robustness against timing errors with only a small performance loss between the synchronous and asynchronous cases. In addition, it is shown that the proposed receiver is capable of cancelling the interference terms in both the single numerology and mixed numerology systems.

7.2 Future Work

The work presented in this thesis addressed the interference problem in FBMC-QAM systems. IIC is implemented for different system models to cancel the intrinsic interference in FBMC-QAM in order to enable the practical implementation of FBMC-QAM in future wireless networks. Furthermore, this thesis has investigated the combination of FBMC-QAM and SWIPT. This enables SWIPT systems to opportunistically exploit the intrinsic interference in FBMC-QAM for EH. However, there are a number of potential research directions that can be further explored as extensions to the work in this thesis. Some potential future research directions are summarized as follows:

1. **Channel estimation in FBMC-QAM:** For the interference cancellation algorithms in this thesis, it has been assumed that the receiver has perfect channel knowledge. However, in practical systems, receivers are expected to undertake channel estimation. The presence of intrinsic interference can limit the accuracy of channel estimation in FBMC-QAM systems, which can affect the effectiveness of the interference cancellation algorithms in this thesis. Therefore, efficient design of preamble-based channel estimation that can suppress the effect of intrinsic interference could be an extension to the work in this thesis.

2. **TO Estimation:** For the asynchronous communication discussed in Chapter 6, it is assumed that the TO is known at the receiver. A model that considers the estimation of the TO at the receiver and the effect of TO estimation errors on the interference cancellation algorithm is an interesting future work.

3. **Extension of the interference analysis and cancellation to FBMC-QAM based MIMO, Massive MIMO and cell-free massive MIMO systems:** In this thesis, mathematical models have been derived for the interference analysis and cancellation of single antenna systems. However, the concept of massive MIMO is a key technology in future wireless networks. The analysis in this thesis can be extended to MIMO, massive MIMO and cell-free massive MIMO scenarios.

4. **FBMC-QAM with non-orthogonal multiple access:** Non-orthogonal multiple access (NOMA) is a promising physical layer technique that enables non-orthogonal resource allocation in a multi-user system. In Chapters 5 and 6 of this thesis, orthogonal multiple access is considered for the resource allocation. However, since FBMC-QAM is a non-orthogonal waveform, the combination of FBMC-QAM with NOMA could be an interesting extension to the work in this

thesis. For example, the proposed system in Chapter 6 can be extended to an FBMC-based NOMA system, where a NOMA-like SIC receiver can be combined with IIC to effectively remove the interference terms. With such a receiver, UNs with stronger signals can be decoded first. The interference contribution of the stronger UNs can then be subtracted from the received signal of the weaker UNs before IIC operations is implemented. Many other scenarios of FBMC-based NOMA systems, e.g. in cooperative networks, MIMO etc, can be investigated. The combination of NOMA and FBMC may be particularly useful for grant-free transmissions in future networks.

5. **Flexible, use case based prototype filter design:** In Chapter 6, mixed numerology systems have been investigated. In mixed numerology systems, different subcarrier spacing or symbol duration are selected for use cases with different requirements. For FBMC-QAM systems, another layer of flexibility that can be considered is the choice of overlapping factor, which determines the length of an FBMC-QAM symbol. Conventional FBMC systems, like the one considered in this thesis, are designed with long filters (i.e. high overlapping factor) that offer better frequency localization. This is acceptable for delay tolerant applications. However, for low latency applications short prototype filters (i.e. low overlapping factor) should be employed. Therefore, the extension of the current work to the scenario in which the overlapping factor can be selected based on specific system requirements can add another layer of flexibility to mixed numerology FBMC-QAM systems.

6. **Application of Machine Learning:** Another potential future research direction is the application of machine learning for the resource allocation techniques investigated in Chapter 5. Most resource allocation problems in the literature, including the work in this thesis, are solved using conventional convex optimization algorithms, which may require highly complex derivations. In order to reduce the computational complexity of the resource allocation in this thesis, machine learning techniques can be exploited. In particular, due to the fact that the interference signals in FBMC are unknown at the receiver, a technique like reinforcement learning can be employed for interference estimation and resource allocation. The main challenge will be to investigate the optimal actions and rewards needed to achieve a desired result. For such a design, the system learns the interference pattern over time and can be very effective in estimating and cancelling the unwanted interference terms.

Appendix A

Proof for Chapter 4

A.1 Proof of Equation (4.22)

Using (4.20), the complexity of the iterative receiver for FBMC-QAM is given as

$$C_{BICM-ID}^{FBMC} = \mathbb{I}_{Dec} \cdot (\mathbb{I}_{IIC} + 1) \cdot C_{outer} \cdot N_b + N_s \cdot [C_{inner,1}^{FBMC} + \mathbb{I}_{IIC} \cdot C_{inner,i}^{FBMC}] \tag{A.1}$$

where $C_{inner,1}^{FBMC}$ is the complexity of the FBMC-QAM demodulator in the first iteration and $C_{inner,i}^{FBMC}$ is the combined complexity of the FDMC-QAM modulator and demodulator in the subsequent iterations. In terms of complex multiplications FBMC-QAM requires DM multiplications for the filtering process and followed by an M-point FFT. Therefore,

$$C_{inner,1}^{FBMC} = M/2\log_2(M) + DM \tag{A.2}$$

and

$$C_{inner,i}^{FBMC} = 2(M/2\log_2(M) + DM). \tag{A.3}$$

Note that the factor 2 takes into consideration the fact that both FBMC-QAM modulation and demodulation processes are performed during the i-th IIC iteration. Substituting (A.2) and (A.3) into the second term of (A.1) gives

$$\begin{aligned} C_{inner}^{FBMC} &= C_{inner,1}^{FBMC} + \mathbb{I}_{IIC} \cdot C_{inner,i}^{FBMC} \\ &= M/2\log_2(M) + DM + \mathbb{I}_{IIC} \cdot [2(M/2\log_2(M) + DM)] \\ &= M/2\log_2(M) + \mathbb{I}_{IIC} \cdot M\log_2(M) + DM + 2\mathbb{I}_{IIC}DM \\ &= M/2\log_2(M)(1 + 2\mathbb{I}_{IIC}) + DM(1 + 2\mathbb{I}_{IIC}) \end{aligned} \tag{A.4}$$

Rearranging the last term of (A.4), the complexity of the inner decoder due to the FBMC-QAM modulator/demodulator can be finally expressed as

$$C_{inner}^{FBMC} = (1+2\mathbb{I}_{IIC})[M/2\log_2(M)+DM] \tag{A.5}$$

(4.30) follows straightforwardly from substituting (A.4) into (A.5). □

Appendix B

Proof for Chapter 5

B.1 WSR and WMMSE Relationship

From equations (5.8) and (5.20), the DL and UL mean squared error (MSE) for each UN is given as

$$\begin{aligned} e^{dl}_{m,n,k} &= |\hat{h}^{dl}_{m,n,k} P^{dl}_{m,n,k} v^{dl}_{m,n,k} - 1|^2 + \sigma_k^2 |v^{dl}_{m,n,k}|^2 \\ &= 1 + |\hat{h}^{dl}_{m,n,k}|^2 |v^{dl}_{m,n,k}|^2 P^{dl}_{m,n,k} + 2\hat{h}^{dl}_{m,n,k} v^{dl}_{m,n,k} \sqrt{P^{dl}_{m,n,k}} + \sigma_k^2 |v^{dl}_{m,n,k}|^2 \end{aligned} \tag{B.1}$$

and

$$\begin{aligned} e^{ul}_{m,n,k} &= |\hat{h}^{ul}_{m,n,k} P^{ul}_{m,n,k} v^{ul}_{m,n,k} - 1|^2 + \sigma^2 |v^{ul}_{m,n,k}|^2 \\ &= 1 + |\hat{h}^{ul}_{m,n,k}|^2 |v^{ul}_{m,n,k}|^2 P^{ul}_{m,n,k} + 2\hat{h}^{ul}_{m,n,k} v^{ul}_{m,n,k} \sqrt{P^{ul}_{m,n,k}} + \sigma^2 |v^{ul}_{m,n,k}|^2, \end{aligned} \tag{B.2}$$

where $v^{dl}_{m,n,k}$ and $v^{ul}_{m,n,k}$ are the MSE receiver filters for the DL and UL, respectively. To acquire the minimum MSE (MMSE) for the DL and UL, the optimal $v^{dl}_{m,n,k}$ and $v^{ul}_{m,n,k}$ are deduced from $\frac{\partial e^{dl}_{m,n,k}}{\partial v^{dl}_{m,n,k}} = 0$ and $\frac{\partial e^{ul}_{m,n,k}}{\partial v^{ul}_{m,n,k}} = 0$ respectively as

$$v^{dl\star}_{m,n,k} = \frac{\hat{h}^{dl}_{m,n,k} \sqrt{P^{dl}_{m,n,k}}}{|\hat{h}^{dl}_{m,n,k}|^2 P^{dl}_{m,n,k} + \sigma_k^2}, \text{ and } v^{ul\star}_{m,n,k} = \frac{h^{ul}_{m,k} \sqrt{P^{ul}_{m,n,k}}}{|\hat{h}^{ul}_{m,n,k}|^2 P^{ul}_{m,n,k} + \sigma^2}. \tag{B.3}$$

Substituting $v^{dl\star}_{m,n,k}$ and $v^{ul\star}_{m,n,k}$ into (B.1) and (B.2), the MMSE for the DL and UL are derived as

$$e^{dl}_{m,n,k} = \frac{\sigma_k^2}{|\hat{h}^{dl}_{m,n,k}|^2 P^{dl}_{m,n,k} + \sigma_k^2} \text{ and } e^{ul}_{m,n,k} = \frac{\sigma^2}{|\hat{h}^{ul}_{m,n,k}|^2 P^{ul}_{m,n,k} + \sigma^2}, \tag{B.4}$$

respectively. Using (B.4), the weighted MMSE (WMMSE) problem is expressed as

$$\begin{aligned}
\underset{L_g}{\text{minimize}} \quad & \sum_{k=1}^{K}\sum_{m=1}^{M}\sum_{n=1}^{N}\left[\bar{\omega}_k^{dl} e_{m,n,k}^{dl} + \bar{\omega}_k^{ul} e_{m,n,k}^{ul}\right] \\
\text{subject to} \quad & \sum_{m=1}^{M}\sum_{n=1}^{N} P_{m,n,k}^{dl} \le P_{0,max}^{dl},\ \bar{\omega}_k^{ul} \ge 0 \\
& \sum_{k=1}^{K}\sum_{m=1}^{M}\sum_{n=1}^{N} P_{m,n,k}^{ul} \le P_k^{ul} - P_c,\ \bar{\omega}_k^{dl} \ge 0, \\
& \alpha\sum_{k=1}^{K}\tau_k + (1-\alpha)\sum_{k=1}^{K}\psi_k = T,
\end{aligned} \tag{B.5}$$

where $L_g = [\alpha, \{P_{m,n,k}^{dl}\}, \{P_{m,n,k}^{ul}\}, \{\psi_k\}, \{\tau_k\}, \{\bar{\omega}_k^{dl}\}, \{\bar{\omega}_k^{ul}\}]$. Also, $\bar{\omega}_k^{dl}$ and $\bar{\omega}_k^{ul}$ are the WMMSE weights for the DL and UL, respectively. The WSR problem based on the MMSE is defined as

$$\begin{aligned}
\underset{L_g}{\text{maximize}} \quad & \sum_{k=1}^{K}\sum_{m=1}^{M}\sum_{n=1}^{N}\left[\omega_k^{dl} \bar{R}_{m,n,k}^{dl} + \omega_k^{ul} \bar{R}_{m,n,k}^{ul}\right] \\
\text{subject to} \quad & \sum_{m=1}^{M}\sum_{n=1}^{N} P_{m,n,k}^{dl} \le P_{0,max}^{dl},\ \omega_k^{ul} \ge 0, \\
& \sum_{k=1}^{K}\sum_{m=1}^{M}\sum_{n=1}^{N} P_{m,n,k}^{ul} \le P_k^{ul} - P_c,\ \omega_k^{dl} \ge 0, \\
& \alpha\sum_{k=1}^{K}\tau_k + (1-\alpha)\sum_{k=1}^{K}\psi_k = T,
\end{aligned} \tag{B.6}$$

where $L_g = [\alpha, \{P_{m,n,k}^{dl}\}, \{P_{m,n,k}^{ul}\}, \{\psi_k\}, \{\tau_k\}, \{\omega_k^{dl}\}, \{\omega_k^{ul}\}]$ and $\bar{R}_{m,n,k}^{dl} = -log_2(e_{m,n,k}^{dl})$ and $\bar{R}_{m,n,k}^{ul} = -log_2(e_{m,n,k}^{ul})$. The next step is to establish the relationship between the WSR and WMMSE. The Lagrangian and KKT condition of the WMMSE problem with respect to $P_{m,n,k}^{dl}$ and $P_{m,n,k}^{ul}$ are deduced as

$$\begin{aligned}
L_{\{WMMSE\}} = & \sum_{k=1}^{K}\bar{\omega}_k^{dl}\sum_{m=1}^{M}\sum_{n=1}^{N} e_{m,n,k}^{dl} - \sum_{k=1}^{K}\sum_{m=1}^{M}\sum_{n=1}^{N}\log_2(\bar{\omega}_k^{dl}) + \sum_{k=1}^{K}\bar{\omega}_k^{ul}\sum_{m=1}^{M}\sum_{n=1}^{N} e_{m,n,k}^{ul} \\
& - \sum_{k=1}^{K}\sum_{m=1}^{M}\sum_{n=1}^{N}\log_2(\bar{\omega}_k^{ul}) + \mu T - \lambda^{dl}\Big(\sum_{k=1}^{K}\sum_{m=1}^{M}\sum_{n=1}^{N} P_{m,n,k}^{dl} - P_{0,max}^{dl}\Big) - \mu(1-\alpha)\sum_{k=1}^{K}\psi_k \\
& - \sum_{k=1}^{K}\lambda_k^{ul}\Big(\sum_{m=1}^{M}\sum_{n=1}^{N} P_{m,n,k}^{ul} + P_c - P_k^{dl}\Big) - \mu\alpha\sum_{k=1}^{K}\tau_k,
\end{aligned} \tag{B.7}$$

$$\frac{\partial L_{\{WMMSE\}}}{\partial P_{m,n,k}^{dl}} = -\bar{\omega}_k^{dl}\frac{\sigma_k^2|\hat{h}_{m,n,k}^{dl}|^2}{(|\hat{h}_{m,n,k}^{dl}|^2 P_{m,n,k}^{dl} + \sigma_k^2)^2} - \lambda^{dl} + \tau_k|\hat{h}_{m,n,k}^{dl}|^2\sum_{j=1}^{K}\frac{\lambda_j^{ul}\beta_j\alpha}{(1-\alpha)\psi_j}, \tag{B.8}$$

and

$$\frac{\partial L_{\{WMMSE\}}}{\partial P_{m,n,k}^{ul}} = -\bar{\omega}_k^{dl}\frac{\sigma_k^2|\hat{h}_{m,n,k}^{dl}|^2}{(|\hat{h}_{m,n,k}^{dl}|^2 P_{m,n,k}^{dl} + \sigma_k^2)^2} - \lambda^{ul}. \tag{B.9}$$

Similarly, the Lagrangian and KKT conditions for the WSR problem with respect to $P^{dl}_{m,n,k}$ and $P^{ul}_{m,n,k}$ are deduced as

$$\begin{aligned} L_{\{WSR\}} = &- \sum_{k=1}^{K} \alpha \tau_k \omega_k^{dl} T \sum_{m=1}^{M} \sum_{n=1}^{N} \log_2 \Big(\frac{\sigma^2_{z^{dl}}}{|\hat{h}^{dl}_{m,n,k}|^2 P^{dl}_{m,n,k} + \sigma^2_{z^{dl}}} \Big) \\ &- \sum_{k=1}^{K} (1-\alpha) \psi_k \omega_k^{ul} T \sum_{m=1}^{M} \sum_{n=1}^{N} \log_2 \Big(\frac{\sigma^2_{z^{ul}}}{|\hat{h}^{ul}_{m,n,k}|^2 P^{ul}_{m,n,k} + \sigma^2_{z^{ul}}} \Big) \\ &- \lambda^{dl} \Big(\sum_{k=1}^{K} \sum_{m=1}^{M} \sum_{n=1}^{N} P^{dl}_{m,n,k} - P^{dl}_{0,max} \Big) - \mu (1-\alpha) \sum_{k=1}^{K} \psi_k \\ &- \sum_{k=1}^{K} \lambda^{ul}_k \Big(\sum_{m=1}^{M} \sum_{n=1}^{N} P^{ul}_{m,n,k} + P_c - P^{dl}_k \Big) - \mu \alpha \sum_{k=1}^{K} \tau_k + \mu T, \end{aligned} \tag{B.10}$$

$$\frac{\partial L_{\{WSR\}}}{\partial P^{dl}_{m,n,k}} = \frac{\alpha \tau_k \omega_k^{dl} T}{\log(2)} \Big(e^{dl}_{m,n,k} \Big)^{-1} \Big(\frac{\sigma^2_{z^{dl}} |\hat{h}^{dl}_{m,n,k}|^2}{(|\hat{h}^{dl}_{m,n,k}|^2 P^{dl}_{m,n,k} + \sigma^2_{z^{dl}})^2} \Big) - \lambda^{dl} + \tau_k |\hat{h}^{dl}_{m,n,k}|^2 \sum_{j=1}^{K} \frac{\lambda^{ul}_j \beta_j \alpha}{(1-\alpha)\psi_j}, \tag{B.11}$$

and

$$\frac{\partial L_{\{WSR\}}}{\partial P^{ul}_{m,n,k}} = \frac{(1-\alpha) \psi_k \omega_k^{ul} T}{\log(2)} \Big(e^{ul}_{m,n,k} \Big)^{-1} \times \Big(\frac{\sigma^2_{z^{ul}} |\hat{h}^{ul}_{m,n,k}|^2}{(|\hat{h}^{ul}_{m,n,k}|^2 P^{ul}_{m,n,k} + \sigma^2_{z^{ul}})^2} \Big) - \lambda^{ul}_k. \tag{B.12}$$

Comparing (B.8) and (B.9) to (B.11) and (B.12), respectively, the WMMSE weights can be estimated as

$$\bar{\omega}^{dl}_k = \frac{\alpha \tau_k \omega_k^{dl} T}{\log(2)} \Big(e^{dl}_{m,n,k} \Big)^{-1} \text{ and } \bar{\omega}^{ul}_k = \frac{(1-\alpha) \psi_k \omega_k^{ul} T}{\log(2)} \Big(e^{ul}_{m,n,k} \Big)^{-1}, \tag{B.13}$$

making the WSR and WMMSE problems equivalent. Now, inserting (B.13) into (B.7) results in

$$\begin{aligned} L_{\{WMMSE\}} = &\frac{MN}{2} \sum_{k=1}^{K} \Big[\frac{\alpha \tau_k \omega_k^{dl} T}{\log(2)} - \log_2 \Big(\frac{\alpha \tau_k \omega_k^{dl} T}{\log(2)} \Big) \Big] + \sum_{k=1}^{K} \sum_{m=1}^{M} \sum_{n=1}^{N} \log_2 \Big(\frac{\sigma^2_{z^{dl}}}{|\hat{h}^{dl}_{m,n,k}|^2 P^{dl}_{m,n,k} + \sigma^2_{z^{dl}}} \Big) \\ &+ MN \sum_{k=1}^{K} \Big[\frac{(1-\alpha) \psi_k \omega_k^{ul} T}{\log(2)} - \log_2 \Big(\frac{(1-\alpha) \psi_k \omega_k^{ul} T}{\log(2)} \Big) \Big] \\ &+ \sum_{k=1}^{K} \sum_{m=1}^{M} \sum_{n=1}^{N} \log_2 \Big(\frac{\sigma^2_{z^{ul}}}{|\hat{h}^{ul}_{m,n,k}|^2 P^{ul}_{m,n,k} + \sigma^2_{z^{ul}}} \Big) - \lambda^{dl} \Big(\sum_{k=1}^{K} \sum_{m=1}^{M} \sum_{n=1}^{N} P^{dl}_{m,n,k} - P^{dl}_{0,max} \Big) \\ &- \sum_{k=1}^{K} \lambda^{ul}_k \Big(\sum_{m=1}^{M} \sum_{n=1}^{N} P^{ul}_{m,n,k} + P_c - P^{dl}_k \Big) - \mu \Big(\alpha \sum_{k=1}^{K} \tau_k + (1-\alpha) \sum_{k=1}^{K} \psi_k - T \Big), \end{aligned} \tag{B.14}$$

From (B.14), the WMMSE problem can be split into the time and weight resource allocation problem and the power resource allocation problem as

$$\begin{aligned} \underset{\alpha,\{\psi_k\},\{\tau_k\},\omega_k^{dl},\omega_k^{ul}}{\text{minimize}} \quad & T_{RS} \\ \text{subject to} \quad & \alpha\sum_{k=1}^{K}\tau_k+(1-\alpha)\sum_{k=1}^{K}\psi_k=T,\ \omega_k^{ul}\geq 0, \\ & \sum_{m=1}^{M}\sum_{n=1}^{N}P_{m,n,k}^{ul}\leq P_k^{ul}-P_c,\ \omega_k^{dl}\geq 0, \end{aligned} \tag{B.15}$$

and

$$\begin{aligned} \underset{\{P_{m,n,k}^{dl}\},\{P_{m,n,k}^{ul}\}}{\text{minimize}} \quad & P_{RS} \\ \text{subject to} \quad & \sum_{k=1}^{K}\sum_{m=1}^{M}\sum_{n=1}^{N}P_{m,n,k}^{dl}\leq P_{0,max}^{dl} \\ & \sum_{m=1}^{M}\sum_{n=1}^{N}P_{m,n,k}^{ul}\leq P_k^{ul}-P_c, \end{aligned} \tag{B.16}$$

where T_{RS} and P_{RS} are defined in (5.30) and (5.31), respectively. Therefore, the weights and time allocation can be determined from (B.15), while the power allocation can be determined from (B.16). ■

B.2 Convexity Proof of Time and Weight Resource Allocation Problem

The time and weight resource problem can be split into two sub problems, the DL time and weight allocation problem and the UL time and weight allocation problem. The Lagrangian of the individual problems are defined respectively as

$$\begin{aligned} L_{RS}^{dl} = {} & \frac{MN}{2}\sum_{k=1}^{K}\Big[\frac{\alpha\tau_k\omega_k^{dl}T}{\log(2)}-\log_2\Big(\frac{\alpha\tau_k\omega_k^{dl}T}{\log(2)}\Big)\Big]-\mu\Big(\alpha\sum_{k=1}^{K}\tau_k+(1-\alpha)\sum_{k=1}^{K}\psi_k-T\Big) \\ & -\sum_{k=1}^{K}\lambda_k^{ul}\Big(\sum_{m=1}^{M}\sum_{n=1}^{N}P_{m,n,k}^{ul}+P_c-\frac{\alpha\beta_k}{(1-\alpha)\psi_k}\sum_{j=1}^{K}\tau_j\sum_{m=1}^{M}\sum_{n=1}^{N}|\hat{h}_{m,n,j}^{dl}|^2P_{m,n,j}^{dl}\Big). \end{aligned} \tag{B.17}$$

$$\begin{aligned} L_{RS}^{ul} = {} & MN\sum_{k=1}^{K}\Big[\frac{(1-\alpha)\psi_k\omega_k^{ul}T}{\log(2)}-\log_2\Big(\frac{(1-\alpha)\psi_k\omega_k^{ul}T}{\log(2)}\Big)\Big]-\mu\Big(\alpha\sum_{k=1}^{K}\tau_k+(1-\alpha)\sum_{k=1}^{K}\psi_k-T\Big) \\ & -\sum_{k=1}^{K}\lambda_k^{ul}\Big(\sum_{m=1}^{M}\sum_{n=1}^{N}P_{m,n,k}^{ul}+P_c-\frac{\alpha\beta_k}{(1-\alpha)\psi_k}\sum_{j=1}^{K}\tau_j\sum_{m=1}^{M}\sum_{n=1}^{N}|\hat{h}_{m,n,j}^{dl}|^2P_{m,n,j}^{dl}\Big). \end{aligned} \tag{B.18}$$

Concentrating on (B.17), the first derivatives of L_{RS}^{dl} with respect to the time and weight variables α, τ_k, and ω_k^{dl} are respectively given as

$$\frac{\partial L_{RS}^{dl}}{\partial \alpha} = \frac{MN}{2}\sum_{k=1}^{K}\Big[\frac{\tau_k \omega_k^{dl} T}{\log(2)} - \frac{1}{\alpha\log(2)}\Big] - \mu\sum_{k=1}^{K}\tau_k + \sum_{k=1}^{K}\frac{\lambda_k^{ul}\beta_k}{(1-\alpha)^2\psi_k}\sum_{j=1}^{K}\tau_j\sum_{m=1}^{M}\sum_{n=1}^{N}|\hat{h}_{m,n,j}^{dl}|^2 P_{m,n,j}^{dl}. \tag{B.19}$$

$$\frac{\partial L_{RS}^{dl}}{\partial \tau_k} = \frac{MN}{2}\Big[\frac{\alpha\omega_k^{dl} T}{\log(2)} - \frac{1}{\tau_k\log(2)}\Big] - \alpha\mu + \sum_{m=1}^{M}\sum_{n=1}^{N}|\hat{h}_{m,n,k}^{dl}|^2 P_{m,n,k}^{dl}\sum_{j=1}^{K}\frac{\lambda_j^{ul}\beta_j\alpha}{(1-\alpha)\psi_j}, \tag{B.20}$$

and

$$\frac{\partial L_{RS}^{dl}}{\partial \omega_k^{dl}} = \frac{MN}{2}\Big[\frac{\alpha\tau_k T}{\log(2)} - \frac{1}{\omega_k^{dl}\log(2)}\Big], \tag{B.21}$$

The Second derivatives of L_{RS}^{dl} with respect to the time variables α, τ_k, and ω_k^{dl} are respectively derived as

$$\frac{\partial^2 L_{RS}^{dl}}{\partial \alpha^2} = \frac{MNK}{2\log(2)\alpha^2} - \sum_{k=1}^{K}\frac{2\lambda_k^{ul}\beta_k}{(1-\alpha)^3\psi_k}\sum_{j=1}^{K}\tau_j\sum_{m=1}^{M}\sum_{n=1}^{N}|\hat{h}_{m,n,j}^{dl}|^2 P_{m,n,j}^{dl} \tag{B.22}$$

$$\frac{\partial^2 L_{RS}^{dl}}{\partial \tau_k^2} = \frac{MN}{\tau_k^2 2\log(2)} \tag{B.23}$$

$$\frac{\partial^2 L_{RS}^{dl}}{\partial \omega_k^{dl^2}} = \frac{MN}{\omega_k^{dl^2} 2\log(2)}. \tag{B.24}$$

$$\frac{\partial^2 L_{RS}^{dl}}{\partial \tau_k \partial \alpha} = \frac{MN\omega_k^{dl} T}{2\log(2)} - \mu + \sum_{m=1}^{M}\sum_{n=1}^{N}|\hat{h}_{m,n,k}^{dl}|^2 P_{m,n,k}^{dl}\sum_{j=1}^{K}\frac{\lambda_j^{ul}\beta_j}{(1-\alpha)^2\psi_j} \tag{B.25}$$

$$\frac{\partial^2 L_{RS}^{dl}}{\partial \omega_k^{dl} \partial \alpha} = \frac{MN\tau_k T}{2\log(2)} \tag{B.26}$$

The Hermitian matrix for the DL time and weight resource allocation problem Lagrangian is represented as

$$\begin{bmatrix} & \alpha & \tau_k & \omega_k^{dl} \\ \alpha & + & + & + \\ \tau_k & + & + & + \\ \omega_k^{dl} & + & + & + \end{bmatrix}. \tag{B.27}$$

From the Hermitian matrix all the second derivatives have positive values. Therefore, the DL time and weight allocation problem is convex with respect to all its variables.

Next, the convexity of the UL time and weight allocation problem is checked. The first derivatives of L_{RS}^{ul} with respect to the time and weight variables α, ψ_k, and ω_k^{ul} are respectively given as

$$\frac{\partial L_{RS}^{ul}}{\partial \alpha} = \mu\sum_{k=1}^{K}\psi_k - MN\sum_{k=1}^{K}\Big[\frac{\psi_k\omega_k^{ul} T}{\log(2)} - \frac{1}{(1-\alpha)\log(2)}\Big] + \sum_{k=1}^{K}\frac{\lambda_k^{ul}\beta_k}{(1-\alpha)^2\psi_k}\sum_{j=1}^{K}\tau_j\sum_{m=1}^{M}\sum_{n=1}^{N}|\hat{h}_{m,n,j}^{dl}|^2 P_{m,n,j}^{dl} \tag{B.28}$$

$$\frac{\partial L_{RS}^{ul}}{\partial \psi_k} = MN\Big[\frac{(1-\alpha)\omega_k^{ul}T}{\log(2)} - \frac{1}{\psi_k \log(2)}\Big] - (1-\alpha)\mu - \frac{\lambda_k^{ul}\beta_k\alpha}{(1-\alpha)\psi_k^2}\sum_{j=1}^{K}\tau_j\sum_{m=1}^{M}\sum_{n=1}^{N}|\hat{h}_{m,n,j}^{dl}|^2 P_{m,n,j}^{dl}, \tag{B.29}$$

$$\frac{\partial L_{RS}^{ul}}{\partial \omega_k^{ul}} = MN\Big[\frac{(1-\alpha)\psi_k T}{\log(2)} - \frac{1}{\omega_k^{ul}\log(2)}\Big]. \tag{B.30}$$

The Second derivatives of L_{RS}^{ul} with respect to the time variables α, ψ_k, and ω_k^{ul} are respectively derived as

$$\frac{\partial^2 L_{RS}^{ul}}{\partial \alpha^2} = \frac{MNK}{(1-\alpha)^2\log(2)} - \sum_{k=1}^{K}\frac{2\lambda_k^{ul}\beta_k}{(1-\alpha)^3\psi_k}\sum_{j=1}^{K}\tau_j\sum_{m=1}^{M}\sum_{n=1}^{N}|\hat{h}_{m,n,j}^{dl}|^2 P_{m,n,j}^{dl} \tag{B.31}$$

$$\frac{\partial^2 L_{RS}^{ul}}{\partial \psi_k^2} = \frac{MN}{\psi_k^2\log(2)} + \frac{2\lambda_k^{ul}\beta_k}{(1-\alpha)\psi_k^3}\sum_{j=1}^{K}\tau_j\sum_{m=1}^{M}\sum_{n=1}^{N}|\hat{h}_{m,n,j}^{dl}|^2 P_{m,n,j}^{dl} \tag{B.32}$$

$$\frac{\partial^2 L_{RS}^{ul}}{\partial \psi_k \partial \alpha} = -\frac{MN\omega_k^{ul}T}{\log(2)} + \mu - \frac{\lambda_k^{ul}\beta_k}{(1-\alpha)^2\psi_k^2}\sum_{j=1}^{K}\tau_j\sum_{m=1}^{M}\sum_{n=1}^{N}|\hat{h}_{m,n,j}^{dl}|^2 P_{m,n,j}^{dl} \tag{B.33}$$

$$\frac{\partial^2 L_{RS}^{ul}}{\partial \omega_k^{ul^2}} = \frac{MN}{\omega_k^{ul^2}\log(2)} \tag{B.34}$$

$$\frac{\partial^2 L_{RS}^{ul}}{\partial \omega_k^{ul}\partial \alpha} = -\frac{MN\psi_k T}{\log(2)} \tag{B.35}$$

$$\frac{\partial^2 L_{RS}}{\partial \omega_k^{ul}\partial \psi_k} = \frac{MN\alpha T}{\log(2)} \tag{B.36}$$

The Hermitian matrix for the UL time and weight resource allocation problem Lagrangian is represented as

$$\begin{bmatrix} & \alpha & \psi_k & \omega_k^{ul} \\ \alpha & + & - & - \\ \psi_k & - & + & + \\ \omega_k^{ul} & - & + & + \end{bmatrix}. \tag{B.37}$$

From the Hermitian matrix, L_{RS}^{ul} is non-convex with respect to all variables but convex with respect to individual variables. However, the differentials presented considered α and not $(1-\alpha)$ as a variable. If $(1-\alpha)$ is made a variable, then the total problem becomes a concave problem. ■

From the analysis presented above, both the DL and UL time and weight resource problems are concave problems. Hence, the overall time and weight resource allocation problem is concave.

B.3 Optimal Time and Weight Resource Allocation Proof

From (5.30), let $x_k = \frac{\tilde{\alpha}_k \omega_k^{dl} T}{\log(2)}$ and $z_k = \frac{\hat{\alpha}_k \omega_k^{ul} T}{\log(2)}$, where $\tilde{\alpha}_k = \alpha \tau_k$ and $\hat{\alpha}_k = (1-\alpha)\psi_k$. Thus, the optimization problem in (B.15) can be rewritten as

$$\begin{aligned} \underset{\{\tilde{\alpha}_k\},\{\hat{\alpha}_k\},\omega_k^{dl},\omega_k^{ul}}{\text{minimize}} \quad & \bar{T}_{RS} \\ \text{subject to} \quad & \sum_{k=1}^{K} \tilde{\alpha}_k + \sum_{k=1}^{K} \hat{\alpha}_k = T,\ \omega_k^{dl} \geq 0, \\ & \sum_{m=1}^{M}\sum_{n=1}^{N} P_{m,n,k}^{ul} \leq P_k^{ul} - P_c,\ \omega_k^{ul} \geq 0 \end{aligned} \tag{B.38}$$

where

$$\bar{T}_{RS} = \frac{MN}{2}\sum_{k=1}^{K}[x_k - \log_2(x_k)] + MN\sum_{k=1}^{K}[z_k - \log_2(z_k)]. \tag{B.39}$$

From $\bar{T}_{RS}$ the optimal values of x_k and z_k can be found individually by a line search method using

$$\bar{T}_{RS,k}^{dl} = \frac{MN}{2}[x_k - \log_2(x_k)] \tag{B.40}$$

and

$$\bar{T}_{RS,k}^{ul} = MN[z_k - \log_2(z_k)]. \tag{B.41}$$

This implies that the optimum solution of each UN can be found separately. However, by observing $\bar{T}_{RS,k}^{dl}$ and $\bar{T}_{RS,k}^{ul}$, it can be deduced that the optimal values of x_k and z_k are the same for all UNs, i.e. $x_1^\star = x_2^\star = \ldots = x_K^\star = z_1^\star = z_2^\star = \ldots = z_K^\star = x^\star$. Therefore, the line search will be performed once. Based on this deduction, the optimal $\tilde{\alpha}_k$, ω_k^{dl}, $\hat{\alpha}_k$, and ω_k^{ul} should satisfy

$$\frac{x^\star \log(2)}{T} = \tilde{\alpha}_1 \omega_1^{dl},\ \frac{x^\star \log(2)}{T} = \tilde{\alpha}_2 \omega_2^{dl}, \ldots, \frac{x^\star \log(2)}{T} = \tilde{\alpha}_K \omega_K^{dl} \tag{B.42}$$

$$\frac{x^\star \log(2)}{T} = \hat{\alpha}_1 \omega_1^{ul}, \frac{x^\star \log(2)}{T} = \hat{\alpha}_2 \omega_2^{ul}, \ldots, \frac{x^\star \log(2)}{T} = \hat{\alpha}_K \omega_K^{ul}. \tag{B.43}$$

Note that different combinations of values (i.e., $\tilde{\alpha}_k$ and ω_k^{dl}, and $\hat{\alpha}_k$ and ω_k^{ul}) can result in $\frac{x^\star \log(2)}{T}$. Therefore, there is a need to find the optimal values of $\tilde{\alpha}_k$, ω_k^{dl}, $\hat{\alpha}_k$, and ω_k^{ul}. First, let the optimal DL and UL weights be defined as

$$\begin{aligned} &\frac{x^\star \log(2)}{\tilde{\alpha}_1^\star T} = \omega_1^{dl^\star},\ \frac{x^\star \log(2)}{\tilde{\alpha}_2^\star T} = \omega_2^{dl^\star}, \ldots \frac{x^\star \log(2)}{\tilde{\alpha}_K^\star T} = \omega_K^{dl^\star}, \\ &\frac{x^\star \log(2)}{\hat{\alpha}_1^\star T} = \omega_1^{ul^\star},\ \frac{x^\star \log(2)}{\hat{\alpha}_2^\star T} = \omega_2^{ul^\star}, \ldots,\ \frac{x^\star \log(2)}{\hat{\alpha}_K^\star T} = \omega_K^{ul^\star}. \end{aligned} \tag{B.44}$$

Next, we find the optimal values of $\tilde{\alpha}_k$ and $\hat{\alpha}_k$. The differential of the optimization problem with respect to $\tilde{\alpha}_k$ and $\hat{\alpha}_k$ are given as

$$\frac{\partial L_{RS}}{\partial \tilde{\alpha}_k} = -\mu + \sum_{m=1}^{M}\sum_{n=1}^{N} |\hat{h}^{dl}_{m,n,k}|^2 P^{dl}_{m,n,k} \sum_{j=1}^{K} \frac{\lambda^{ul}_j \beta_j}{\hat{\alpha}_k} = 0, \tag{B.45}$$

$$\frac{\partial L_{RS}}{\partial \hat{\alpha}_k} = -\hat{\alpha}_k \mu - \frac{\lambda^{ul}_k \beta_k}{\hat{\alpha}_k^2} \sum_{j=1}^{K} \tilde{\alpha}_j \sum_{m=1}^{M}\sum_{n=1}^{N} |\hat{h}^{dl}_{m,n,j}|^2 P^{dl}_{m,n,j} = 0. \tag{B.46}$$

Multiplying (B.45) by $\hat{\alpha}_k$, gives

$$-\hat{\alpha}_k \mu + \hat{\alpha}_k \sum_{m=1}^{M}\sum_{n=1}^{N} |\hat{h}^{dl}_{m,n,k}|^2 P^{dl}_{m,n,k} \sum_{j=1}^{K} \frac{\lambda^{ul}_j \beta_j}{\hat{\alpha}_k} = 0, \tag{B.47}$$

Summing (B.46) and (B.47) for all UNs, results in

$$-\sum_{k=1}^{K} \tilde{\alpha}_k \sum_{m=1}^{M}\sum_{n=1}^{N} |\hat{h}^{dl}_{m,n,k}|^2 P^{dl}_{m,n,k} \sum_{j=1}^{K} \frac{\lambda^{ul}_j \beta_j}{\hat{\alpha}_k} - \mu \sum_{k=1}^{K} \hat{\alpha}_k = 0. \tag{B.48}$$

and

$$\sum_{k=1}^{K} \hat{\alpha}_k \sum_{m=1}^{M}\sum_{n=1}^{N} |\hat{h}^{dl}_{m,n,k}|^2 P^{dl}_{m,n,k} \sum_{j=1}^{K} \frac{\lambda^{ul}_j \beta_j}{\hat{\alpha}_k} - \mu \sum_{k=1}^{K} \hat{\alpha}_k = 0, \tag{B.49}$$

Now, subtracting (B.48) from (B.49) gives

$$\sum_{k=1}^{K} \hat{\alpha}_k \sum_{m=1}^{M}\sum_{n=1}^{N} |\hat{h}^{dl}_{m,n,k}|^2 P^{dl}_{m,n,k} \sum_{j=1}^{K} \frac{\lambda^{ul}_j \beta_j}{\hat{\alpha}_k} + \sum_{k=1}^{K} \tilde{\alpha}_k \sum_{m=1}^{M}\sum_{n=1}^{N} |\hat{h}^{dl}_{m,n,k}|^2 P^{dl}_{m,n,k} \sum_{j=1}^{K} \frac{\lambda^{ul}_j \beta_j}{\hat{\alpha}_k} = 0, \tag{B.50}$$

$$\sum_{k=1}^{K} (\hat{\alpha}_k + \tilde{\alpha}_k) \sum_{m=1}^{M}\sum_{n=1}^{N} |\hat{h}^{dl}_{m,n,k}|^2 P^{dl}_{m,n,k} \sum_{j=1}^{K} \frac{\lambda^{ul}_j \beta_j}{\hat{\alpha}_k} = 0, \tag{B.51}$$

$\sum_{m=1}^{M}\sum_{n=1}^{N} |\hat{h}^{dl}_{m,n,k}|^2 P^{dl}_{m,n,k} \sum_{j=1}^{K} \frac{\lambda^{ul}_j \beta_j}{\hat{\alpha}_k} > 0$, $\forall k$, which implies that $\hat{\alpha}_k + \tilde{\alpha}_k = 0$. Therefore, $\hat{\alpha}_k = -\tilde{\alpha}_k$. Moreover, since both $\hat{\alpha}_k$ and $\tilde{\alpha}_k$ are positive valued variables, $\hat{\alpha}_k = \tilde{\alpha}_k$. This implies that the optimal time allocation coincides with equal time allocation, i.e. $\hat{\alpha}_k = \tilde{\alpha}_k = 1/K$. This also leads to equal weight allocations for all UNs according to (B.44), i.e. $\omega^{dl}_k = \omega^{ul}_k = \omega_k$. Therefore, the weight of UN_k can be found as $\omega^{\star}_k = \frac{2x^{\star} K \log(2)}{T^2}$. ■

B.4 Convexity Proof and Solution for the Power Resource Allocation Problem

For the power allocation problem, the Lagrangian can be represented as

$$\begin{aligned} L_{RS} = &\sum_{k=1}^{K}\sum_{m=1}^{M}\sum_{n=1}^{N}\log_2\Big(\frac{\sigma_k^2}{|\hat{h}_{m,n,k}^{dl}|^2P_{m,n,k}^{dl}+\sigma_k^2}\Big)+\sum_{k=1}^{K}\sum_{m=1}^{M}\sum_{n=1}^{N}\log_2\Big(\frac{\sigma^2}{|\hat{h}_{m,n,k}^{ul}|^2P_{m,n,k}^{ul}+\sigma^2}\Big)\\ &-\sum_{k=1}^{K}\lambda_k^{ul}\Big[\sum_{m=1}^{M}\sum_{n=1}^{N}P_{m,n,k}^{ul}+P_c-\frac{\alpha\beta_k}{(1-\alpha)\psi_k}\sum_{j=1}^{K}\tau_j\sum_{m=1}^{M}\sum_{n=1}^{N}|\hat{h}_{m,n,j}^{dl}|^2P_{m,n,j}^{dl}\Big]\\ &-\lambda^{dl}\Big(\sum_{k=1}^{K}\sum_{m=1}^{M}\sum_{n=1}^{N}P_{m,n,k}^{dl}-P_{0,max}^{dl}\Big). \end{aligned} \tag{B.52}$$

The first derivatives of L_{RS} with respect to $P_{m,n,k}^{dl}$ and $P_{m,n,k}^{ul}$ are given as

$$\frac{\partial L_{RS}}{\partial P_{m,n,k}^{dl}} = -\frac{1}{\log(2)}\Big(\frac{|\hat{h}_{m,n,k}^{dl}|^2}{|\hat{h}_{m,n,k}^{dl}|^2P_{m,n,k}^{dl}+\sigma_k^2}\Big)-\lambda^{dl}+\tau_k|\hat{h}_{m,n,k}^{dl}|^2\sum_{j=1}^{K}\frac{\alpha\beta_j\lambda_j^{ul}}{(1-\alpha)\psi_j} \tag{B.53}$$

and

$$\frac{\partial L_{RS}}{\partial P_{m,n,k}^{ul}} = -\frac{1}{\log(2)}\Big(\frac{|\hat{h}_{m,n,k}^{ul}|^2}{|\hat{h}_{m,n,k}^{ul}|^2P_{m,n,k}^{ul}+\sigma^2}\Big)-\lambda_k^{ul}. \tag{B.54}$$

Furthermore, the second derivatives of L_{RS} with respect to $P_{m,n,k}^{dl}$ and $P_{m,n,k}^{ul}$ are given as

$$\frac{\partial^2 L_{RS}}{\partial P_{m,n,k}^{dl^2}} = \frac{1}{\log(2)}\Big(\frac{|\hat{h}_{m,n,k}^{dl}|^4}{(|\hat{h}_{m,n,k}^{dl}|^2P_{m,n,k}^{dl}+\sigma_k^2)^2}\Big), \tag{B.55}$$

$$\frac{\partial^2 L_{RS}}{\partial P_{m,n,k}^{ul^2}} = \frac{1}{\log(2)}\Big(\frac{|\hat{h}_{m,n,k}^{ul}|^4}{(|\hat{h}_{m,n,k}^{ul}|^2P_{m,n,k}^{ul}+\sigma^2)^2}\Big) \tag{B.56}$$

and

$$\frac{\partial^2 L_{RS}}{\partial P_{m,n,k}^{dl}\partial P_{m,n,k}^{ul}} = \frac{\partial^2 L_{RS}}{\partial P_{m,n,k}^{ul}\partial P_{m,n,k}^{dl}} = 0. \tag{B.57}$$

Hence, the Hermitian matrix for L_{RS} is given as

$$\begin{bmatrix} & P_{m,n,k}^{dl} & P_{m,n,k}^{ul} \\ P_{m,n,k}^{dl} & + & 0 \\ P_{m,n,k}^{ul} & 0 & + \end{bmatrix}. \tag{B.58}$$

From the above Hermitian matrix and second derivatives, it is obvious that L_{RS} is non-convex with respect to both variables. However, L_{RS} is a convex function considering the variables individually.

Therefore, from $\frac{\partial L_{RS}}{\partial P^{dl}_{m,n,k}}$ and $\frac{\partial L_{RS}}{\partial P^{ul}_{m,n,k}}$, the optimal $P^{dl}_{m,n,k}$ and $P^{ul}_{m,n,k}$ are defined as

$$P^{dl}_{m,n,k} = \Big[\frac{1}{\log(2)A} - \frac{\sigma_k^2}{|\hat{h}^{dl}_{m,n,k}|^2}\Big] \tag{B.59}$$

and

$$P^{ul}_{m,n,k} = \Big[\frac{1}{\lambda^{ul}_k \log(2)} - \frac{\sigma^2}{|\hat{h}^{ul}_{m,n,k}|^2}\Big] \tag{B.60}$$

with $A = (\lambda^{dl} - \tau_k \sum_{m=1}^{M}\sum_{n=1}^{N} |\hat{h}^{dl}_{m,n,k}|^2 \sum_{j=1}^{K} \frac{\alpha\beta_j \lambda^{ul}_j}{(1-\alpha)\psi_j})$.

An iterative algorithm is used to obtain the optimal $P^{dl}_{m,n,k}$ and $P^{ul}_{m,n,k}$ which minimizes problem (B.16). The optimal λ^{dl} can be found using the bisection method, while the optimal λ^{ul}_k is acquired as

$$\lambda^{ul}_k = \frac{MN}{\log(2)\Big(B - P_c + \sum_{m=1}^{M} \frac{N\sigma^2}{|\hat{h}^{ul}_{m,n,k}|^2}\Big)} \tag{B.61}$$

with $B = \frac{\alpha\beta_k}{(1-\alpha)\psi_k} \sum_{j=1}^{K} \tau_j \sum_{m=1}^{M}\sum_{n=1}^{N} |\hat{h}^{dl}_{m,n,j}|^2 P^{dl}_{m,n,j}$. ■

References

[1] ITU-R, "IMT Vision – Framework and overall objectives of the future development of IMT for 2020 and beyond," ITU, Tech. Rep. M.2083-0, Sep. 2015.

[2] W. Jiang, B. Han, M. A. Habibi, and H. D. Schotten, "The Road Towards 6G: A Comprehensive Survey," *IEEE Open Journal of the Communications Society*, vol. 2, pp. 334–366, Feb. 2021.

[3] Y. J. Harbi, "Enhanced air-interfaces for fifth generation mobile broadband communication," Ph.D. dissertation, University of York, Sep. 2017.

[4] 3GPP, *Study on New Radio Access Technology; Physical Layer Aspects*, TR 38.802 v14.2.0 (Rel. 14) ed., 2017.

[5] ——, *Study on New Radio Access Technology; Radio Interface Protocol Aspects*, TR 38.804 v14.0.0 (Rel. 14) ed., 2017.

[6] M. Pischella, R. Zakaria, and D. L. Ruyet, "On maximum D2D multiplexing in asynchronous communications," in *IEEE 87th Vehicular Technology Conference (VTC Spring)*, Jun. 2018, pp. 1–5.

[7] C. Sexton, Q. Bodinier, A. Farhang, N. Marchetti, F. Bader, and L. A. DaSilva, "Enabling asynchronous machine-type D2D communication using multiple waveforms in 5G," *IEEE Internet of Things Journal*, vol. 5, no. 2, pp. 1307–1322, Apr. 2018.

[8] T. Xu and I. Darwazeh, "Non-orthogonal narrowband internet of things: A design for saving bandwidth and doubling the number of connected devices," *IEEE Internet of Things Journal*, vol. 5, no. 3, pp. 2120–2129, Jun. 2018.

[9] D. Chen, Y. Tian, D. Qu, and T. Jiang, "OQAM-OFDM for wireless communications in future internet of things: A survey on key technologies and challenges," *IEEE Internet of Things Journal*, vol. 5, no. 5, pp. 3788–3809, Oct. 2018.

[10] A. T. Abebe and C. G. Kang, "Comprehensive grant-free random access for massive low latency communication," in *2017 IEEE International Conference on Communications (ICC)*, May 2017, pp. 1–6.

[11] M. Bellanger, D. Le Ruyet, D. Roviras, M. Terré, J. Nossek, L. Baltar, Q. Bai, D. Waldhauser, M. Renfors, T. Ihalainen *et al.*, "FBMC physical layer: A primer," *Phydyas*, vol. 25, no. 4, pp. 7–10, 2010.

[12] A. Sahin, I. Guvenc, and H. Arslan, "A survey on multicarrier communications: Prototype filters, lattice structures, and implementation aspects," *IEEE Commuications Surveys and Tutorials*, vol. 16, no. 3, pp. 1312–1338, 2014.

[13] R. Zakaria and D. L. Ruyet, "A novel filter-bank multicarrier scheme to mitigate the intrinsic interference: Application to MIMO systems," *IEEE Transactions on Wireless Communications*, vol. 11, no. 3, pp. 1112–1123, Mar. 2012.

[14] ——, "Intrinsic interference reduction in a filter bank-based multicarrier using QAM modulation," *Physical Communication*, vol. 11, pp. 15–24, Jun. 2014.

[15] J. J. Benedetto, C. Heil, and D. F. Walnut, "Differentiation and the Ballian-Low theorem," *J. Fourier Anal. Appl.*, vol. 1, no. 4, pp. 355–402, 1994.

[16] D. Demmer, R. Zakaria, R. Gerzaguet, J.-B. Dore, and D. L. Ruyet, "Study of OFDM precoded filter-bank waveforms," *IEEE Transaction on Wireless Communications*, vol. 18, no. 6, pp. 2889–2902, Jun. 2019.

[17] B. Saltzberg, "Performance of an efficient parallel data transmission system," *IEEE Transactions on Communication Technology*, vol. 15, no. 6, pp. 805–811, Dec. 1967.

[18] G. Wunder *et al.*, "5GNOW: Non-orthogonal, asynchronous waveforms for future mobile applications," *IEEE Commun. Mag.*, vol. 52, no. 2, pp. 97–105, Feb. 2014.

[19] H. Nam, M. Choi, S. Han, C. Kim, S. Choi, , and D. Hong, "A new filter-bank multicarrier system with two prototype filters for QAM symbols transmission and reception," *IEEE Transactions on Wireless Communications*, vol. 15, no. 9, pp. 5998–6009, Sep. 2016.

[20] S. M. Oteafy and H. S. Hassanein, "Resilient IoT architectures over dynamic sensor networks with adaptive components," *IEEE Internet Things J.*, vol. 4, no. 2, pp. 474–483, Apr. 2017.

[21] S. Mahama, D. K. P. Asiedu, and K.-J. Lee, "Simultaneous wireless information and power transfer for cooperative relay networks with battery," *IEEE Access*, vol. 5, pp. 13 171–13 178, Jul. 2017.

[22] D. K. P. Asiedu, S. Mahama, C. Song, D. Kim, and K.-J. Lee, "Beamforming and resource allocation for multi-user full-duplex wireless powered communications in IoT networks," *IEEE Int. Things J.*, vol. 7, no. 12, pp. 11 355 – 11 370, Dec. 2020.

[23] B. Clerckx, R. Zhang, R. Schober, D. W. K. Ng, D. I. Kim, and H. V. Poor, "Fundamentals of wireless information and power transfer: From RF energy harvester models to signal and system designs," *IEEE Journal on Selected Areas in Communications*, vol. 37, no. 1, pp. 4–33, Jan. 2019.

[24] F. Mukhlif, K. A. B. Noordin, A. M. Mansoor, and Z. M. Kasirun, "Green transmission for C-RAN based on SWIPT in 5G: A review," *Wireless Net.*, pp. 1–29, May 2018.

[25] F. Jameel, M. A. A. Haider, A. A. Butt *et al.*, "A technical review of simultaneous wireless information and power transfer (SWIPT)," in *Proc. IEEE Int. Symp. on Recent Adv. in Electrical Eng.*, Oct. 2017, pp. 1–6.

[26] M. Renfors, X. Mestre, E. Kofidis, and F. Bader, Eds., *Orthogonal waveforms and filter banks for future communication systems*. New York, NY, USA: Academic Press, 2017.

[27] G. A. Akpakwu, B. J. Silva, G. P. Hancke, , and A. M. Abu-Mahfouz, "A survey on 5G networks for the internet of things: Communication technologies and challenges," *IEEE Access*, vol. 6, p. 3619–3647, Feb. 2018.

[28] Cisco, "Cisco visual networking index: Global mobile data traffic forecast update, 2015-2020," Cisco, Tech. Rep., Feb. 2016.

[29] A. Osseiran *et al.*, "Scenarios for 5G mobile and wireless communications: The vision of the METIS project," *IEEE Communications Magazine*, vol. 52, pp. 26–35, May 2014.

[30] R. L. G. Cavalcante, S. Stanczak, M. Schubert, A. Eisenblaetter, and U. Tuerke, "Toward energy-efficient 5G wireless communications technologies: Tools for decoupling the scaling of networks from the growth of operating power," *IEEE Signal Processing Magazine*, vol. 31, no. 6, pp. 24–34, Nov. 2014.

[31] 3GPP, *NR; Physical Channels and Modulation*, TS 38.211 v15.3.0 (Rel. 15) ed., 2018.

[32] R. Chang, "High-speed multichannel data transmission with bandlimited orthogonal signals," *Bell System Technical Journal*, vol. 45, p. 1775–1796, 1966.

[33] E. T. S. Institute, *Digital Video Broadcasting (DVB); Framing structure, channel coding and modulation for digital terrestrial television*, ETSI ETS 300 744, V1.6.1 ed., Jan. 2009.

[34] *IEEE Standard for wireless MAN-Advanced air interface for broadband wireless access systems*, IEEE Std 802.16.1-2012 ed., Sep. 2012.

[35] *Evolved Universal Terrestrial Radio Access (E-UTRA); User Equipment (UE) Radio Transmission and Reception*, TS 136 304, 3GPP TSG RAN ed., 2017.

[36] A. Peled and A. Ruiz, "Frequency domain data transmission using reduced computational complexity algorithms," in *IEEE International Conference on Acoustics, Speech, and Signal Processing, ICASSP*, Apr. 1980, p. 964–967.

[37] J. A. Lopez-Salcedo *et al.*, "Unified framework for the synchronization of flexible multicarrier communication signals," *IEEE Transaction Signal Processing*, vol. 61, no. 4, p. 828–842, Feb. 2013.

[38] E. Kofidis, "A tensor-based approach to joint channel estimation/data detection in flexible multicarrier MIMO systems," *IEEE Transaction on Signal Processing*, vol. 68, pp. 3179–3193, May 2020.

[39] S. Weinstein and P. Ebert, "Data transmission by frequency-division multiplexing using the discrete fourier transform," *IEEE Transactions on Communication Technology*, vol. 19, p. 628–634, Oct. 1971.

[40] H. S. Stone, "R66-50: An algorithm for the machine calculation of complex fourier series," *IEEE Transactions on Electronic Computers*, vol. 15, p. 680–681, Aug. 1966.

[41] X. Zhang, M. Jia, L. Chen, J. Ma, and J. Qiu, "Filtered-OFDM - enabler for flexible waveform in the 5th generation cellular networks," in *IEEE Global Communication Conference (GLOBECOM)*, Apr. 2015, pp. 1–6.

[42] 3GPP, *f-OFDM scheme and filter design*, R1-165425 ed., 2016.

[43] G. Fettweis, M. Krondorf, and S. Bittner, "GFDM - Generalized frequency division multiplexing," in *IEEE Vehicular Technology Conference (VTC)*, Apr. 2009, pp. 1–4.

[44] N. Michailow, M. Matthe, I. Gaspar, A. N. Caldevilla, L. L. Mendes, A. Festag, and G. Fettweis, "Generalized frequency division multiplexing for 5th generation cellular networks," *IEEE Transaction on Communications*, vol. 62, no. 9, pp. 3045–3061, Sep. 2014.

[45] N. Michailow, I. Gaspar, S. Krone, M. Lentmaier, and G. Fettweis, "Generalized frequency division multiplexing: Analysis of an alternative multicarrier technique for next generation cellular systems," in *IEEE International Symposium Wireless Communication Systems (ISWCS)*, Aug. 2012, pp. 171–175.

[46] R. Datta, N. Michailow, M. Lentmaier, and G. Fettweis, "GFDM interference cancellation for flexible cognitive radio PHY design," in *IEEE Vehicular Technology Conference (VTC Fall)*, Sep. 2012, pp. 1–5.

[47] N. Michailow, S. Krone, M. Lentmaier, and G. Fettweis, "Bit error rate performance of generalized frequency division multiplexing," in *IEEE Vehicular Technology Conference (VTC Fall)*, Sep. 2012, pp. 1–5.

[48] G. Cherubini, E. Eleftheriou, S. Oker, and J. M. Ciof, "Filter bank modulation techniques for very high speed digital subscriber lines," *IEEE Communications Magazine*, vol. 38, no. 5, pp. 98–104, May 2000.

[49] B. Farhang-Boroujeny, "OFDM versus filter bank multicarrier," *IEEE Signal Processing Magazine*, vol. 28, no. 3, pp. 92–112, May 2011.

[50] PHYDYAS Project , "D5.1 prototype filter and structure optimization," Tech. Rep., 2009.

[51] M. G. Bellanger, "Specification and design of a prototype filter for filter bank based multicarrier transmission," in *IEEE International Conference on Acoustics, Speech, and Signal Processing*, May 2001, pp. 2417 – 2420.

[52] B. Kwon, S. Kim, and S. Lee, "Scattered reference symbol-based channel estimation and equalization for FBMC-QAM systems," *IEEE Transaction on Communications*, vol. 65, no. 8, pp. 3522–3537, Aug. 2017.

[53] D. Chen, Y. Tian, D. Qu, and T. Jiang, "OQAM-OFDM for wireless communications in future internet of things: A survey on key technologies and challenges," *IEEE Internet of Things Journal*, vol. 5, no. 5, pp. 3788–3809, Oct. 2018.

[54] D. Chen, X.-G. Xia, T. Jiang, and X. Gao, "Properties and power spectral densities of CP based OQAM-OFDM systems," *IEEE Transaction on Signal Processing*, vol. 63, no. 14, pp. 3561–3575, Jul. 2015.

[55] A. Gorokhov and J. . Linnartz, "Robust OFDM receivers for dispersive time-varying channels: equalization and channel acquisition," *IEEE Transactions on Communications*, vol. 52, no. 4, pp. 572–583, Apr. 2004.

[56] A. B. Awoseyila, C. Kasparis, and B. G. Evans, "Robust time-domain timing and frequency synchronization for OFDM systems," *IEEE Transactions on Consumer Electronics*, vol. 55, no. 2, pp. 391–399, May 2009.

[57] S. . Phoong, Yubing Chang, and Chun-Yang Chen, "DFT-modulated filterbank transceivers for multipath fading channels," *IEEE Transactions on Signal Processing*, vol. 53, no. 1, pp. 182–192, Jan. 2005.

[58] T. Strohmer and S. Beaver, "Optimal OFDM design for time-frequency dispersive channels," *IEEE Transactions on Communications*, vol. 51, no. 7, pp. 1111–1122, Jul. 2003.

[59] D. Tse and P. Viswanath, *Fundamentals of Wireless Communication*. Cambridge: Cambridge University Press, May 2005.

[60] A. Bazin, "Massive MIMO for 5G scenarios with OFDM and FBMC/OQAM waveforms," Ph.D. dissertation, INSA de Rennes, 2018.

[61] J. Hao, J. Wang, and Y. Wu, "A new equalizer in doubly-selective channels for TDS-OFDM," *IEEE Transactions on Broadcasting*, vol. 61, no. 1, pp. 91–97, Mar. 2015.

[62] P. Muneer and S. M. Sameer, "Pilot-aided joint estimation of doubly selective channel and carrier frequency offsets in OFDMA uplink with high-mobility users," *IEEE Transactions on Vehicular Technology*, vol. 64, no. 1, pp. 411–417, Jan. 2015.

[63] B. Li, M. Sun, X. Li, A. Nallanathan, and C. Zhao, "Energy detection based spectrum sensing for cognitive radios over time-frequency doubly selective fading channels," *IEEE Transactions on Signal Processing*, vol. 63, no. 2, pp. 402–417, Jan. 2015.

[64] G. T. 36.211, *Technical Specification. LTE; Evolved Universal Terrestrial Radio Access (E-UTRA); Physical Channels and Modulation*, 3rd ed., 3GPP, 2012.

[65] 3GPP-TS-36.101, *Technical Specification. LTE; Evolved Universal Terrestrial Radio Access (E-UTRA); User Equipment (UE) radio transmission and reception*, 3rd ed., 3GPP, 2014.

[66] P. Bello, "Characterization of randomly time-variant linear channels," *IEEE Transactions on Communications Systems*, vol. 11, no. 4, pp. 360–393, Dec. 1963.

[67] P. Hoeher, "A statistical discrete-time model for the WSSUS multipath channel," *IEEE Transactions on Vehicular Technology*, vol. 41, no. 4, pp. 461–468, Nov. 1992.

[68] J. S. Sadowsky and V. Kafedziski, "On the correlation and scattering functions of the WSSUS channel for mobile communications," *IEEE Transactions on Vehicular Technology*, vol. 47, no. 1, pp. 270–282, Feb. 1998.

[69] C. Sgraja, J. Tao, and C. Xiao, "On discrete-time modeling of time-varying WSSUS fading channels," *IEEE Transactions on Vehicular Technology*, vol. 59, no. 7, pp. 3645–3651, Sep. 2010.

[70] A. I. Prikhodko, "Optimal and suboptimal differentially coherent reception of MDPSK in time-spread WSSUS channel," *IEEE Transactions on Communications*, vol. 58, no. 9, pp. 2604–2610, Sep. 2010.

[71] P. Wang and D. W. Lin, "On maximum-likelihood blind synchronization over WSSUS channels for OFDM systems," *IEEE Transactions on Signal Processing*, vol. 63, no. 19, pp. 5045–5059, Oct. 2015.

[72] R. H. Clarke, "A statistical theory of mobile-radio reception," *The Bell System Technical Journal*, vol. 47, no. 6, pp. 957–1000, Jul. 1968.

[73] C. Xiao, Y. R. Zheng, and N. C. Beaulieu, "Novel sum-of-sinusoids simulation models for rayleigh and rician fading channels," *IEEE Transactions on Wireless Communications*, vol. 5, no. 12, pp. 3667–3679, Dec. 2006.

[74] W. C. Jakes, *Microwave mobile communications*. IEEE press, 1994.

[75] M. F. Pop and N. C. Beaulieu, "Limitations of sum-of-sinusoids fading channel simulators," *IEEE Transactions on Communications*, vol. 49, no. 4, pp. 699–708, Apr. 2001.

[76] M. Patzold, U. Killat, F. Laue, and Yingchun Li, "On the statistical properties of deterministic simulation models for mobile fading channels," *IEEE Transactions on Vehicular Technology*, vol. 47, no. 1, pp. 254–269, Feb. 1998.

[77] Yahong Rosa Zheng and Chengshan Xiao, "Simulation models with correct statistical properties for rayleigh fading channels," *IEEE Transactions on Communications*, vol. 51, no. 6, pp. 920–928, Jun. 2003.

[78] Kun-Wah Yip and Tung-Sang Ng, "A simulation model for Nakagami-m fading channels, m<1," *IEEE Transactions on Communications*, vol. 48, no. 2, pp. 214–221, Feb. 2000.

[79] Chengshan Xiao and Y. R. Zheng, "A generalized simulation model for rayleigh fading channels with accurate second-order statistics," in *Vehicular Technology Conference. IEEE 55th Vehicular Technology Conference. VTC Spring 2002 (Cat. No.02CH37367)*, vol. 1, May 2002, pp. 170–174 vol.1.

[80] A. Alimohammad and B. F. Cockburn, "Modeling and hardware implementation aspects of fading channel simulators," *IEEE Transactions on Vehicular Technology*, vol. 57, no. 4, pp. 2055–2069, Jul. 2008.

[81] P. Dent, G. E. Bottomley, and T. Croft, "Jakes fading model revisited," *Electronics Letters*, vol. 29, no. 13, pp. 1162–1163, Jun. 1993.

[82] E. Zehavi, "8-PSK trellis codes for a rayleigh channel," *IEEE Transactions on Communications*, vol. 40, no. 5, pp. 873–884, May 1992.

[83] A. Alvarado, "Towards fully optimized BICM transmissions," Ph.D. dissertation, Chalmers Univ. of Tech., Goteborg, Sweden, 2010.

[84] X. Li and J. A. Ritcey, "Bit-interleaved coded modulation with iterative decoding," *IEEE Communications Letters*, vol. 1, no. 6, p. 169–171, Nov. 1997.

[85] S. ten Brink, J. Speidel, and R. . Han, "Iterative demapping for QPSK modulation," *Electronics Letters*, vol. 34, no. 15, pp. 1459–1460, Jul. 1998.

[86] S. Benedetto, D. Divsalar, G. Montorsi, and F. Pollara, "Soft-input soft-output modules for the construction and distributed iterative decoding of code networks," *Eur. Trans. Telecommun.*, vol. 9, pp. 155–172, Mar. 1998.

[87] Xiaodong Li, A. Chindapol, and J. A. Ritcey, "Bit-interleaved coded modulation with iterative decoding and 8 PSK signaling," *IEEE Transactions on Communications*, vol. 50, no. 8, pp. 1250–1257, Aug. 2002.

[88] C. Berrou, A. Glavieux, and P. Thitimajshima, "Near shannon limit error-correcting coding and decoding: Turbo-codes," in *Proceedings of ICC '93 - IEEE International Conference on Communications*, vol. 2, May 1993, pp. 1064–1070.

[89] D. Hui, S. Sandberg, Y. Blankenship, M. Andersson, and L. Grosjean, "Channel coding in 5G new radio: A tutorial overview and performance comparison with 4G LTE," *IEEE Vehicular Technology Magazine*, vol. 13, no. 4, pp. 60–69, Dec. 2018.

[90] R. Gallager, "Low-density parity-check codes," *IRE Transactions on Information Theory*, vol. 8, no. 1, pp. 21–28, Jan. 1962.

[91] J. S. Johnson, *Iterative error correction: Turbo, low-density parity check and repeat-accumulate codes*, C. U. Press, Ed. Cambridge University Press, 2009.

[92] M. Luby, M. Mitzenmacher, M. A. Shokrollahi, , and D. A. Spielman, "Improved low-density parity-check codes using irregular graphs," *IEEE Transactions on Information Theory*, vol. 47, no. 2, p. 585–598, Feb. 2001.

[93] R. Tanner, "A recursive approach to low complexity codes," *IEEE Transactions on Information Theory*, vol. 27, no. 5, pp. 533–547, Sep. 1981.

[94] L. R. Varshney, "Performance of LDPC codes under faulty iterative decoding," *IEEE Transactions on Information Theory*, vol. 57, no. 7, pp. 4427–4444, Jul. 2011.

[95] S. ten Brink, "Convergence behavior of iteratively decoded parallel concatenated codes," *IEEE Transaction on Commununications*, vol. 49, no. 10, pp. 1727 – 1737, Oct. 2001.

[96] J. Hagenauer, "The EXIT chart - introduction to extrinsic information transfer in iterative processing," in *12th European Signal Processing Conference*, 2004, pp. 1541–1548.

[97] F. Brannstrom, L. K. Rasmussen, and A. J. Grant, "Convergence analysis and optimal scheduling for multiple concatenated codes," *IEEE Transactions on Information Theory*, vol. 51, no. 9, p. 3354–3364, 2005.

[98] S. Bi, C. K. Ho, and R. Zhang, "Wireless powered communication: Opportunities and challenges," *IEEE Commun. Mag.*, vol. 53, no. 4, pp. 117–125, Apr. 2015.

[99] X. Lu, P. Wang, D. Niyato, D. I. Kim, and Z. Han, "Wireless networks with RF energy harvesting: A contemporary survey," *IEEE Commun. Surveys Tut.*, vol. 17, no. 2, pp. 757–789, May 2015.

[100] H. Lee, K.-J. Lee, H.-B. Kong, and I. Lee, "Sum-rate maximization for multiuser MIMO wireless powered communication networks," *IEEE Trans. Veh. Tech.*, vol. 65, no. 11, pp. 9420–9424, Nov. 2016.

[101] S. Yin, Z. Qu, Z. Wang, and L. Li, "Energy-efficient cooperation in cognitive wireless powered networks," *IEEE Commun. Lett.*, vol. 21, no. 1, pp. 128–131, Jan. 2017.

[102] D. K. P. Asiedu, "Wireless information and power transfer for multi-relay and multi-user internet of things networks," Ph.D. dissertation, Hanbat National University, May 2019.

[103] X. Chen, Z. Zhang, H. Chen, and H. Zhang, "Enhancing wireless information and power transfer by exploiting multi-antenna techniques," *IEEE Communications Magazine*, vol. 53, no. 4, pp. 133–141, Apr. 2015.

[104] H. Lee, K.-J. Lee, H. Kim, and I. Lee, "Joint transceiver optimization for MISO SWIPT systems with time switching," *IEEE Trans. Wireless Commun.*, vol. 17, no. 5, pp. 3298–3312, May 2018.

[105] K. Huang and X. Zhou, "Cutting the last wires for mobile communications by microwave power transfer," *IEEE Communications Magazine*, vol. 53, no. 6, pp. 86–93, Jun. 2015.

[106] D. K. P. Asiedu, H. Lee, and K.-J. Lee, "Simultaneous wireless information and power transfer for decode-and-forward multihop relay systems in energy-constrained IoT networks," *IEEE Int. Things J.*, vol. 6, no. 6, pp. 9413–9426, Aug. 2019.

[107] S. H. Chae, C. Jeong, and S. H. Lim, "Simultaneous wireless information and power transfer for internet of things sensor networks," *IEEE Int. Things J.*, vol. 5, no. 4, pp. 2829–2843, Aug. 2018.

[108] J. Tang, D. K. C. So, N. Zhao, A. Shojaeifard, and K.-K. Wong, "Energy efficiency optimization with SWIPT in MIMO broadcast channels for internet of things," *IEEE Int, Things J.*, vol. 5, no. 4, pp. 2605–2619, Aug. 2018.

[109] K. W. Choi and D. I. Kim, "Stochastic optimal control for wireless powered communication networks," *IEEE Trans. Wireless Commun*, vol. 15, no. 1, pp. 686–698, Jan. 2016.

[110] K. W. Choi, A. A. Aziz, D. Setiawan, N. M. Tran, L. Ginting, and D. I. Kim, "Distributed wireless power transfer system for internet-of-things devices," *IEEE Int. of Things J.*, vol. 5, no. 4, pp. 2657–2671, Aug. 2018.

[111] K. W. Choi, P. A. Rosyady, L. Ginting, A. A. Aziz, D. Setiawan, and D. I. Kim, "Theory and experiment for wireless-powered sensor networks: How to keep sensors alive," *IEEE Trans. Wireless Commun.*, vol. 17, no. 1, pp. 430–444, Jan. 2018.

[112] C. Song, H. Lee, and K. Lee, "Optimal precoder designs for sum-utility maximization in SWIPT-enabled multi-user MIMO cognitive radio networks," *IEEE Systems Journal*, vol. 13, no. 3, pp. 2332–2343, Sep. 2019.

[113] C. Song and Y. Jeon, "Weighted MMSE precoder designs for sum-utility maximization in multi-user SWIPT network-MIMO with per-BS power constraints," *IEEE Transactions on Vehicular Technology*, vol. 67, no. 3, pp. 2809–2813, Mar. 2018.

[114] C. Song, J. Park, B. Clerckx, I. Lee, and K. Lee, "Generalized precoder designs based on weighted MMSE criterion for energy harvesting constrained MIMO and multi-user MIMO channels," *IEEE Transactions on Wireless Communications*, vol. 15, no. 12, pp. 7941–7954, Dec. 2016.

[115] D. K. P. Asiedu, S. Mahama, S.-W. Jeon, and K.-J. Lee, "Optimal power splitting for simultaneous wireless information and power transfer in amplify-and-forward multiple-relay systems," *IEEE Access*, vol. 6, pp. 3459–3468, Feb. 2018.

[116] H. Lee, S. Lee, K. Lee, H. Kong, and I. Lee, "Optimal beamforming designs for wireless information and power transfer in MISO interference channels," *IEEE Transactions on Wireless Communications*, vol. 14, no. 9, pp. 4810–4821, Sep. 2015.

[117] Y. Liu, Z. Wen, N. C. Beaulieu, D. Liu, and X. Liu, "Power allocation for SWIPT in full-duplex AF relay interference channels using game theory," *IEEE Communications Letters*, vol. 24, no. 3, pp. 608–611, Mar. 2020.

[118] P. V. Tuan and I. Koo, "Optimizing efficient energy transmission on a SWIPT interference channel under linear/nonlinear EH models," *IEEE Systems Journal*, vol. 14, no. 1, pp. 457–468, Mar. 2020.

[119] Z. Na, X. Li, X. Liu, and Z. Deng, "Subcarrier allocation based simultaneous wireless information and power transfer for multiuser OFDM systems," *EURASIP J. Wireless Commun. Netw.*, vol. 2017, no. 1, p. 148, Sep. 2017.

[120] X. Zhou, R. Zhang, and C. K. Ho, "Wireless information and power transfer in multiuser OFDM systems," *IEEE Trans. Wireless Commun.*, vol. 13, no. 4, pp. 2282–2294, Apr. 2014.

[121] W. Lu, Y. Gong, J. Wu, H. Peng, and J. Hua, "Simultaneous wireless information and power transfer based on joint subcarrier and power allocation in OFDM systems," *IEEE Access*, vol. 5, pp. 2763–2770, Feb. 2017.

[122] Z. Na, J. Lv, M. Zhang, B. Peng, M. Xiong, and M. Guan, "GFDM based wireless powered communication for cooperative relay system," *IEEE Access*, vol. 7, pp. 50 971–50 979, Apr. 2019.

[123] Z. Na, J. Lv, F. Jiang, M. Xiong, and N. Zhao, "Joint subcarrier and subsymbol allocation-based simultaneous wireless information and power transfer for multiuser GFDM in IoT," *IEEE Internet Things J*, vol. 6, no. 4, pp. 5999–6006, Aug. 2019.

[124] D. C. Melgarejo, J. M. Moualeu, P. Nardelli, G. Fraidenraich, , and D. B. da Costa, "GFDM-based cooperative relaying networks with wireless energy harvesting," in *Proc. 16th Int. Symposium on Wireless Commun Systems (ISWCS)*. IEEE, Aug. 2019, pp. 416–421.

[125] B. Clerckx and E. Bayguzina, "Waveform design for wireless power transfer," *IEEE Transactions on Signal Processing*, vol. 64, no. 23, pp. 6313–6328, Dec. 2016.

[126] Y. Dong, M. J. Hossain, and J. Cheng, "Performance of wireless powered amplify and forward relaying over Nakagami-*m* fading channels with nonlinear energy harvester," *IEEE Communications Letters*, vol. 20, no. 4, pp. 672–675, Apr. 2016.

[127] Y. H. Yun, C. Kim, K. Kim, Z. Ho, B. Lee, and J.-Y. Seol, "A new waveform enabling enhanced QAM-FBMC systems," in *IEEE 16th International Workshop on Signal Processing Advances in Wireless Communications (SPAWC)*, 2015, pp. 116–120.

[128] D. Sim and C. Lee, "Performance evaluation based on effective channel analysis for FBMC-QAM system with two prototype filters," *IEEE Transaction on Communication*, vol. 67, no. 5, pp. 3552–3565, May 2019.

[129] J. Kim, Y. Park, S. Weon, J. Jeong, S. Choi, and D. Hong, "A new filter-bank multicarrier system: The linearly processed FBMC system," *IEEE Transactions on Wireless Communications*, vol. 17, no. 7, pp. 4888–4898, Jul. 2018.

[130] Y. J. Harbi and A. G. Burr, "On ISI and ICI cancellation for FBMC/OQAM system using iterative decoding and ML detection," in *Wireless Communications and Networking Conference (WCNC)*, Apr. 2016, pp. 1–6.

[131] Q. Li, J. Zhang, L. Bai, and J. Choi, "Performance analysis and system design of hierarchical modulated BICM-ID," *IEEE Transaction on Wireless Communication*, vol. 13, no. 6, p. 3056–3069, Jun. 2014.

[132] Q. Li, J. Zhang, and U. Epple, "Design and EXIT chart analysis of a doubly iterative receiver for mitigating impulsive interference in OFDM systems," *IEEE Transaction on Communication*, vol. 64, no. 4, pp. 1726–1736, Apr. 2016.

[133] Y. J. Harbi and A. G. Burr, "IIC of the MIMO-FBMC/OQAM system using linear and SIC detection schemes in LTE channel," in *Wireless Communications and Networking Conference (WCNC)*, Apr. 2018, pp. 1–6.

[134] M. Caus, M. Navarro, X. Mestre, and A. Perez-Neira, "Link adaptation in FBMC/OQAM systems using NB-LDPC codes," in *European Conference Networks and Communications*, Jun. 2016, pp. 1–5.

[135] S. ten Brink, G. Kramer, and A. Ashikhmin, "Design of low-density parity-check codes for modulation and detection," *IEEE Transaction on Communication*, vol. 52, no. 4, pp. 670–678, Apr. 2004.

[136] R. E. Chall, F. Nouvel, M. Hélard, and M. Liu, "Performance and complexity evaluation of iterative receiver for coded MIMO-OFDM systems," *Mobile Information Systems*, pp. 1–22, 2016.

[137] F. Schreckenbach, N. Gortz, J. Hagenauer, and G. Bauch, "Optimization of symbol mappings for bit-interleaved coded modulation with iterative decoding," *IEEE Communication Letters*, vol. 7, pp. 593–595, Dec. 2003.

[138] S. M. A. Oteafy and H. S. Hassanein, "Resilient IoT architectures over dynamic sensor networks with adaptive components," *IEEE Internet of Things Journal*, vol. 4, no. 2, pp. 474–483, Apr. 2017.

[139] M. R. A. Khandaker, C. Masouros, K.-K. Wong, and S. Timotheou, "Secure SWIPT by exploiting constructive interference and artificial noise," *IEEE Transaction on Communication*, vol. 67, no. 2, pp. 1326–1340, Feb. 2019.

[140] S. Mahama, Y. J. Harbi, A. G. Burr, and D. Grace, "Iterative interference cancellation in FBMC-QAM systems," in *Wireless Communications and Networking Conference (WCNC)*, Apr. 2019, pp. 1–5.

[141] ——, "A non-orthogonal waveform design with iterative detection and decoding for narrowband IoT applications," in *European Conference on Networks and Communications (EuCNC)*, 2019, pp. 1–5.

[142] A. Prathima, D. S. Gurjar, H. H. Nguyen, and A. Bhardwaj, "Performance analysis and optimization of bidirectional overlay cognitive radio networks with hybrid-SWIPT," *IEEE Transactions on Vehicular Technology*, vol. 69, no. 11, pp. 13 467–13 481, Nov. 2020.

[143] E. K. Chong and S. H. Zak, *An introduction to optimization*. John Wiley & Sons, Inc., 2013.

[144] GSMA, "5G, the internet of things and wearablle devices: Radio frequency exposure," GSMA, Tech. Rep., 2019.

[145] Z. Wang, L. Mei, X. Wang, and N. Zhang, "Bit error rate analysis of generalised frequency division multiplexing with weighted-type fractional fourier transform precoding," *IET Commun.*, vol. 11, no. 6, pp. 916–924, Mar. 2017.

[146] B. Lim and Y.-C. Ko, "Multiuser interference cancellation for GFDM with timing and frequency offsets," *IEEE Transaction on Communications*, vol. 67, no. 6, pp. 4337–4349, Jun. 2019.

[147] Y. Mostofi and D. C. Cox, "Mathematical analysis of the impact of timing synchronization errors on the performance of an OFDM system," *IEEE Transactions on Communications*, vol. 54, no. 2, pp. 226–230, Feb. 2006.

[148] B. Yang, L. Zhang, O. Onireti, P. Xiao, M. A. Imran, and R. Tafazolli, "Mixed-numerology signals transmission and interference cancellation for radio access network slicing," *IEEE Transactions on Wireless Communications*, vol. 19, no. 8, pp. 5132–5147, Aug. 2020.

[149] S. Mahama, Y. J. Harbi, A. G. Burr, and D. Grace, "Design and convergence analysis of an IIC-Based BICM-ID receiver for FBMC-QAM systems," *IEEE Open J. of the Comm. Society*, vol. 1, pp. 563 – 577, May 2020.

[150] X. Zhang, L. Zhang, P. Xiao, D. Ma, J. Wei, and Y. Xin, "Mixed numerologies interference analysis and inter-numerology interference cancellation for windowed OFDM systems," *IEEE Transactions on Vehicular Technology*, vol. 67, no. 8, pp. 7047–7061, Aug. 2018.

[151] M. Penner, S. Akin, M. Fuhrwerk, and J. Peissig, "Bit error probability for asynchronous channel access with interference cancellation and FBMC," in *2020 IEEE Wireless Communications and Networking Conference (WCNC)*, May 2020, pp. 1–7.

[152] B. Lim and Y. Ko, "SIR analysis of OFDM and GFDM waveforms with timing offset, CFO, and phase noise," *IEEE Transactions on Wireless Communications*, vol. 16, no. 10, pp. 6979–6990, Oct. 2017.